IMAGE GUIDED RADIATION THERAPY APPLICATIONS FOR HEAD AND NECK, PROSTATE, AND BREAST CANCERS USING 3D ULTRASOUND IMAGING AND MONTE CARLO DOSE CALCULATIONS

Danielle Fraser

Doctor of Philosophy

Department of Physics
McGill University, Montreal
2009-12

A thesis submitted to McGill University in partial fulfilment of the requirements of the degree of Doctor of Philosophy

ACKNOWLEDGEMENTS

I would like to acknowledge my supervisor, Frank Verhaegen, for his guidance during the past few years. He readily gave up his time during the day from which many fruitful discussions greatly enhanced this work. He also generously helped me with equipment in the evenings. He was instrumental in teaming up with equipment suppliers, and in facilitating research collaboration. His trust in me and interest in this project are much appreciated.

I would like to thank all those at Resonant Medical who patiently answered my questions regarding the 3D ultrasound system, and entertained my proposals for changing software and hardware: Geralyn Ochab; Ulrich Scheipers; Janet Hendry; Martin Lachaine; Sergei Koptenko; and Tony Falco. A special thank you goes to Philippe Fortier who always made the trek to the Montreal General Hospital to discuss the equipment with me.

I would also like to thank the Medical Physicists working at the Montreal General Hospital. Will Parker and Horatio Patrocinio answered all my clinical questions and introduced me to technologists in the department, thereby adding to the number of personnel I could ask questions to. Their feedback on the clinical relevance of this work, along with that from Eric Reynard, was much appreciated. Jan Seuntjens offered his time and advice for some of the work presented here. Gabriela Stroian introduced me to Monte Carlo (MC) codes and graciously translated this abstract. Wamied Abdel-Raman maintained the MC computer cluster and answered my questions regarding simulations. Marylene Brodeur discussed the computed tomography calibration phantom with me, which is used in MC simulations. Ervin Podgorsak first gave me the opportunity to work in the Medical Physics Unit and provided career advice.

I would like to thank all of the students with whom I have worked with in the Medical Physics Unit. In particular Yong Chen relentlessly looked at ultrasound images of the prostate and his time spent on the prostate study was much appreciated. Andrew Alexander and Emily Poon helped me with reading DICOM files, and provided a platform on which to analyze dose distributions. Geneviève Jarry helped me with dynamic MLC MC simulations and Emily Heath always stopped her work to help me with bugs in the DYNVMLC MC component module. Jonathon Thebaut provided linac modeling support.

Phil Wong taught me a lot about breast cancer patients and his discussions on this study greatly enhanced the work. The computed tomography technologists are thanked for offering their time to teach me and help me with scanning. The radiation therapists were extremely patient when I borrowed their patients for study. Fabio Cury showed interest and offered his

time to investigate new ultrasound applications in the clinic. Joe Larkin always readily answered technical questions regarding radiation therapy equipment.

ABSTRACT

In radiation therapy an uncertainty in the delivered dose always exists because anatomic changes are unpredictable and patient specific. Image guided radiation therapy (IGRT) relies on imaging in the treatment room to monitor the tumour and surrounding tissue to ensure their prescribed position in the radiation beam. The goal of this thesis was to determine the dosimetric impact on the misaligned radiation therapy target for three cancer sites due to common setup errors; organ motion, tumour tissue deformation, changes in body habitus, and treatment planning errors. For this purpose, a novel 3D ultrasound system (Restitu, Resonant Medical, Inc.) was used to acquire a reference image of the target in the computed tomography simulation room at the time of treatment planning, to acquire daily images in the treatment room at the time of treatment delivery, and to compare the daily images to the reference image. The measured differences in position and volume between daily and reference geometries were incorporated into Monte Carlo (MC) dose calculations. The EGSnrc (National Research Council, Canada) family of codes was used to model Varian linear accelerators and patient specific beam parameters, as well as to estimate the dose to the target and organs at risk under several different scenarios.

After validating the necessity of MC dose calculations in the pelvic region, the impact of interfraction prostate motion, and subsequent patient realignment under the treatment beams, on the delivered dose was investigated. For 32 patients it is demonstrated that using 3D conformal radiation therapy techniques and a 7 mm margin, the prescribed dose to the prostate, rectum, and bladder is recovered within 0.5% of that planned when patient setup is corrected for prostate motion, despite the beams interacting with a new external surface and internal tissue boundaries.

In collaboration with the manufacturer, the ultrasound system was adapted from transabdominal imaging to neck imaging. Two case studies of nasopharyngeal cancer are discussed. The deformation of disease-positive cervical lymph nodes was monitored throughout

treatment. Node volumes shrunk to 17% of the initial volume, moved up 1.3 cm, and received up to a 12% lower dose than that prescribed. It is shown that difficulties in imaging soft tissue in the neck region are circumvented with ultrasound imaging, and after dosimetric verification it is argued that adaptive replanning may be more beneficial than patient realignment when intensity modulated radiation therapy techniques are used.

Some of the largest dose delivery errors were found in external electron beam treatments for breast cancer patients who underwent breast conserving surgery. Inaccuracies in conventional treatment planning resulted in substantial target dose discrepancies of up to 88%. When patient setup errors, interfraction tumour bed motion, and tissue remodeling were considered, inadequate target coverage was exacerbated.

This thesis quantifies the dose discrepancy between that prescribed and that delivered. I delve into detail for common IGRT treatment sites, and illuminate problems that have not received much attention for less common IGRT treatment sites.

ABRÉGÉ

Des incertitudes dans la dose délivrée aux patients existent toujours car les changements anatomiques sont imprévisibles et spécifiques à chaque patient. La radiothérapie guidée par l'image (IGRT) dépend de l'imagerie en ligne afin de suivre la tumeur et les tissus sains adjacents, et s'assure que leur positions, par rapport au faisceau de radiation, est telle que planifiés. L'objectif de cette thèse a été de déterminer l'impact dosimétrique du désalignement de la cible par rapport au faisceau de radiation du aux erreurs d'installation, aux mouvement des organes, à la déformation de la tumeur, aux changements de l'habitus du corps et aux erreurs dans la planification du traitement. À cette fin, un nouveau système ultrason 3D (Restitu, Resonant Medical, Inc.) a été utilisé pour acquérir des images référence de la cible dans la salle de simulation tomodensitométrique au moment de la planification du traitement, et ensuite pour acquérir des images quotidiennes de la cible au moment du traitement. Les images quotidiennes ont été comparées à l'image de référence et les différences de position et volume ont été incorporées dans des calculs de dose Monte Carlo. La famille de logiciels EGSNRC (National Research Council, Canada) a été utilisée pour modéliser des accélérateurs linéaires Varian et des paramètres spécifiques à chaque patient ainsi que pour estimer la dose à la cible et aux organes à risque.

Premièrement, les calculs de dose Monte Carlo, longs mais précis, ont été validés pour la région homogène du pelvis. Ensuite, l'influence du mouvement de la prostate inter fractions et du réalignement du patient sur la distribution de dose délivrée a été investiguée. Pour 32 patients nous avons démontré que l'utilisation des techniques conformes 3D combinée à une marge de 7 mm autour de la cible se traduit par une différence de moins de 0.5% entre la dose délivrée et la dose planifiée pour la prostate, rectum et vessie lorsque le positionnement du patient est corrigé pour le mouvement de la prostate, même si les faisceaux interagissent avec une nouvelle surface externe et des nouveaux contours des organes internes.

En collaboration avec le fabriquant, le system ultrason a été adapté pour l'imagerie de la région du cou. Nous avons suivi la déformation des nœuds lymphoïdes cervicaux positives pour le cancer, due à la réponse à la radiation et à la perte de poids, pendant le traitement. Le volume des nœuds a diminue de 17% par rapport au volume initial, les nœuds ont bougés 1.3 cm SUP et ont reçu jusqu'à 12% moins de dose que planifiée. Nous avons montré que les difficultés d'acquérir des images des tissus mous dans cette région sont contournées avec l'imagerie par ultrason, et

après vérification dosimétrique, nous arguons que la planification adaptive pourrait être plus bénéfique que le réalignement pour cette région anatomique lorsque la radiothérapie modulée en intensité est utilisée.

Quelques-unes des plus grandes erreurs dans la dose délivrée aux patients ont été trouvées dans les traitements par faisceau d'électrons pour les patients atteints d'un cancer du sein et qui ont subi une chirurgie mammaire conservatrice. Les erreurs dans la planification conventionnelle du traitement se sont traduite en une différence de jusqu'a 88% entre la dose délivrée et la dose planifiée. Lorsque les erreurs de positionnement du patient, le mouvement inter fraction du lit tumoral et le remodelage du tissue ont été pris en compte, la couverture dosimétrique inadéquate a été exacerbée.

Cette thèse quantifie les différences entre la dose planifiée et la dose délivrée aux patients. Les sites traités fréquemment avec IGRT ont été examinés en détail et les problèmes qui n'ont pas reçu beaucoup d'attention pour les sites IGRT moins communs ont été éclairés.

TABLE OF CONTENTS

LIST OF TABLES

LIST OF FIGURES

STATEMENT OF ORIGINALITY

To the best of my knowledge the results reported in this thesis have not been previously published using the methods and materials used herein. This thesis reports on dosimetric verification of the target and organs at risk in external beam radiation therapy. Monte Carlo (MC) techniques are used throughout to model the patient specific treatment beam geometry and to simulate the dose deposition process for all dose calculations. A novel 3D ultrasound system was adapted and applied to image three cancer sites. Image guidance in radiation therapy has always been a subject of interest, and it's recent revival has lead to much work in the field, primarily focusing on x-ray imaging. MC simulations have also been the subject of much research. However, incorporating patient specific measurements from 3D ultrasound images in MC simulations is a unique idea.

Prostate image guidance is a subject heavily reported on in the literature, yet dose estimates to such a mobile target have often been estimated using analytical dose calculation algorithms, simulated motion, and a small number of data points. MC dose calculations considering tissue heterogeneities have been reported in the literature and reveal the shortcomings of analytical algorithms that employ heterogeneity corrections. However, we revealed that even in homogeneous regions, analytical algorithms still did not match MC dose calculations. We are the first group to use the combination of ultrasound measured motion and MC dose calculations for each fraction for a large number of patients. We also studied the dosimetric discrepancy between corrected and uncorrected alignment scenarios, which no other group has reported on in such detail, nor included dose volume histogram data for the bladder and rectum. We aim to improve on these works by using a larger sample patient population, an intramodality imaging system, accurate dose calculation techniques, and a dosimetric analysis relevant to current treatment plan evaluation methods.

Although ultrasound imaging is commonly used in diagnostic radiology, it's application in radiation therapy has been limited. Monitoring changes in neck tissue throughout a course of

treatment using ultrasound is a unique idea. Moreover, monitoring cervical lymph node position and geometry changes in order to verify the dose specifically to this tissue provides new information for the radiation therapy community.

Little research has been done to implement treatment verification in electron beams even though it is known that conventional treatment planning is inaccurate, and that some treatment sites are known to remodel with time. A recent study was published on the feasibility of imaging the tumour bed in breast cancer patients using ultrasound and on the feasibility of ultrasound-CT registration for this site. Yet they did not report on interfraction volume or position changes, or the impact on the delivered dose. We are the first to report on the dose to the tumour bed and surrounding edge tissue in electron beams incorporating ultrasound measurements from interfraction images.

CONTRIBUTION OF AUTHORS

In this thesis, we present five manuscripts which describe the equipment used in this work and which describe the dosimetric impact of interfraction target position and geometry changes in radiation therapy. I was first author on all manuscripts, yet the contribution from others was greatly appreciated.

For all manuscripts, my thesis supervisor, Dr. Frank Verhaegen, contributed significantly to defining the studies, discussing results, guiding further work, and carefully revising each text. Each manuscript was accepted by each of the co-authors.

The manuscript presented in Chapter 5 was a prospective study. Te Vuong, MD, was responsible for referring patients to the study. Palma Fava performed the majority of the ultrasound scans, always indicating my presence to the patients and followed my guidance for scanning. For those radiation therapy fractions when she was unavailable, I performed the scans. Dr. Tony Falco was instrumental in designing and initiating the study. I analyzed the ultrasound images and developed a new scanning protocol with software and hardware changes suggested to the manufacturer. The volume of interest was contoured with the aid of a sonographer (recognized in the Acknowledgements). I performed the phantom accuracy and precision measurements, and wrote the text. Fabio Cury, MD, was consulted periodically as the study progressed.

The manuscript presented in Chapter 6 is a follow up study to Chapter 5. In this manner the authors made similar contributions with the addition of Emily Poon, who provided the software used in the analysis. I performed all patient and phantom dose calculations. Dr. Frank Verhaegen provided the code to create digital phantoms read by DOSXYZnrc. Discussions with Dr. Frank Verhaegen lead to how best to present the data, and I wrote the text.

The manuscript presented in Chapter 7 was a retrospective study performed at the beginning of this work. Aichu Chang aided in collecting the treatment charts, which contain patient specific treatment parameters. Fabio Cury, MD, aided in interpreting the treatment

charts so that I could set up the Monte Carlo simulations and run them. Clarisse Mark taught me how to use the treatment planning software CADPLAN so that I could perform the dose calculations in CADPLAN. I analyzed the data, developed the conclusion, and wrote the text.

The manuscript presented in Chapter 8 was also a retrospective study. As such, Yong Chen helped collect the ultrasound data for 32 patients. I set up the simulation parameters and he monitored the simulation progress. Emily Poon provided software that was used in the analysis. I developed a method to incorporate measured interfraction organ motion into the uncorrected and corrected scenarios. I evaluated the data and wrote the text. The patients were referred by Fabio Cury, MD, and discussions with Dr. Tony Falco contributed to the final version of the text.

In Chapter 9, I ran the linear accelerator commissioning simulations and compared the data with measurements. Khalil Sultanem, MD, aided in setting up the study and referred the patients. I modeled the beam geometry and cutout shape for the simulations. Phil Wong, MD, contoured the tumour bed on the computed tomography and ultrasound images. I reviewed the literature and decided on the most relevant analysis and information to be presented. After the dose calculations were performed and analyzed, discussions with Phil Wong, MD, about the clinical relevance of the results aided in directing the text.

CHAPTER 1
General introduction

1.1 Radiation therapy as treatment modality

The discovery of x-rays by Wilhelm Roentgen in 1895 considerably advanced the medical world, with subsequent developments in medical imaging and treatment. In fact, the discovery and initial studies of x-rays and gamma rays were based on imaging the human hand [1,2]. Less than 60 days after the discovery of x-rays, clinical radiation therapy was born when Emil Grubbé treated an advanced ulcerated breast cancer with x-rays [3]. Since the 19th century x-rays have played an important role in atomic and nuclear physics, with applications including equipment sterilization, airport security, and chemical analysis, to name a few. Medical therapeutic applications of x-rays include treating cancer — the leading cause of premature deaths in Canada, where an estimated 171 000 new cases of cancer will be diagnosed, and 75 3000 deaths from cancer, will occur in 2009 [4].

Ionizing radiation (> 13.6 eV) interacts with tissue through various processes depositing energy along its direction of travel. It ionizes and excites atoms and molecules to create highly reactive chemical species that cause DNA damage and impair cellular functions for multiplication [5]. In this manner it is used to kill cancer cells or to shrink tumours. It is therefore not only used for curative purposes, but also for palliative care where the aim is for temporary local disease control, and symptomatic relief resulting in increased quality of life.

Radiation (photons and electrons) can be delivered to the patient from an external source, such as a linear accelerator (linac) as shown in Fig. 1.1, or from an internal source, such as radioactive seed implants used in brachytherapy. External beam therapy accounts for the majority of treatments [6]. This treatment technique can be highly localized such as stereotactic

radiosurgery where the requirements for positional accuracy in dose delivery are ±1 mm and ±5% [7]. External beams can also cover large areas of the body such as in total body irradiation to promote immunosuppresion for bone marrow transplants [8]. Intraoperative radiation therapy combines two conventional modalities of cancer treatment where a high radiation dose is delivered to surgically exposed tissue in a single session [9]. In comparison with surgical oncology and chemotherapy, external beam radiation therapy can be delivered on an outpatient basis and is capable of localized treatment targeting. It also has the distinct advantage of targeting not only the tumour site but also microscopic disease surrounding the tumour. This flexibility and widespread medical use continuously places radiation therapy at the forefront of patient care.

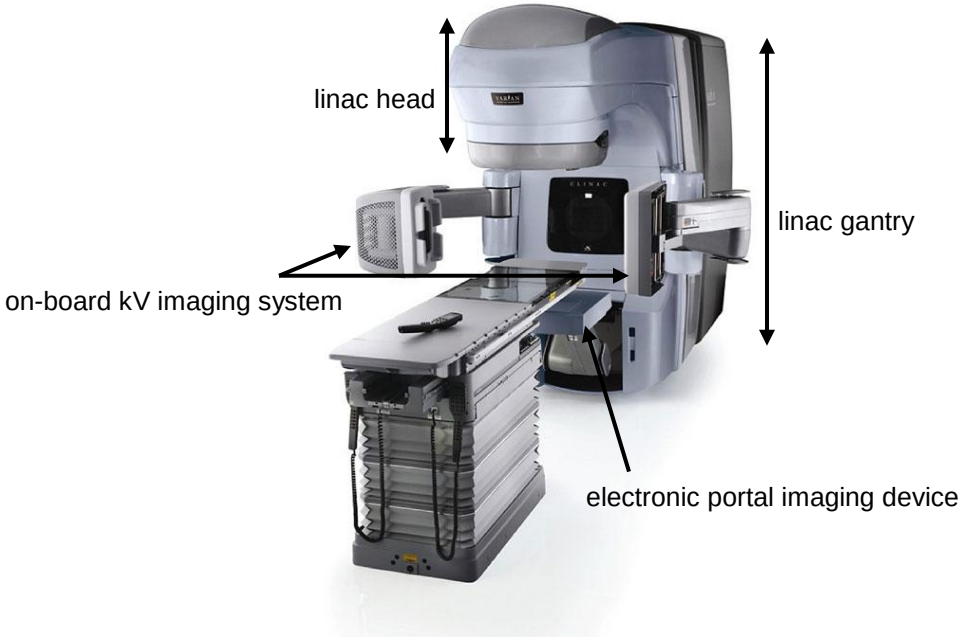

FIG. 1.1 A Varian Clinac iX linear accelerator mounted with a retractable electronic portal imaging device and an on-board kV imaging system. Image adapted from www.varian.com.

The interaction of radiation with tissue makes it a powerful ally to target malignant cells, and a powerful foe capable of damaging healthy cells. Much recent work in the field has focused on tightly conforming the dose to the target, which requires accurately localizing the target in the radiation treatment beam. This allows for an increase in the dose to the target while sparing

healthy tissue and organs at risk (OAR) [10-12]. A lower rate of complication may also mean lower cost of patient care following treatment [13]. Current trends to tighten the radiation beam and toward hypofractionation schemes require stringent patient positioning control [14]. Pretreatment verification imaging is playing an increasing role in the radiation delivery process and has become a key component in precision radiation therapy [15]. Moreover, patient specific organ motion and changes in body habitus are unpredictable so that pretreatment verification provides the only knowledge of the actual organ position during treatment.

1.2 Introduction to external beam radiation therapy

Initial applications of external beam radiation therapy utilized x-rays in the orthovoltage energy range (50 - 300 kVp) to treat superficial lesions in patients. The planning was simple and consisted of visual inspection of the patient's surface to define the treatment area. With the advent of isocentrically mounted treatment units, using either high activity radio-isotopes (Co-60, Cs-137), or megavoltage photon beams created with linacs, medical imaging became a necessity for treatment planning. Using a radiation therapy simulator treatment fields could be defined with respect to bony anatomy or implanted fiducial markers visible on radiographs. A simulator is a machine that geometrically mimics the motions of a treatment unit, but uses diagnostic quality x-rays to image the patient for planning purposes. Although this was a significant advance in radiation therapy planning, the position of the target was still uncertain due to poor soft tissue contrast, and so treatment fields were defined with generous margins.

Dose estimates in the patient were initially estimated from measured tabulated data, but with the advent of computers simple planning systems used measured data and patient contour information to provide individualized dose distributions. The work by Hounsfield [16] and the introduction of computed tomography scanners (CT) for planning meant that targets could be more accurately defined in 3D, and fields arranged in such a way as to maximize tumour dose while sparing healthy tissue. This method of conformal planning, also named three dimensional conformal radiation therapy (3DCRT), gave rise to more complex planning and delivery techniques in use today.

1.3 Recent developments in conformal treatment

In the 1980s, Brahme et al demonstrated the unique potential of intensity modulated beams to create homogeneous concave dose distributions [17]. Fundamental to the intensity modulated radiation therapy (IMRT) method is the use of non-uniform radiation intensity

profiles (Fig. 1.2), and computer optimized treatment planning. It has been suggested that with superior intensity modulation, dose conformity and resultant tumour control probability may be significantly improved [18].

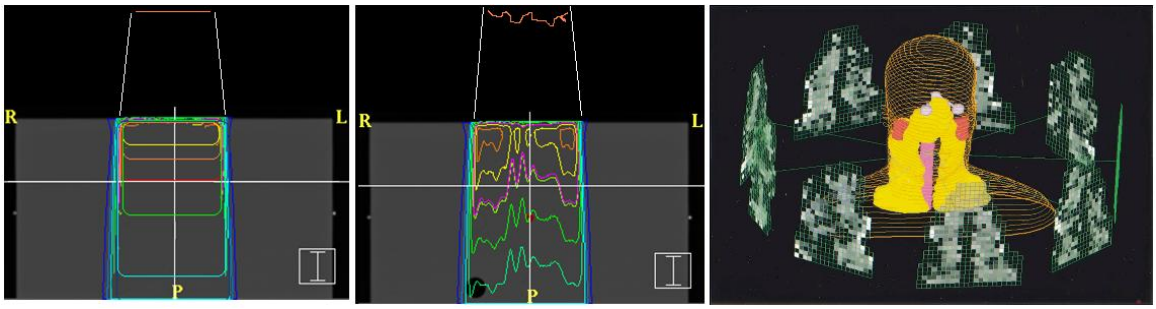

FIG. 1.2 Isodose lines from a conventional open field with uniform fluence profile (left) and from an IMRT field with intensity modulated fluence profile (middle). A head and neck dose distribution produced from the summation of multiple 2D intensity fluence maps (right).

The logical extension of simple field geometry is the replacement of conventional collimation devices with multileaf collimators (MLC) capable of intricate patterns for detailed field perimeter geometries (Fig. 1.3). Modern MLCs have many individually controlled, closely abutting leaves that generate arbitrary shapes. There are three basic applications of the MLC [19]. Traditionally they were used to define static irregular field perimeters for 3DCRT, such as in the treatment of prostate cancer used in this work. More recently MLCs have been used to spatially alter the beam intensity across the entire field by modulating the size, position, and dwell time of the gap between leaves. This type of delivery, where the field changes shape while the beam is on, was used for head and neck cancers in this thesis. A third function of the MLC is intensity modulated arc therapy, invented by Yu [20], which adjusts the shape as the gantry rotates so that the field outline matches the beam's eye view projection of the target.

Although most IMRT has relied on the use of MLC-based techniques, two radically alternative approaches were simultaneously and independently developed starting in about 1992. Helical tomotherapy delivers helical IMRT with a 6 MeV linac mounted on a gantry that rotates around a translating couch [21] (Fig. 1.4). The radiation beam is collimated to a narrow fan using a small set of 64 binary collimators that are switched on/off rapidly. The system also offers megavoltage computed tomography (MVCT) imaging by diminishing the nominal energy of the

incident electron beam to 3.5 MeV, and by detecting the transmitted photon fluence through a ring detector. The most recent arrival on the scene for clinical IMRT is the CyberKnife [22]. It is a short linear accelerator mounted on a robotic arm that has six degrees of freedom and delivers a number of pencil beams of different fluence and direction. CyberKnife determines the position of internal anatomy from ceiling mounted x-ray sources and a floor mounted x-ray detector, while infrared emitters are used to record the motion of the patient's skin surface. The versatility of IMRT lends its use to a multitude of areas and has quickly become the technique of choice for many treatment sites.

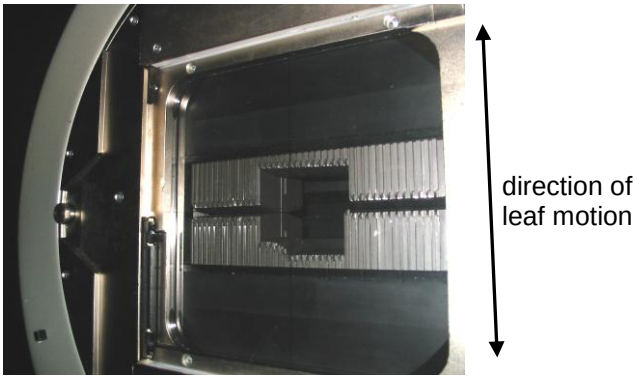

FIG. 1.3 Millennium MLC (Varian) with leaves positioned to form a lopsided rectangular shape.

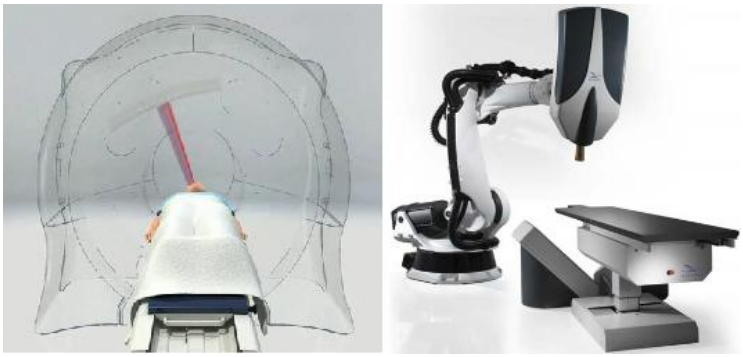

FIG. 1.4 A Tomotherapy unit (left) and CyberKnife system (right).

1.4 Imaging during radiation therapy

For many decades, improvements in radiation therapy were hampered by the inability to determine the 3D location of tumours accurately. With the advent of more advanced diagnostic imaging modalities like multi-slice CT, 3D ultrasound, anatomic and functional magnetic resonance (MR) imaging, positron emission tomography (PET), and single photon emission computed tomography (SPECT), the accuracy of dose delivery with new treatment techniques has now been limited by the uncertainty in target localization at the time of treatment. Interfraction as well as intrafraction target movement, relative to reference landmarks, coupled with set-up errors and other inaccuracies add to this uncertainty. The standard approach has been to add margins to the target volume at the expense of the benefits of conformal treatment delivery techniques [23].

Since high accuracy and precision are essential, treatment verification imaging immediately prior to the delivery of each fraction has become standard practice for many cancer sites. Inaccurate initial localization of internal anatomy, voluntary and involuntary patient motion, therapy induced time trends, natural tissue inhomogeneities, and the difficulty of reproducibly positioning an uncomfortable patient over a treatment course of several weeks lead to uncertainties far greater than the 2% attributed to dosimetry [24]. The role of image guidance is to achieve greater accuracy of daily target volume positioning, thus gaining knowledge of the location of the target volume on a daily basis. Image guided radiation therapy (IGRT) aims to always position the target relative to a predefined reference point so that the treatment plan may be delivered as expected [24]. This may allow for reduced treatment margins, improved tumour control probability, decreased treatment morbidity (i.e. decreased normal tissue complication probability), greater target dose escalation, and the prevention of geographical misses [25,26]. Capturing images during treatment can also be used to detect machine and operator errors.

An image guidance system has several requirements if it is to operate within the environment of an external beam radiation therapy treatment room: good soft tissue contrast; high spatial resolution; short image acquisition time; minimal patient dose; sufficient field of view; and treatment machine integration capabilities [27]. The mainstay of managing position uncertainties has been x-ray imaging. Imaging is easily accomplished in the megavoltage range using the treatment beam itself. However, soft tissue contrast is not achieved leading to the advent of add-on kilovoltage imaging systems. Other efforts have incorporated a CT imager in the treatment room, but this is bulky and delivers a substantial dose to the patient. A strong

candidate technology to satisfy these requirements is ultrasound. Since the late 1960s ultrasound has been a valuable tool in diagnostic radiology and yet it has not been fully realized in radiation therapy. It is a noninvasive, relatively easy, fast, and real-time imaging technique with little discomfort to the patient. In radiation therapy it has been developed to a greater extent for prostate cancer than for other sites, yet promising results using daily ultrasound targeting for patients with upper abdominal, ovarian, bladder, and breast tumours suggest an area for additional trial and study [28-32].

Daily imaging provides knowledge of the position of the target and surrounding tissue that facilitates target positioning under the treatment beams — knowledge that can be used to generate an estimate of the actual delivered dose to the organs. If the patient is repositioned on the treatment couch to account for positioning uncertainties, then the treatment beams intersect a new geometry placing external contour boundaries and tissue densities at positions different from the reference CT image [33]. In this manner, the delivered dose will differ from the planned dose by an unknown amount (as shown in Fig. 8.1) unless daily dose calculations are performed that take into account the image guidance information.

1.5 Proposed work

Despite the widespread use and acceptance of IGRT in radiation oncology clinics, there is still a considerable amount of work to be done. For example daily verification of external photon beams is common, but little work has been done to implement verification for electron beams. In addition, image verification systems generally relate back to the reference CT used for planning the treatment, yet relating a different imaging modality used in the treatment room to the reference CT modality is not straight forward. Recommendations by the International Commission on Radiation Units and Measurements (ICRU) state that the accuracy in dose delivery be within -5% to + 7% [34]. Advancements in technology provide us with the tools to perform daily dose estimates in order to meet these requirements, yet few studies have reported on this information acquired from daily IGRT measurements over the course of a full treatment.

Ultrasound target localization is not yet a fully matured technique. Recent developments in 3D ultrasound and automatic contouring methods have put it on similar footing as other image guidance modalities. However, it's use in IGRT has been primarily limited to the pelvic region.

In this thesis we will explore the application of 3D ultrasound for three different cancer sites and use the information as a dose verification tool. Monte Carlo (MC) methods are used in this work as they are the most accurate method for the determination of absorbed dose.

This thesis consists of five manuscripts that have been either published or submitted to journals. Chapter 2 provides general background information for image guidance in the context of the treatment planning process. Ultrasound IGRT is also reviewed. Chapter 3 is an introduction to the physics of ultrasound and medical ultrasonography. It concludes with an introduction to the ultrasound equipment used in this thesis. Chapter 4 describes how radiation therapy MC dose calculations are performed in this work. Chapter 5 describes in detail the 3D ultrasound system used for all image guidance measurements in this work. The chapter focuses on developing the equipment to image a non-typical treatment site. This work was published in the Proceedings of SPIE: Medical Imaging. Chapter 6 is a follow up study to Chapter 5 that incorporates the ultrasound data into a dosimetric study for head and neck cancer. In Chapter 7 we present proceedings published in the Journal of Physics: Conference Series. It provides the reader with the importance of accurate MC dose calculations, even in an unassuming homogeneous region such as the pelvis. A comparison between MC and analytical algorithms is made for prostate cancer. Chapter 8 is a follow up study to Chapter 7 that incorporates the ultrasound data into a dosimetric study for prostate cancer. This work was published in *Medical Physics*. Chapter 9 uses ultrasound imaging to investigate the pitfalls of electron beam treatment planning and dose delivery for early stage breast cancer. For each treatment site the volume and position of tissue is measured throughout treatment using 3D ultrasound, and MC dose calculations are used to estimate the dose to moving and changing anatomy. This work was published in *Radiotherapy and Oncology*. Finally, Chapter 10 provides a summary of the work presented and suggests context for future work to be done.

1.6 References

[1] Roentgen WC. On a new kind of rays. *Proceedings of the Wuerzburg Physico-Medical Society* 1895

[2] Curie M. Radiations from compounds of uranium and of thorium. *Comptes Rendus* 1898; 126: 1101

[3] Grubbé EH. Priority in the therapeutic use of X-rays. *Radiol* 1993; 21: 156-162

[4] Canadian Cancer Society's Steering Committee. Canadian Cancer Statistics 2009. (Toronto: Canadian Cancer society, 2009)

[5] Johns HE and Cunningham JR. Physics of radiology, Fourth Edition, (Springfield, IL: Charles C. Thomas, 1983)

[6] National Cancer Institute. Radiation Therapy for Cancer: Questions and Answers (Fact Sheet 7.1) 2004

[7] Podgorsak EB and Podgorsak MB. "Stereotactic irradiation," in The modern technology in radiation oncology: A compendium for medical physicists and radiation oncologists. ed J Van Dyk, 589-640 (Madison, WI: Medical Physics Publishing, 1999)

[8] Van Dyk J, Galvin JM, Glasgow, GP, and Podgorsak EB. Physical aspects of rotal and half body irradiation. Report of Task Group 29, Report No. 17 (New York: American Association of Physicists in Medicine, 1986)

[9] Vaeth JM. "Intraoperative radiation therapy in treatment of cancer," in Frontiers of radiation therapy and oncology, Vol. 31. ed JM Vaeth, 1-2 (Basel: Karger, 1997)

[10] Brahme A. Dosimetric precision requirements in radiation therapy. *Acta Radiol Oncol* 1984; 23: 379-91

[11] Brahme A. Optimized radiation therapy based in radiobiological objectives. *Semin Radiat Oncol* 1999; 9: 35-47

[12] Langen KM and Jones DTL. Organ motion and its management. *Int J Radiat Oncol Biol Phys* 2001; 50: 265-278

[13] Mohan R and Bortfeld T. "The potential and limitations of IMRT: A physicist's point of view," in Image guided IMRT. ed T Bortfeld, R Schmidt-Ullrich, W De Neve, and DE Wazer, 11-18 (Germany: Springer-Verlag, 2006)

[14] Shalev S. "Treatment verification using digital imaging," in Radiation therapy physics. ed LW Brady and MD Altschuler, 155-174 (New York: Springer-Verlag, 1996).

[15] Jaffray DA. Image-guided radiation therapy: From concept to practice. *Semin Radiat Oncol* 2007; 17: 243-244

[16] Hounsfield GN. Nobel Award address. Computed medical imaging. *Med Phys* 1980; 7: 283-290

[17] Brahme A, Roos JE, and Lax I. Solution of an integral equation encountered in rotation therapy. *Phys Med Biol* 1982; 27: 1221-1229

[18] Gustafsson A, Lind BK, and Brahme A. A generalized pencil beam algorithm for optimization of radiation therapy. *Med Phys* 1994; 21: 343-356

[19] Boyer AL, Xing L, and Xia P. "Beam shaping and intensity modulation," in The modern technology of radiation oncology: A compendium for medical physicists and radiation oncologists. ed J Van Dyk, 437-479 (Madison, WI: Medical Physics Publishing, 1999)

[20] Yu C. Intensity modulated arc therapy with dynamic multileaf collimation: An alternative to tomotherapy. *Phys Med Biol* 1995; 40: 1435-1449

[21] Mackie TR, Holmes T, Swerdloff S, et al. Tomotherapy: A new concept for the delivery of dynamic conformal radiotherapy. *Med Phys* 1993; 20: 1709-1719

[22] Schweikard A, Glosser G, Bodduluri M, Murphy M, and Adler JR. Robotic motion compensation for respiratory motion in radio-surgery. *Comput Aided Surg* 2000; 5: 263-277

[23] Podgorsak EB and Podgorsak MB. "Special procedures and techniques in radiotherapy," in Radiation oncology physics: A handbook for teachers and students. ed EB Podgorsak, 505-548 (Vienna: International Atomic Energy Agency, 2005)

[24] Yorke ED, Keall PJ, and Verhaegen F. Anniversary paper: Role of medical physicists and the AAPM in improving geometric aspects of treatment accuracy and precision. *Med Phys* 2008; 35: 828-839

[25] Goitein M and Busse J. Immobilization error: Some theoretical considerations. *Radiology* 1975; 117: 407-412

[26] Boyer AL. "Patient positioning and immobilization devices," in Radiation oncology physics. ed JG Kereiakes, HR Elson, and CG Born, 438-446 (New York: American Institute of Physics, 1987)

[27] Jaffray DA and Siewerdsen JH. Cone-beam computed tomography with a flat-panel imager: Initital performance characterization. *Med Phys* 2000; 27: 1311-1323

[28] Fuss M, Salter BJ, and Cavanaugh SX. Daily ultrasound-based image-guided targeting for radiotherapy of upper abdominal malignancies. *Int J Radiat Oncol Biol Phys* 2004; 59: 1245-1256

[29] Featherstone C, Harnett AN, and Brunt AM. Ultrasound localization of the ovaries for radiation-induced ovarian ablation. *Clin Oncol (R Coll Radiol)* 1999; 11: 393-397

[30] Perkins AC, Price HM, and Cox DJ. Ultrasound in the localisation of bladder tumours for radiotherapy treatment planning. *Br J Radiol* 1984; 57: 241-245

[31] Valdagni R, Italia C, and Montanaro P. Clinical target volume localization using conventional methods (anatomy and palpation) and ultrasonography in early breast cancer post-operative external irradiation. *Radiother Oncol* 1997; 42: 231-237

[32] Berrang T, Truong P, Pompescu C, et al. 3D ultrasound can contribute to planning CT to define the target for partial breast radiotherapy. *Int J Radiat Oncol Biol Phys* 2009; 73: 375-383

[33] Beckham WA, Keall PJ, and Siebers JV. A fluence-convolution method to calculate radiation therapy dose distributions that incorporate random set-up error. *Phys Med Biol* 2002; 7: 3465-3473

[34] ICRU (International Commission on Radiation Units and Measurements). Prescribing, recording and reporting photon beam therapy ICRU Report 50 (Bethesda, MD: ICRU, 1993)

CHAPTER 2
Image guided radiation therapy

Radiation therapy planning, verification, and delivery involve a large spectrum of imaging and imaging-based decision making. During the past two decades, the treatment planning process — simulation, organ delineation, plan development, dose calculation, and plan evaluation — has evolved from planning based on planar radiographs to planning based on volumetric image sets. Often there is less information in the treatment room than there is at treatment planning however, advances in imaging are changing this scenario, motivated in part by an overwhelming acceptance of conformal treatment techniques as a standard of care for many sites.

2.1 The radiation therapy treatment planning process

A conventional simulator has been an integral component of the treatment planning process for over 30 years. A simulator is a machine that geometrically mimics the motions and design of a megavoltage (MV) treatment unit (linear accelerator or Co-60), but instead uses diagnostic quality x-rays to image the patient for planning purposes. 2D planar transmission radiographs or fluoroscopic images are acquired at different gantry angles to visualize the resulting treatment fields, defined with delineator wires placed on the patient's surface around the region of interest. The photons produced by the x-ray tube are in the kilovoltage (kV) range and are preferentially attenuated through photoelectric interactions by higher atomic number materials such as bone. The result is a high quality diagnostic radiograph with limited soft tissue contrast, but with excellent visualization of bone, lead wires, and contrast agents. Using primarily bony landmarks, the target area is outlined on the radiographs. The dose to the patient is estimated by scaling tabulated percent depth doses measured in a water tank for the required field size. Shortcomings of the conventional simulation process are analogous to the

shortcomings in initial image guidance systems. Very little anatomy, other than bony anatomy, is visible for the design of treatment fields, and simulators inherently lack volumetric information so that common plan evaluation metrics cannot be computed.

Shortly after the introduction of computed tomography scanners in the early 1970s, they were proposed to replace conventional simulators in the treatment planning process [1-6]. By the 1990s commercial CT simulator packages became available. Anatomical information on CT scans is presented in the form of axial slices to generate a 3D volume. The detectors in a CT scanner are sensitive to the intensity of attenuated photons and provide better grey scale resolution than a radiograph. Because each pixel represents the attenuation coefficient of that tissue relative to water, dose calculations can be computed directly on the images. Early on Goitein et al [3] suggested that CT simulators could mimic images produced from conventional simulators by producing a planar digital radiograph from a projection through the CT data at any angle. This is known as a digitally reconstructed radiograph (DRR), and when it corresponds to a treatment gantry angle it is called the beam's eye view, and provides a reproduction of anatomic features from the viewpoint of the treatment source. Figure 2.1 compares images produced from a conventional and CT simulator. Note that with digitization grey levels, brightness, and contrast can be adjusted to provide an optimal image.

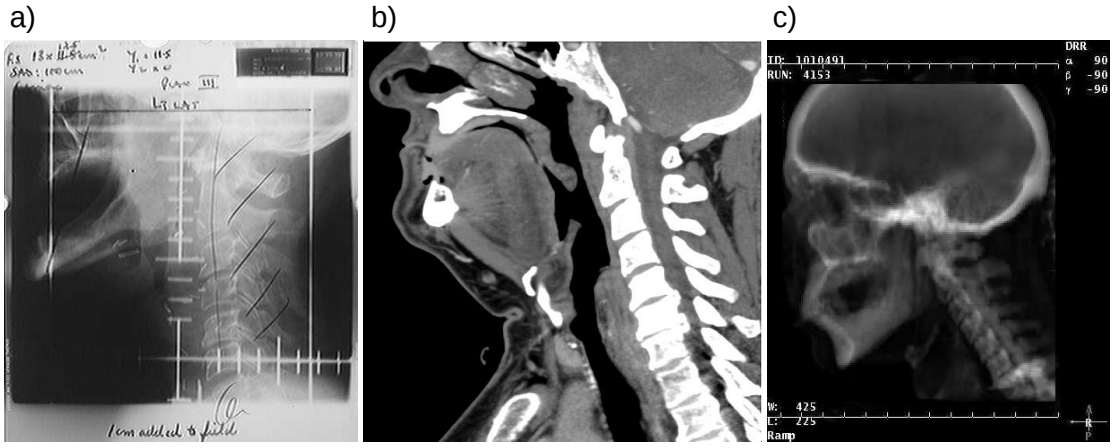

FIG. 2.1 (a) A conventional simulator radiograph for a head and neck patient. The field limits and shielding are indicated on the radiograph. (b) A CT scan. (c) A digitally reconstructed radiograph.

Three features distinguish a CT scanner used for radiation therapy purposes from diagnostic purposes: 1) a flat couch that mimics the treatment unit couch and allows for reproducible patient alignment; 2) a large bore to accommodate various patient positions (for example breast cancer treatment fields often require the arm to be raised above the head); and 3) and a laser system defining the three coordinate axes and isocentre of the CT simulator room. The lasers provide a reference isocentre point between the simulator and treatment rooms. The intersection of the lasers on the patient's skin (or immobilization device) in the simulator room is marked and used as an initial superficial alignment to the lasers in the treatment room.

CT images are helpful for distinguishing between structures that have substantially different x-ray attenuation properties (air, tissue, and bone), but it is difficult to discriminate contiguous soft tissue structures with similar attenuation (for example soft tissue and fluid). This limitation has led to significant inter and intraobserver contouring differences in tumours of the head and neck, prostate, and breast [7-9]. Thus in clinical practice CT images are sometimes used in conjunction with other imaging modalities. Virtually all treatment planning systems (TPS) allow the import and registration of multimodality images to facilitate structure visibility for contouring. Three additional imaging modalities employed in the modern treatment planning process include magnetic resonance imaging, positron emission tomography, and ultrasound imaging. MR provides superior soft tissue contrast but requires long acquisition times and suffers from geometric distortions near the edges of the images [10]. MR images also do not contain information that can be related to electron density so bulk density corrections to heterogenous tissue regions must be applied. PET imaging can come from a stand alone PET scanner or a combined PET/CT unit. The combined unit accommodates the PET and CT scanner in the same housing providing automatic registration between the two image sets [11]. The functional information from PET images can demonstrate disease before it becomes anatomically detectable from a CT image [12], and treatment fields can be defined accordingly. Yet voxels of PET activity are converted to intensity levels so that PET-based tumour volumes are strongly affected by the choice of threshold resulting in substantial differences in target radiation dose. Ultrasound imaging also provides good soft tissue contrast, and it does not use ionizing radiation to acquire images. It is also useful to image sites for which other modalities would suffer from artifacts such as dental fillings in the head and neck region and prosthetics in the pelvic region. Yet, ultrasound imaging does not provide a complete geometrical view of the patient, only localized regions of interest. It also cannot be used to image regions with large differences in

acoustic impedance, such as air-tissue and bone-tissue transitions. For these reasons CT simulators remain the cornerstone of the treatment planning process.

The delineation of critical structures and target volumes is the basis for developing the treatment plan as it guides field shapes, field sizes, beam angles, and treatment technique. The gross tumour volume (GTV) is the clinically visible (from images) or palpable volume. It represents the volume that includes the highest density of tumour cells, and presumably, requires the highest dose in order to be controlled. The clinical target volume (CTV) contains the GTV plus a margin in which tumour cells may reside but which are not appreciated on images. The planning target volume (PTV) is a volume that is fixed in space and contains the CTV plus a margin that includes the best estimate of the daily set-up uncertainty including possible interfraction and intrafraction target motion. It therefore includes normal tissues near the tumour, to which radiation is intentionally delivered. ICRU Reports 50 and 62 guide these volume definitions, yet the extent of margin between the CTV and the PTV is undefined [13,14]. The amount to which the PTV can be reduced will determine the volume of normal tissue receiving high dose, and thus, the maximum level of dose that can be safely delivered to the tumour. If the PTV is fixed in space then the goal is to ensure that the CTV is within the PTV at all times. This requires a consideration of different positioning errors. For example, the CTV might not be rigidly fixed within the patient and might move relative to other tissues because of changes in patient position, breathing, cardiovascular movement, digestion, peristalsis, and variable contents of the bladder, rectum, and stomach. These types of errors can affect the position and/or the shape of the CTV both inter and intrafractionally. The CTV might also change shape and/or size during treatment because of the effects of radiation on the tumour [15]. Portions of the CTV might also be able to move relative to other portions if the CTV rotates around a peripheral point [16]. If permanent marks are made on the surface of the patient to assist in reproducing set-up, errors can occur because the skin can move relative to internal anatomy such as during weight loss or tumour shrinkage. If properly defined, the PTV should include the entire CTV for every fraction of treatment [17].

Conformal radiation therapy has introduced more complex planning and delivery techniques. In 3DCRT, the treatment plan is developed based on trial and error from experienced users — a technique known as forward planning. Modern forward treatment planning combines radiation beam geometries (energy, modifiers, gantry angles, field shaping, etc.) at any orientation on any image to create patient specific treatment plans, which are then compared and evaluated

by the user. To facilitate this process computerized 3D TPS are driven from patient image data sets transferred from the simulation stage. IMRT treatment techniques have changed the process of treatment planning from the design of fields to the design of dose distributions. Treatment plans are not described by general fields in terms of gantry angles, or beam modifiers but instead in terms of treatment goals and prescriptions [18]. Brahme et al [19] were the first to begin with known quantities of prescribed planning results and relate them back to the delivery. Somewhat of a misnomer, inverse planning was later fine tuned using many computerized forward plan iterations [20]. Figure 2.2 illustrates the treatment plan difference between 3DCRT and IMRT techniques for a convex target volume.

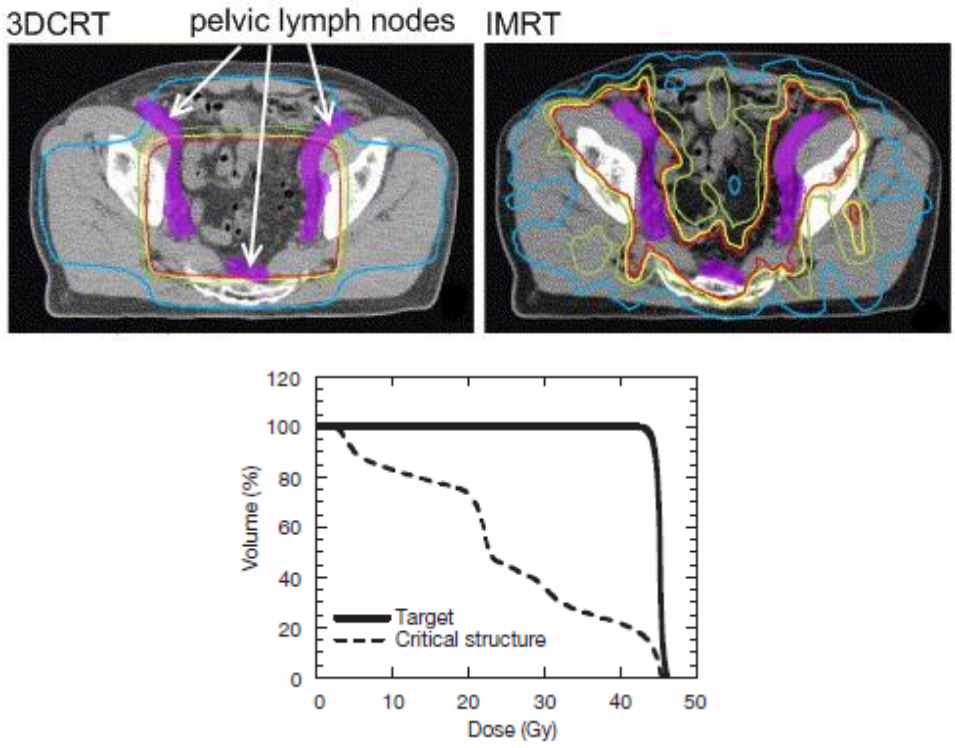

FIG 2.2 Comparison of treatment techniques for pelvic lymph node irradiation. The blue and red lines represent isodose lines for low and high dose, respectively. An example cumulative dose volume histogram for a typical target and critical structure is also shown.

Treatment plans are often evaluated using isodose curves, dose volume histograms (DVH), and dose distribution statistics. An isodose map portrays isodose lines of equal absorbed

dose. The isodose covering the periphery of the target is compared with the isodose at the isocentre, and the ratio is usually within a desired range 95-100% [21]. The purpose of a DVH is to summarize 3D dose distribution information in a graphical 2D format. It represents a frequency distribution of dose values within a defined volume. Rather than displaying the frequency, cumulative DVHs represent the percent of a structure volume receiving at least a particular dose. However, no spatial information is offered; a DVH does not show where within a structure the dose is received. Ideally, 100% of the PTV receives the prescription dose, and organs at risk receive zero dose.

2.2 Rationale for image guidance

Imaging technologies are becoming highly adaptable, allowing integration with treatment delivery instead of being dedicated to planning. Frequent imaging in the treatment room during the course of radiation delivery, image guided radiation therapy, is becoming a crucial requirement for further innovation in conformal techniques, allowing for rigorous delineation and irradiation of tumours. Precision dose painting (a term coined by Ling et al [11]) with high dose gradients is less forgiving in terms of target localization uncertainties, thus warranting accurate positioning and control of organ motion during treatment delivery [23]. Although many factors contribute to radiation therapy failures, retrospective studies have shown a strong correlation between local recurrence and inadequate high dose coverage of the target volume [24,25]. IGRT acquires instant knowledge of target location and geometry during treatment in order to better align the patient under the treatment beam. Image guidance is an important link and a major player in the treatment chain.

The 3D image acquired during CT simulation is but a snapshot in time, whereas a course of radiation therapy may begin a few weeks after planning image acquisition, and last up to six weeks, so that long term geometrical changes may necessitate replanning. Verification imaging may lead to repositioning if gross misalignments are detected. But the benefits of frequent in-room imaging do not stop at patient alignment. Verification imaging creates a record for quality assurance and educates staff on treatment practices and geometric uncertainties. Large set-up errors are more likely to be detected with frequent imaging, and interventions to reduce errors could be implemented sooner than usual [26]. Imaging at the time of treatment might also increase awareness of the range of organ motion, set-up errors, and changes in tumour size and shape that take place in time frames relevant to radiation therapy. For example, the varying position of the prostate every day has been correlated with bladder and rectum filling [27-29]

leading to recommendations for patient preparation before treatment. A study using cine MR imaging reported intrafractional prostate motion up to 11.7 mm along the superior-inferior direction during a 9 minute time frame [30]. Another reported that 29% of patients exhibited anterior-posterior prostate displacements exceeding 5 mm [31]. In the head and neck region weight loss may have led to an increase in spinal cord dose that was detected only in the presence of frequent imaging [32]. Another example demonstrated that IGRT and adaptive replanning of lung cancer resulted in an average reduction of 21% in the volume of healthy lung receiving 20 Gy or more, with a resultant reduction in the risk of toxicity [33].

In combination with IMRT, IGRT has paved the way for more aggressive treatment schedules especially in sites in which normal structure complications limit dose escalation. Classic radiation schedules use daily fractions of 1.8-2 Gy for a total of approximately 70 Gy. These schedules are a burden for patients requiring daily visits to the hospital and demand a lot of machine time. The concept of delivering partial tumour boosts was developed some years ago [34], but hypofractionation is only now being translated to the clinic [35,36]. Some authors have reported late toxicity effects in breast cancer hypofractionation [37,38] making frequent in-room imaging, ideally nonionizing imaging, even more important.

IGRT techniques have also been used to reduce the impact of short term motion such as breathing. One solution to the management of mobile tumours is to gate the radiation beam so that radiation is delivered only at a specific time during the breathing cycle, such as full inhale or full exhale. Another method that does not require patient intervention and active breathing control is beam tracking, which images the target and follows it dynamically with the radiation beam on [39]. IGRT combined with beam tracking was first implemented in a robotic radiosurgery system (CyberKnife, Accuray Inc., Sunnyvale, CA) [40-42].

2.3 Geometrical uncertainties and margins

In radiation therapy there are many error sources that act during treatment preparation and execution to limit delivery accuracy. The CTV contour represents the target volume to be irradiated as it contains malignant disease and areas susceptible to malignant disease. However, the geometrical errors in target delineation, patient set-up variation, organ motion, and beam set-up require a safety margin to ensure that the planned dose is actually delivered to the CTV for (almost) all patients.

As working definitions, uncertainty refers to the standard deviation of a set of measurements, and error refers to any known deviation between planned and executed treatment

[43]. ~~Therefore, there should be a known probability of the error lying somewhere within the range of uncertainty [44].~~ Geometric uncertainties in radiation therapy are often divided into systematic and random errors. Systematic error exists because the simulation target position may differ from the average target position. Random error is the day-to-day deviation from the average target position. Of the two, systematic errors are more important because, if uncorrected, would be propagated throughout treatment. As to random error, its detrimental effect is usually smaller, and may already be accounted for in the safety margin [43,45].

Delineation uncertainty is a purely systematic error as it affects all treatment fractions in the same manner. Delineation of the target volume depends on the imaging modality, the resolution of the image [46], and intra and interobserver effects [47-48]. These effects are due to differences in the interpretation of simulator images. Patient set-up variation has systematic and random components. In particular, motion of skin over skeletal structure limits the reproducibility of aligning the patient to the room lasers based on surface marks. Efforts to improve this step include rigid immobilization devices, such as a mesh mask for head and neck cancers [49]. Well defined set-up protocols have enabled some clinics to achieve a set-up uncertainty of 2 mm in each direction for prostate cancer [50]. Organ motion also has systematic and random components. For target volumes near the lung or diaphragm, tumour movement with 2-3 cm amplitude has been reported [51]. Particular to these lesions is that the images may also be blurred due to respiratory and cardiac motion. Another form of geometric error that impacts patient positioning is the calibration of the simulation and treatment rooms' isocentre and laser coordinate system. These are usually specified to be accurate within 1 mm [52].

It has become common practice to specify target localization errors (set-up and organ motion) in terms of the safety margins that would be required to encompass the CTV at every fraction if image guidance was not used. The components of the margin calculations are shown in Fig 2.3. Assume that for a population of patients image guidance was used to determine the daily CTV position with respect to the planning position determined at simulation. The mean and standard deviation (SD) of daily errors (displacement from the planning position) are determined per patient (patient mean and patient SD). The group systematic error (M) is then the mean of all patient means. Ideally M should be zero, but in reality it is a function of how well the situation at planning represents that at treatment. The systematic (interpatient) error (Σ) is the SD of all patient means. Σ is sometimes called the preparation error because it describes how

reproducible treatment preparation is performed. The random (intrapatient) error (σ) is the root mean square average of patient SDs and represents the execution error [43].

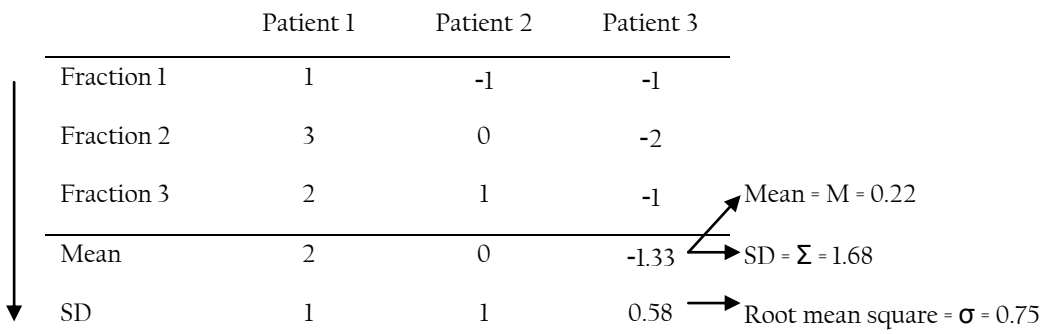

FIG. 2.3 The components of systematic and random target positioning errors used in margin calculations.

Several margin recipes have been published, and later on refined over the years. In 1995 Austin-Seymour et al described a margin taking into account patient set-up, patient motion, and lung tumour motion by cylindrically expanding the CTV [53]. Bel et al proposed methods of producing a PTV assuming rigid body translations and rotations of the CTV [54]. They showed through simulation that a margin for random deviations of 0.7σ is adequate to maintain 95% dose coverage, which was later shown to be treatment technique specific [55]. Killoran et al introduced the concept of probability of prescription dose using numerical simulations [56]. The margin was iterated to ensure coverage up to a given dose for a given fraction of the patient population. Fontenla et al described how margins may be optimized on the basis of not only target volume coverage but also on normal tissue irradiation [57]. Stroom et al was one of the first groups to use coverage probability to derive margins [58]. Their equation $2\Sigma + 0.7\sigma$ was specific to the prostate PTV and was formulated from the criterion that on average more than 99% of the CTV should receive at least 95% of the prescribed dose. The authors used clinically shaped CTVs and clinical dose distributions in its derivation. Some authors have incorporated biological parameters in their margin recipes, such as tumour control probability [59-61]. One of the more well known margin recipes, also derived from measured prostate errors, $2.5\Sigma + 0.7\sigma$, was introduced by van Herk et al to guarantee that 90% of patients in the population receive a

minimum cumulative CTV dose of at least 95% of the prescribed dose [62]. Although one of the more rigorously developed recipes, the authors assumed a spherical CTV, did not take into account organ rotation or deformation in addition to translation, and they warn that this approximation is only valid for a given beam penumbra used in their work. Note that Σ and σ are vectors allowing the equation to be used for defining nonisotropic margins.

Margin recipes have also been derived for more specific applications such as respiration and external electron beam techniques. Equations that consider respiration motion often weight the peak-to-peak amplitude of the breathing cycle more heavily than systematic and random errors [63-66]. A guideline for CTV to PTV expansion for electron beams was presented in ICRU Report 72 [67]. However, the method is based on Stroom et al's work, which makes a number of assumptions that do not hold for electron beams [68]. Stroom et al and van Herk et al assumed that the treatment plan beam arrangement would conform the dose distribution to the target in three dimensions. The more usual situation in external electron beam therapy is to use a single field of beam energy appropriate to the depth required to ensure adequate PTV coverage. The effect of geometrical errors parallel to the beam will be very different from the effect of geometrical errors nonparallel to the beam. Moreover, unlike photon beams, the width of an electron beam penumbra is larger and varies more rapidly with depth and energy.

2.4 The effect of geometric errors on the dose

~~It is well known that set-up errors and organ motion compromise the accuracy of the planned dose delivery [69]~~. Set-up errors and organ motion will cause the dose distribution to be shifted and blurred. One method of evaluating the impact of random motion on the delivered dose is to convolve the static treatment plan with a Gaussian blur probability density function (PDF) that describes random motion [70]. This method assumes the Gaussian is centered at zero and so does not consider systematic offsets. Whereas the blurring of the dose distribution because of random errors (or respiration) over a large number of fractions is predictable, systematic motion will be unknown for each patient until it is actually measured [43]. Undoing these effects by correcting for motion will still cause the dose distribution to differ from that planned. This is because the patient is initially aligned with skin marks as they were in the CT simulator room. Realigning the patient by shifting the treatment couch may bring the target back to the isocentre but it has also changed the position of the external surface and internal anatomy interfaces with respect to the beam. The target may now be at a different depth and the beams may pass through different tissue heterogeneities.

2.5 Different approaches to image guided radiation therapy

2.5.1 Online and offline techniques

In general, image guided decisions and adjustments can be grouped into two categories: online and offline. An online correction approach refers to immediate intervention. That is, frequent (can be at every fraction) interfraction images are acquired in the treatment room, in the treatment position, and after initial skin alignment to the room lasers. The images are immediately evaluated on the basis of predefined thresholds by comparing the current image to the reference image captured at simulation. If deemed necessary, translations of the treatment couch are the most frequent method to adjust for positional offsets of the target. Rotational corrections are possible using specialized couches, but this is not routine [71]. Alternatively, an offline approach refers to the acquisition of frequent images without immediate intervention. After a small number of fractions have been delivered, the systematic component of geometric uncertainty can be calculated, and a correction applied by repositioning the treatment couch by the same amount for all future fractions [72,73]. There is general agreement that 3-5 imaging sessions would be sufficient for the correction of systematic error, with subsequent periodic (i.e. weekly) checks for additional assurance, allowing for a large step in margin reduction with limited workload [74,75]. An advantage of online corrections is that both systematic and random errors are corrected efficiently. A disadvantage is that analysis and corrections must be fast, simple, and unambiguous. The rationale for offline correction strategies is that margin requirements are dominantly determined by systematic errors and much less by random errors. Approaches resulting in adaptation of machine or treatment parameters are referred to more generally as adaptive radiation therapy (ART) [76].

Beam tracking is inherently an adaptive approach where the radiation beam itself is moved and the patient remains stationary. The CyberKnife system continuously monitors and tracks the target during radiation delivery such that intrafraction motion is accounted for [77]. Gated radiation therapy [78] and active breathing control techniques [79] are alternate methods to tumour tracking. For example, the conventional solution to correct for respiratory motion is to expand the PTV, but if the time-averaged tumour position is accurately known then the required margin for respiration is relatively small [63,80].

2.5.2 Registration methods and segmentation

An extremely important feature of IGRT is the ability to register the daily images to a reference image set in order to compare or integrate data obtained from different measurements. Image registration involves spatially transforming the daily image to align with the reference image. Linear, or rigid, transformations include translation, rotation, and scaling. Linear transformations are global in nature and cannot model local geometric differences between images. Non-rigid, or deformable, transformations are capable of locally warping the daily image to align with the reference image [81]. Rigid registration has been successfully applied to radiation oncology practice and is familiar to most practitioners. Deformable registration is more complicated because it entails modeling voxel dependent distortion. Registration can be performed via manual, landmark-based, surface-based, or intensity-based techniques [82].

Computerized segmentation also plays a role in registration if the transformation between two image sets is based on the centre of mass or the surface of a reference organ. In most cases segmentation is performed manually in a slice-by-slice fashion such that daily manual segmentation becomes unrealistic and is prone to interobserver discrepancies. Automatic segmentation methods include using threshold or greyscale information, which represent good examples of a intensity-based method, or using an a priori physical model of the region of interest with a deformable external boundary, which represents a good example of a model-based method [83].

2.5.3 Evolution of image guided modalities

In early approaches, the patient was positioned before treatment by inferring the location of internal anatomy from skin marks. At this time, the emphasis of positioning accuracy was mostly focused toward immobilization, and applying conservative margins ensuring target coverage, rather than toward imaging. In these days in-room imaging was mainly used to verify immobilization techniques and not as a positioning technique on its own [84]. The most widespread method to image internal anatomy at the time of treatment used the MV treatment beam itself. In 1988 the Canada Post Corporation produced a commemorative stamp, illustrating the early adoption of verification imaging with the introduction of Co-60 treatment machines. In FIG 2.4 a diagnostic x-ray tube is shown mounted to the right of a 1951 machine head in order to obtain good-quality images from the perspective of the therapy beam [85,86].

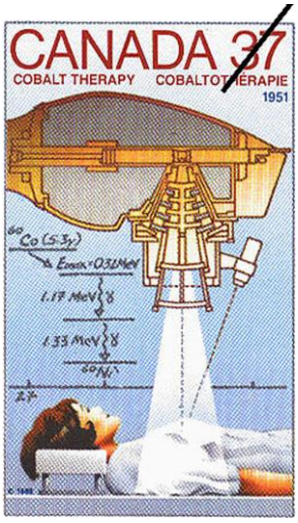

FIG. 2.4 A Canada Post Corporation commemorative stamp produced in 1988.

Initially radiographic film was used but it was not so common in the era before linacs. Analysis of these port films was difficult, tedious, prone to error, and time consuming. Various deficiencies included delay in film development, low contrast, noise associated with film granularity, batch-to-batch inconsistencies, susceptibility to under and over exposure, and poor resolution due to the source size of the Co-60 device [87]. Rabinowitz et al reported limiting the number of patients verified with radiographic film to a maximum of two per treatment unit per day as it would otherwise impact workflow [88]. A matrix ionization chamber was suggested as an improvement [89], and methods had been described to optimize film radiography with metal or luminescent screens [90]. The logical future development was to bypass the use of films and obtain images directly in electronic format [91].

Digital non-film technology began in the 1980s and became widespread in the 1990s. Electronic portal imaging devices (EPID) were soon reported to be used for daily or weekly online corrections [92,93]. EPIDs are a planar IGRT technology mounted to the treatment delivery system distal to the patient (Fig. 1.1). In this respect the imaging isocentre is identical to the treatment isocentre and multiple gantry positions can be used to obtain 3D information [94]. Moreover, an EPID can be used for dose measurements making it a valuable tool for quality assurance and dosimetric treatment verification [95,96]. Nevertheless, there are two shortfalls of MV portal imaging similar to conventional simulators. First of all, planar images are acquired and registered to a volumetric CT image. This is approximated by aligning DRRs and in-room MV x-rays as if they were each 2D images, limiting the ability to assess rotational changes in

target position. Cone beam CT (CBCT) is a new technology which generates 3D images from 2D portal projections. Swindell et al first proposed to use the treatment beam to perform MV computed tomography of the patient in the treatment position [97]. The cone beam implementation of that idea was first investigated by Mosleh-Shirazi et al [98]. During MV CBCT acquisition the treatment beam collimation is opened to a large field to encompass the whole field of view of the patient, and the EPID is used to obtain 2D projections. In this manner CBCT operates on the same principles as CT systems, except that it allows a volumetric CT image to be reconstructed from data collected during a single gantry rotation.

Second of all, MV imaging still suffers from detectors that have poor detection quantum efficiency in the MV energy range resulting in a poor signal-to-noise ratio. Soft tissue contrast is also reduced because the primary interaction in human tissue in the MV treatment range is Compton scattering. MV images primarily show skeletal anatomy and some features with sharp density changes from surrounding tissue (lung, trachea, skin) [100]. A surrogate set of anatomic landmarks are sometimes used to infer target position. For some anatomy, reasonable surrogates exist (for example, the skull for a tumour in the brain), but others are less certain (for example, the prostate). Target visualization has been enhanced by implanting radio opaque fiducials in or near the tumour. The fiducials are not only highly visible, but generally present a simpler geometric object such as a point or a line, thus enhancing the reproducibility of alignment. More recently, radiofrequency transponders have been developed that can be inserted in or near the tumour. These systems are coupled with a local antenna array in the treatment room that can sense and locate the transponders relative to the treatment beam real-time [100]. Alternatively, the approach of using diagnostic kV x-rays for treatment set-up verification is not new. kV CBCT uses conventional x-ray tubes that are typically mounted perpendicular to the gantry head with an opposing flat-panel detector (see Fig. 1.1). While MV CBCT may offer advantages in terms of less radiation scatter, less imaging artifacts due to the presence of metal, and simplicity of mechanical integration with a linear accelerator, kV CBCT offers significant performance advantages such as improved image quality (because of the larger differences in the attenuation coefficient in tissues), reduced patient dose compared to daily MV imaging, and the ability to be used in fluoroscopic mode during treatment [101]. Despite these clinical advantages, kV CBCT also suffers from a high degree of scatter as well as artifacts due to the presence of large heterogeneities [102].

Room mounted kV x-ray imaging sources have also recently been introduced [103,104]. The x-ray sources and imagers are fixed on either the floor or ceiling. Being independent of the

beam delivery device, they are particularly stable and suitable for real-time internal fiducial marker tracking allowing motion management during treatment.

A kV imaging modality that is widely accepted and familiar to radiation oncology departments is a CT scanner. Some clinics have installed CT scanners directly in the treatment room (CT-on-rails) in order to register images of the same modality [105-107]. In this manner the CT and linac share a common treatment couch minimizing patient motion between position verification and treatment. Integrated in-room MR systems are also under development yet none have reached commercial application [108,109]. Recently a design has resolved the mutual interference between the MR imager and linac such that the MR imager's magnetic field does not interfere with the trajectory of electrons in the linac waveguide, and the radiofrequency signals from each system do not interfere with the operation of the other system [110].

2.6 Ultrasound based localization

Ultrasound based localization reserves a unique role in radiation therapy. It does not use ionizing radiation to produce an image, and is second only to portal imaging in its age since commercial clinical implementation [111]. It is one of two modalities that provides intramodality image registration of simulation and in-room images, and it was one of the first to provide for routine volumetric imaging at treatment delivery, the other being in-room CT. It has been instrumental in the development of IGRT and has substantially advanced prostate localization and dose escalation studies.

Ultrasound imaging was the first effective soft tissue imaging modality used in diagnostic radiology as it provided tomographic views of anatomy, and it is now one of the most widely used diagnostic imaging modalities. After the introduction of ultrasound, CT and MR were introduced for disease diagnosis and management, yet ultrasound imaging retained its unique advantages of real-time imaging (without delivering a dose, unlike fluoroscopy), low cost, relative ease of use, and the equipment was small enough that it could be moved between rooms [112]. These advantages were carried over into radiation therapy with the introduction of 2D transrectal ultrasonography — a relatively new imaging modality in 1990. One of the earlier studies on ultrasound IGRT in 1996 was to determine whether a real-time ultrasound imaging and targeting system for the treatment of prostate cancer was feasible [113]. The initial phase of the project included a study to develop and determine software for the fusion of ultrasound images to standard CT images, and to determine the potential reduction in conventional field sizes with real-time imaging. It was determined that lateral field sizes could be reduced up to

47%. The authors also concluded that prostate position could be determined with certainty on a regular basis with transrectal ultrasonography, the amount of normal tissue in high dose volumes could be reduced, and that this approach may reduce acute and chronic morbidity to allow for dose escalation.

Image guidance for prostate cancer has been a leading application of ultrasound imaging in radiation therapy because of the prostate's accessibility for imaging in this modality. In brachytherapy advances in transrectal ultrasound image reconstruction [114], robotic aids [115], and radioactive seed segmentation [116] permitted prostate planning, guiding, and seed implantation in the same session, thereby avoiding problems of repositioning, prostate motion, and prostate size/contour changes between the preplan and implantation. In external beam radiation therapy transabdominal ultrasound imaging is an online image guidance technique that uses rigid registration. It has been used for upper abdominal and pelvic tumour IGRT. In the abdomen, sites such as liver, gall bladder, pancreas, and retroperineal tumours have successfully been imaged with ultrasound and registered to the reference CT scan, allowing for individualized reduction of safety margins due to improved daily target alignments [117,118]. Transabdominal ultrasound had an important impact on, and had become the de facto standard in, daily targeting for prostate cancer [117]. Some of the reasons for ultrasound's popularity was that it was a non-radiographic localization tool, did not require a surrogate to visualize the target, images could be acquired without leaving the treatment room, and localization could be completed within five minutes [119].

The first commercial implementations of transabdominal ultrasound used 3D localizing systems, but visualization was only in two dimensions. A 3D visualization system came a few years later, and was also equipped with site specific semi-automatic segmentation and intramodality registration capabilities (Restitu (Resonant Medical Inc., Montreal, QC)). Intramodality position verification was made possible by installing a second ultrasound system directly in the CT simulation room. Not only could ultrasound images in the simulation room be compared with the treatment room ultrasound images, but because they shared a common coordinate system with the CT simulator they were implicitly registered to the CT images and could aid in target delineation. It has been reported that intramodality registration may be more accurate [120], as different imaging modalities portray the same organ with different shapes and sizes [121-123].

Subsequent to 1996, advancements paved the way for more aggressive treatment schedules and significantly helped to reduce complications. Well known examples are the dose

escalation protocols in prostate cancer, which resulted in improved biochemical control rates while preventing an increase in rectal and bladder complications [124,125]. Ghilezan et al showed that "perfect" targeting of the prostate permitted an average increase in dose of 13% while maintaining an equivalent risk of rectal toxicity. Importantly, the spread of individual gains through IGRT varied by more than 30%, indicating that patient specific geometric factors weigh heavily on the actual benefit of image guidance, a result also found in this thesis (Chapter 8) [126].

Soon after the introduction of ultrasound in radiation therapy, it's localization measurements were compared to other methods, notably with portal imaging and prostate implanted fiducial markers [127-129], and with CT [130]. X-ray imaging with fiducial markers is not resistant to errors as the number and location of implanted markers affect the accuracy and reliability of daily alignment [131], and the markers have been reported to migrate over time [132]. A conclusion can be drawn that prostate imaging modalities have been compared only to find that they are not inter-replaceable. It has also been reported that the act of acquiring an ultrasound image may displace the prostate due to the pressure from the transducer on the patient's lower abdomen [133]. More recent studies have reported that displacement due to probe pressure is negligible [134]. It has been argued that ultrasound imaging is susceptible to interobserver effects [135], yet as with any new technology, experience is correlated with high interobserver consistency and improved reproducibility [136]. On the other hand ultrasound imaging has been shown to have less interobserver delineation variation than CT for breast cancer [137], and it has been predicted that further community experience with 3D ultrasound will improve its accuracy [138].

2.7 References

[1] Thatcher M. Treatment simulators and computer assisted tomography. *Br J Radiol* 1977; 50: 294

[2] Goitein M and Abrams M. Multi-dimensional treatment planning; 1. Delineation of anatomy. *Int J Radiat Oncol Biol Phys* 1983a; 9: 777-787

[3] Goitein M, Abrams M, Rowell D, Pollari H, and Wiles J. Multi-dimensional treatment planning; 2. Beam's eye-view, back projection, and projection through CT sections. *Int J Radiat Oncol Biol Phys* 1983b; 9: 789-797

[4] Sherouse G, Mosher KL, Novins K, Rosenman EL, and Chaniey EL. "Virtual simulation; concept and implementation," in Ninth International Conference on the Use of Computers in Radiation Therapy. ed IAD Buinvis, PH van der Giessen, HJ van Kleffens, and FW Wittkamper, 433-436 (The Netherlands: North-Holland Publishing, 1987)

[5] Sherouse GW, Novins K, and Chaney EL. Computation of digitally reconstructed radiographs for use in radiotherapy treatment design. *Int J Radiat Oncol Biol Phys* 1990a; 18: 651-658

[6] Sherouse GW, Bourland JD, and Reynolds K. Virtual simulation in the clinical setting; some practical considerations. *Int J Radiat Oncol Biol Phys* 1990b; 19: 1059- 1065

[7] Hermans R, Feron M, Bellon E, Dupont P, Van den Bogaert W, Baert AL. Laryngeal tumor volume measurements determined with CT: a study on intra- and interobserver variability. *Int J Radiat Oncol Biol Phys* 1998; 40: 553-557

[8] Cazzaniga LF, Marinoni MA, Bossi A, et al. Interphysician variability in defining the planning target volume in the irradiation of prostate and seminal vesicles. *Radiother Oncol* 1998; 47: 293-296

[9] Hurkmans CW, Borger JH, Giersbergen A, Cho J, Mijnheer BJ. Variability in target volume delineation on CT scans of the breast. *Int J Radiat Oncol Biol Phys* 2001; 50: 1366-1372

[10] Purdy JA, Vijayakumar S, Perez CA, and Levitt SH. "The simulation process in the determination and definition of the treatment volume and treatment planning," in

Technical basis of radiation therapy; Practical clinical applications. ed LW Brady, SH Levitt, JA Purdy, and CA Perez, 107-134 (Berlin: Springer-Verlag, 2008)

[11] Beyer T, Townsend DW, Brun T, et al. A combined PET/CT scanner for clinical oncology. *J Nucl Med* 2000; 41: 1369-1379

[12] Dizendorf EV, Baumert BG, Schulthess GK von, Lutolf UM, and Steinert HC. Impact of whole-body 18F-FDG PET on staging and managing patients for radiation therapy. *J Nucl Med* 2003; 44: 24-29

[13] ICRU (International Commission on Radiation Units and Measurements). Prescribing, recording and reporting photon beam therapy ICRU Report 50 (Bethesda, MD: ICRU, 1993)

[14] ICRU (International Commission on Radiation Units and Measurements). Prescribing, recording and reporting photon beam therapy (supplement to ICRU Report 50) ICRU Report 62 (Bethesda, MD: ICRU, 1999)

[15] Wang ZH, Yan C, Zhang ZY, et al. Radiation-induced volume changes in parotid and submandibular glands in patients with head and neck cancer receiving postoperative radiotherapy: a longitudinal study. *Laryngoscope* 2009; 119: 1966-1974

[16] Li JS, Jin L, Pollack A, et al. Gains from real-time tracking of prostate motion during external beam radiation therapy. *Int J Radiat Oncol Biol Phys* 2009; Epub ahead of print doi:10.1016/j.ijrobp.2009.05.022

[17] Verhey LJ. Immobilizing and positioning patients for radiotherapy. *Semin Radiat Oncol* 1995; 5: 100-114

[18] Langer M. "What is different about IMRT?," in Intensity–modulated radiation therapy; The state of the art. ed JR Palta and TR Mackie, 199- 221 (Madison, WI: Medical Physics Publishing, 2003)

[19] Brahme A, Roos JE, and Lax I. Solution of an integral equation encountered in rotation therapy. *Phys Med Biol* 1982; 27: 1221-1229

[20] Webb S. "Historical Perspective on IMRT," in Intensity–modulated radiation therapy; The state of the art. ed JR Palta and TR Mackie, 1-23 (Madison, WI: Medical Physics Publishing, 2003)

[21] Parker W and Patrocinio H. "Clinical treatment planning in external photon beam radiotherapy," in Radiation oncology physics; A handbook for teachers and students. ed EB Podgorsak, 219-272 (Vienna: International Atomic Energy Agency, 2005)

[22] Ling CC, Humm J, Larson S, et al. Towards multidimensional radiotherapy (MD-CRT); biological imaging and biological conformality. *Int J Radiat Oncol Biol Phys* 2000; 47: 551-560

[23] Verellen D, De Ridder M, and Storme G. A (short) history of image-guided radiotherapy. *Radiother Oncol* 2008; 86: 4-13

[24] Doss LL. "Localization error and local recurrence in upper airway carcinoma," in Workshop on Quality Control in the Radiotherapy Departments of the Cancer and Leukemia Group B (CALGB). ed Reinstein LE (New York, 1979)

[25] Kinzie JJ, Hanks GE, Madean CJ, et al. Patterns of care study; Hodgkin's disease relapse rates and adequacy of portals. *Cancer* 1983: 52; 2223-2226

[26] Dawson L and Sharpe MB. Image-guided radiotherapy; rationale, benefits, and limitations. *Lancet Oncol* 2006; 7: 848-858

[27] Beard CJ, Kijewski P, Bussiere M, et al. Analysis of prostate and seminal vesicle motion; Implications for treatment planning. *Int J Radiat Oncol Biol Phys* 1996; 34;451-458

[28] Zelefsky MJ, Crean D, Mageras GS, et al. Quantification and predictors of prostate position variability in 50 patients evaluated with multiple CT scans during conformal radiotherapy. *Radiother Oncol* 1999; 50: 225-234

[29] Zellars RC, Roberson PL, Strawderman M, et al. Prostate position late in the course of external beam therapy; Patterns and predictors. *Int J Radiat Oncol Biol Phys* 2000; 47: 655-660

[30] Mah D, Freedman G, Milestone B, et al. Measurement of intrafractional prostate motion using magnetic resonance imaging. *Int J Radiat Oncol Biol Phys* 2002; 54;568-575

[31] Padhani AR, Khoo VS, Suckling J, et al. Evaluating the effect of rectal distension and rectal movement on prostate gland position using cine MRI. *Int J Radiat Oncol Biol Phys* 1999; 44: 525-533

[32] Hong TS, Tome WA, Chappell RJ, et al. The impact of daily set-up variations on head-and-neck intensity-modulated radiation therapy. *Int J Radiat Oncol Biol Phys* 2005; 61: 779-788

[33] Ramsey CR, Langen KM, Kupelian PA, et al. A technique for adaptive image-guided helical tomotherapy for lung cancer. *Int J Radiat Oncol Biol Phys* 2006; 64: 1237-1244

[34] Goitein M, Niemierko A, and Okunieff P. "The probability of controlling an inhomogeneously irradiated tumor," in Quantitative imaging in oncology, Proceedings of the 19th LH Gray Conference. ed K Kaulner, B Carey, A Crellin et al, (London: British Institute of Radiology, 1995; 25-32)

[35] Budrukkar A. Accelerated partial breast irradiation; an advanced form of hypofractionation. *J Cancer Res Ther* 2008; 4: 46-47

[36] Whelan TJ, Kim DH, and Sussman J. Clinical experience using hypofractionated radiation schedules in breast cancer. *Semin Radiat Oncol* 2008; 18: 257-624.

[37] Dolinsky C and Glatstein E. Some cases of severe normal tissue toxicity can be anticipated with ablated fractionated radiation with appropriate long-term follow-up. *Semin Radiat Oncol* 2008; 18: 229-233.

[38] Friberg S and Ruden BI. Hypofractionation in radiotherapy. An investigation of injured Swedish women, treated for cancer of the breast. *Acta Oncol* 2009; 4: 1-10

[39] Murphy MJ. Tracking moving organs in real time. *Semin Radiat Oncol* 2004; 14: 91-100

[40] Adler JR, Murphy MJ, Chang SD, et al. Image-guided robotic radiosurgery. *Neurosurgery* 1999; 44: 1299-1306

[41] Schweikard A, Glosser G, Bodduluri M, et al. Robotic motion compensation for respiratory movement during radiosurgery. *Comput Aided Surg* 2000; 5: 263-277

[42] Murphy MJ, Chang SD, Gibbs IC, et al. Patterns of patient movement during frameless image-guided radiosurgery. *Int J Radiat Oncol Biol Phys* 2003; 55: 1400-1408

[43] Van Herk M. Errors and margins in radiation therapy, *Semin Radiat Oncol* 2004; 14: 52-64

[44] Wilkinson JM. Geometric uncertainties in radiotherapy. *Br J Radiol* 2004; 77: 86-87

[45] Yan D, Lockman D, Martinez A, et al. Computed tomography guided management of interfractional patient variation. *Semin Radiat Oncol* 2005; 15: 168-181

[46] Links JM, Beach LS, Subramaniam B, et al. Edge complexity and partial volume effects. *J Comput Assist Tomogr* 1998; 22: 450-458

[47] Dubois DF, Prestidge BR, Hotchkiss LA, et al. Intraobserver and interobserver variability of MR imaging- and CT-derived prostate volumes after transperineal interstitial permanent prostate brachytherapy. *Radiology* 1998; 207: 785-789

[48] Fiorino C, Reni M, Bolognesi A, et al. Intra- and interobserver variability in contouring prostate and seminal vesicles; Implications for conformal treatment planning. *Radiother Oncol* 1998; 47: 285-292

[49] Weltens C, Kesteloot K, Vandevelde G, et al. Comparison of plastic and Orfit masks for patient head fixation during radiotherapy; Precision and costs. *Int J Radiat Oncol Biol Phys* 1995; 33: 499-507

[50] Hurkmans CW, Remeijer P, Lebesque JV, et al. Set-up verification using portal imaging: review of current clinical practice. *Radiother Oncol* 2001; 58: 105-120

[51] Seppenwoolde Y, Shirato H, Kitamura K, et al. Precise and real-time measurement of 3D tumor motion in lung due to breathing and heartbeat, measured during radiotherapy. *Int J Radiat Oncol Biol Phys* 2002; 53: 822-834

[52] Podgorsak EB, Metcalf P, and Van Dyk J. "Medical accelerators," in Modern Technology of Radiation Oncology; A Compendium for Medical Physicists and Radiation Oncologists. ed J Van Dyk, (Madison, WI: Medical Physics Publishing, 1999)

[53] Austin-Seymour M, Kalet I, McDonald J, et al. Three dimensional planning target volumes; a model and a software tool. *Int J Radiat Oncol Biol Phys* 1995; 33: 1073-1080

[54] Bel A, van Herk M, and Lebesque JV. Target margins for random geometrical treatment uncertainties in conformal radiotherapy. *Med Phys* 1996; 23: 1537-1545

[55] McKenzie AL, van Herk M, Mijnheer B. The width of margins in radiotherapy treatment plans. *Phys Med Biol* 2000a; 45: 3331-3342

[56] Killoran JH, Kooy HM, Gladstone DJ, et al. A numerical simulation of organ motion and daily set-up uncertainties; Implications for radiation therapy. *Int J Radiat Oncol Biol Phys* 1997; 37: 213-221

[57] Fontenla E, Pelizzari CA, and Chen GTY. Implications of 3-dimensional target shape and motion in aperture design. *Med Phys* 1996; 23: 1431-1441

[58] Stroom JC, de Boer HC, Huizenga H, et al. Inclusion of geometrical uncertainties in radiotherapy treatment planning by means of coverage probability. *Int J Radiat Oncol Biol Phys* 1999; 43: 905-919

[59] Aaltonen P, Brahme A, Lax I, et al. Specification of dose delivery in radiation therapy. Recommendation by the Nordic Association of Clinical Physics (NACP) (suppl). *Acta Oncol* 1997; 36: 1-32

[60] Craig T, Battista J, Moiseenko V, et al. Considerations for the implementation of target volume protocols in radiation therapy. *Int J Radiat Oncol Biol Phys* 2001; 49: 241-250

[61] van Herk M, Witte M, van der Geer J, et al. Modeling the effect of treatment uncertainties in radiotherapy on tumor control probability for different tumor cell density configurations [Abstract]. *Int J Radiat Oncol Biol Phys* 2003a; 55: 447

[62] van Herk M, Remeijer P, Rasch C, and Lebesque JV. The probability of correct target dosae; Dose-population histograms for deriving treatment margins in radiotherapy. *Int J Radiat Oncol Biol Phys* 2000; 47: 1121-1135

[63] Ten Haken RK, Balter JM, Marsh LH, et al. Potential benefits of eliminating planning target volume expansions for patient breathing in the treatment of liver tumors. *Int J Radiat Oncol Biol Phys* 1997; 38: 613-617

[64] McKenzie AL. How should breathing motion be combined with other errors when drawing margins around the clinical target volumes? *Br J Radiol* 2000b; 73: 973-977

[65] Engelsman M, Remeijer P, van Herk M, et al. Field size reduction enables iso-NTCP escalation of tumor control probability for irradiation of lung tumors. *Int J Radiat Oncol Biol Phys* 2001; 51: 290-1298

[66] van Herk M, Witte M, van der Geer J, et al. Biological and physical fractionation effects of random geometrical errors. *Int J Radiat Oncol Biol Phys* 2003b; 57: 1460-1471

[67] ICRU (International Commission on Radiation Units and Measurements). Prescribing, recording and reporting electron beam therapy ICRU Report 72 (Oxford University Press, 2004)

[68] Thomas SJ. Margins between clinical target volume and planning target volume for electron beam therapy. *Br J Radiol* 2006; 79: 244-247

[69] Bortfeld T, Jiang SB, and Rietzel E. Effects of Motion on the Total Dose Distribution. *Sem Radiat Oncol* 2004; 14: 41-51

[70] Beckham WA, Keall PJ, and Siebers JV. A fluence-convolution method to calculate radiation therapy dose distributions that incorporate random set-up error. *Phys Med Biol* 2002; 7: 3465-3473

[71] Hornick DC, Litzenberg DW, Lam KL, et al. A tilt and roll device for automated correction of rotational set-up errors. *Med Phys* 1998; 25: 1739-1740

[72] Bel A, van Herk M, Bartelink H, et al. A verification procedure to improve patient set-up accuracy using portal images. *Radiother Oncol* 1993; 29: 253-260

[73] Yan D, Lockman D, Brabbins D, et al. An offline strategy for constructing a patient-specific planning target volume in adaptive treatment process for prostate cancer. *Int J Radiat Oncol Biol Phys* 2000; 48: 289-302

[74] Amer AM, Mackay RI, Roberts SA, et al. The required number of treatment imaging days for an effective offline correction of systematic errors in conformal radiotherapy of prostate cancer—A radiobiological analysis. *Radiother Oncol* 2001; 61: 143-150

[75] Bortfeld T, van Herk M, and Jiang SB. When should systematic patient positioning errors in radiotherapy be corrected? *Phys Med Biol* 2002; 47: N297-N302

[76] Lof J, Lind BK, and Brahme A. An adaptive control algorithm for optimization of intensity modulated radiotherapy considering uncertainties in beam profiles, patient set-up, and internal organ motion. *Phys Med Biol* 1998; 43: 1605-1628

[77] Suzuki O, Shiomi H, Nakamura S, et al. Novel correction methods as alternatives for the six-dimensional correction in CyberKnife treatment. *Radiat Med* 2007; 25: 31-37

[78] Nishioka T, Nishioka S, Kawahara M, et al. Synchronous monitoring of external/internal respiratory motion; validity of respiration-gated radiotherapy for liver tumors. *Jpn J Radiol* 2009; 27: 285-289

[79] Mageras GS, Yorke E; Deep inspiration breath hold and respiratory gating strategies for reducing organ motion in radiation treatment. *Semin Radiat Oncol* 2004; 14: 65-75

[80] Engelsman M, Remeijer P, van Herk M, et al. The theoretical benefit of beam fringe compensation and field size reduction for iso-normal tissue complication probability dose escalation in radiotherapy of lung cancer. *Med Phys* 2003; 30: 1086-1095

[81] Goshtasby AA. 2-D and 3-D Image Registration for Medical, Remote Sensing, and Industrial Applications (Hoboken, NJ: John Wiley and Sons, Inc., 2005)

[82] Xing L, Siebers J, and Keall P. Computational challenges for image-guided radiation therapy; Framework and current research. *Semin Radiat Oncol* 2007; 17: 245-257

[83] Pham DL, Xu C, and Prince JL. "Current Methods in Medical Image Segmentation," in Annual Rrview of biomedical engineering Vol. 2. ed ML Yarmush, KR Diller, and M Toner, 315-337(Annual Reviews, 2003)

[84] Perez C and Brady LW. Principles and practice of radiation oncology. (Philadelphia, PA: JP Lippencott, 1992)

[85] Holloway AF. A localising device for a rotating cobalt therapy unit. *Br J Radiol* 1958; 31: 227

[86] Johns HE and Cunningham JR. A precision cobalt 60 unit for fixed field and rotation therapy. *Am J Roentgenol Radium Ther Nucl Med* 1959; 81: 4-12

[87] Haus AG, Pinsky SM, and Marks JE. A technique for imaging patient treatment area during a therapeutic radiation exposure. *Radiology* 1970; 97: 653-656

[88] Rabinowitz I, Broomberg J, Goitein M, et al. Accuracy of radiation field alignment in clinical practice. *Int J Radiat Oncol Biol Phys* 1985; 11: 1857-1867

[89] van Herk M and Meertens H. A matrix ionisation chamber imaging device for online patient set-up verification during radiotherapy. *Radiother Oncol* 1988; 11: 369-378

[90] Droege RT and Bjlrngard BE. Influence of metal screens on contrast in megavoltage X-ray imaging. *Med. Phys* 1979; 6: 487-492

[91] Meertens H. Digital processing of high-energy photon beam images. *Med Phys* 1985; 12: 111-113

[92] De Neve W, Van den HF, De Beukeleer M, et al. Routine clinical online portal imaging followed by immediate field adjustment using a tele-controlled patient couch. *Radiother Oncol* 1992; 24: 45-54

[93] Ezz A, Munro P, Porter AT, et al. Daily monitoring and correction of radiation field placement using a video-based portal imaging system; A pilot study. *Int J Radiat Oncol Biol Phys* 1992; 22: 159-165

[94] Vetterli D, Thalmann S, Behrensmeier F, et al. Daily organ tracking in intensity-modulated radiotherapy of prostate cancer using an electronic portal imaging device with a dose saving acquisition mode. *Radiother Oncol* 2006; 79: 101-110

[95] Pasma KL, Heijmen BJ, Kroonwijk M, et al. Portal dose image (PDI) prediction for dosimetric treatment verification in radiotherapy. An algorithm for open beams. *Med Phys* 1998; 25: 830-840

[96] van Elmpt W, Nijsten S, Mijnheer B, et al. The next step in patient-specific QA: 3D dose verification of conformal and intensity-modulated RT based on EPID dosimetry and Monte Carlo dose calculations. . *Int J Radiat Oncol Biol Phys* 2008; 86: 86-92

[97] Swindell W, Simpson RG, Oleson JR, Chen CT, and Grubbs EA. Computed tomography with a linear accelerator with radiotherapy applications. *Med Phys* 1983; 10: 416-420

[98] Mosleh-Shirazi MA, Evans PM, Swindell W, Webb S, and Partridge M. A cone-beam megavoltage CT scanner for treatment verification in conformal radiotherapy. *Radiother Oncol* 1988; 48: 319-328

[99] Balter JM and Kessler ML. Imaging and alignment for image-guided radiation therapy. *J Clin Oncol* 2007; 25: 931-937

[100] Balter J, Wright J, Newell J, et al. Accuracy of a wireless localization system for radiotherapy. *Int J Radiat Oncol Biol Phys* 2005; 61: 933-937

[101] Groh BA, Siewerdsen JH, Drake DG, Wong JW, and Jaffray DA. A performance comparison of flat-panel imager-based MV and kV cone-beam CT. *Med Phys* 2002; 29: 967-975

[102] Smitsmans M, Wolthaus J, Artignan X, et al. Automatic localization of the prostate for on-line or off-line image-guided radiotherapy. *Int J Radiat Oncol Biol Phys* 2004; 60: 623-635

[103] Shirato H, Shimizu S, Kitamura K, et al. Four-dimensional treatment planning and fluoroscopic real-time tumor tracking radiotherapy for moving tumor. *Int J Radiat Oncol Biol Phys* 2000a; 48: 435-442

[104] Shirato H, Shimizu S, Kunieda T, et al. Physical aspects of a real-time tumor-tracking system for gated radiotherapy. *Int J Radiat Oncol Biol Phys* 2000b; 48: 1187-1195

[105] Uematsu M, Fukui T, Shioda A, et al. A dual computed tomography linear accelerator unit for stereotactic radiation therapy; A new approach without cranially fixated stereotactic frames. *Int J Radiat Oncol Biol Phys* 1996; 35: 587-592

[106] Uematsu M, Shioda A, Tahara K, et al. Daily positioning accuracy of frameless stereotactic radiation therapy with a fusion of computed tomography and linear accelerator (focal) unit; Evaluation of z-axis with a z-marker. *Radiother Oncol* 1999; 50: 337-339

[107] Ma C and Paskalev K. In-room CT techniques for image-guided radiation therapy. *Med Dosim* 2006; 31: 30-39

[108] Dempsey JF, Benoit D, Fitzsimmons JR, et al. A device for realtime 3D image-guided IMRT. *Int J Radiat Oncol Biol Phys* 2005; 63: S202

[109] Raaymakers B, Overweg J, Van der Heide U, et al. Design of the MRI accelerator. *Rad Oncol* 2005; 76: S109

[110] Fallone BG, Murray B, Rathee S, et al. First MR images obtained during megavoltage photon irradiation from a prototype integrated linac-MR system. *Med Phys* 2009; 36: 2084-2088

[111] Troccaz J, Menguy Y, Bolla M, et al. Conformal external radiotherapy of prostatic carcinoma: requirements and experimental results. *Radiother Oncol* 1993; 29: 176-183

[112] Carson PL and Fenster A. Anniversary Paper; Evolution of ultrasound physics and the role of medical physicists and the AAPM and its journal in that evolution. *Med Phys* 2009; 36: 411-428

[113] Holupka EJ, Kaplan ID, Burdette EC, and Svensson GK. Ultrasound image fusion for external beam radiotherapy for prostate cancer. *Int J Radiat Oncol Biol Phys* 1996; 35: 975-984

[114] Tong S, Cardinal HN, Downey DB, and Fenster A. Analysis of linear, area and volume distortion in 3D ultrasound imaging. *Ultrasound Med Biol* 1998; 24: 355-373

[115] Fichtinger G, Burdette EC, Tanacs A, et al. Robotically assisted prostate brachytherapy with transrectal ultrasound guidance — phantom experiments. *Brachytherapy* 2006; 5: 14-26

[116] Ding M, Cardinal HN, and Fenster A. Automatic needle segmentation in three-dimensional ultrasound images using two orthogonal two-dimensional image projections. *Med Phys* 2003; 30: 222-234

[117] Fuss M, Salter BJ, Cavanaugh SX, et al. Daily ultrasound-based image-guided targeting for radiotherapy of upper abdominal malignancies. *Int J Radiat Oncol Biol Phys* 2004a; 59: 1245-1256

[118] Fuss M, Salter BJ, Herman TS, et al. External beam radiation therapy for hepatocellular carcinoma; Potential of intensity-modulated and image-guided radiation therapy. *Gastroenterology* 2004b; 127: S206-S217

[119] Lattanzi J, McNeeley S, Hanlon A, et al. Ultrasound-based stereotactic guidance of precision conformal external beam radiation therapy in clinically localized prostate cancer. *Urology* 2000; 55: 73-78

[120] Cury FL, Shenouda G, Souhami L, et al. Ultrasound-based image guided radiotherapy for prostate cancer; comparison of cross-modality and intramodality methods for daily localization during external beam radiotherapy. *Int J Radiat Oncol Biol Phys* 2006; 66: 1562-1567

[121] Rasch C, Barillot I, Remeijer P, Touw A, van Herk M, and Lebesque JV. Definition of the prostate in CT and MRI; a multi-observer study. *Int J Radiat Oncol Biol Phys* 1999; 43: 57-66

[122] Smith W, Lewis C, Bauman G, et al. 3DUS, MRI and CT prostate volume definition; 3D evaluation of intra- and inter-modality and observer variability [Abstract]. *Med Phys* 2005; 32: 2083

[123] Kälkner KM, Kubicek G, Nilsson J, Lundell M, Levitt S, and Nilsson S. Prostate volume determination; differential volume measurements comparing CT and TRUS. *Radiother Oncol* 2006; 81: 179-183

[124] Peeters ST, Heemsbergen WD, Koper PC, et al. Dose–response in radiotherapy for localized prostate cancer; results of the Dutch multicenter randomized phase III trial comparing 68 Gy of radiotherapy with 78 Gy. *J Clin Oncol* 2006; 24: 1990-1996

[125] Pollack A, Hanlon AL, Horwitz EM, et al. Dosimetry and preliminary acute toxicity in the first 100 men treated for prostate cancer on a randomized hypofractionation dose escalation trial. *Int J Radiat Oncol Biol Phys* 2006; 64: 518-526

[126] Ghilezan M, Yan D, Liang J, et al. Online image-guided intensity-modulated radiotherapy for prostate cancer; How much improvement can we expect? A theoretical assessment of clinical benefits and potential dose escalation by improving precision and accuracy of radiation delivery. *Int J Radiat Oncol Biol Phys* 2004; 60: 1602-1610

[127] Langen KM, Pouliot J, Anezinos C, et al. Evaluation of ultrasound-based prostate localization for image-guided radiotherapy. *Int J Radiat Oncol Biol Phys* 2003; 57: 635-644

[128] Van den Heuvel F, Powell T, Seppi E, et al. Independent verification of ultrasound based image-guided radiation treatment, using electronic portal imaging and implanted gold markers. *Med Phys* 2003; 30: 2878-2887

[129] Scarbrough TJ, Golden NM, Ting JY, et al. Comparison of ultrasound and implated seed marker prostate localization methods; implications for image guided radiotherapy. *Int J Radiat Oncol Biol Phys* 2006; 65: 378-387

[130] McNair HA, Mangar SA, Coffey J, et al. A comparison of CT- and ultrasound-based imaging to localize the prostate for external beam radiotherapy. *Int J Radiat Oncol Biol Phys* 2006; 65: 678-687

[131] Kudchadker RJ, Lee AK, Yu ZH, et al. Effectiveness of using fewer implanted fiducial markers for prostate target alignment. *Int J Radiat Oncol Biol Phys* 2009; 74: 1283-1289

[132] Kupelian PA, Willoughby TR, Meeks SL, et al. Intraprostatic fiducial for localization of the prostate gland; monitoring intermarker distances during radiation therapy to test for marker stability. *Int J Radiat Oncol Biol Phys* 2005; 62: 1291-1296

[133] Artignan X, Smitsmans MH, Lebesque JV, et al. Online ultrasound image guidance for radiotherapy of prostate cancer; Impact of image acquisition on prostate displacement. *Int J Radiat Oncol Biol Phys* 2004; 59: 595-601

[134] Dobler B, Mai S, Ross C, et al. Evaluation of possible prostate displacement induced by pressure applied during transabdominal ultrasound image acquisition. *Strahlenther Onkol* 2006; 182: 240-246

[135] Enke C, Ayyangar K, Saw CB, Zhen W, Thompson RB, and Raman NV. Inter-observer variation in prostate localization utilizing BAT [Abstract]. *Int J Radiat Oncol Biol Phys* 2002; 54: supplement

[136] Fuss M, Cavanaugh SX, Fuss C, et al. Daily stereotactic ultrasound prostate targeting; Inter-user variability. *Technol Cancer Res Treat* 2003; 2: 161-170

[137] Berrang T, Truong PT, Pepescu C, et al. 3D ultrasound can contribute to planning CT to define the target for partial breast radiotherapy. *Int J Radiat Oncol Biol Phys* 2009; 73: 375-383

[138] van Herk M. Different styles of image-guided radiotherapy. *Semin Radiat Oncol* 2007; 17: 258-267

CHAPTER 3
Medical ultrasonography

The basic physics behind ultrasound and ultrasound devices is presented in this chapter. First, mechanical wave generation, and the materials used in medical ultrasound equipment are presented. Second, wave propagation and image formation are described. The chapter ends with an introduction to the ultrasound equipment used in this thesis.

3.1 The piezoelectric effect

The discovery of the piezoelectric effect by the brothers Pierre and Jacques Curie in France in 1880 marked a breakthrough development in harnessing ultrasound for many applications. The Curies, however, did not predict the converse piezoelectric effect, which was mathematically deduced from fundamental thermodynamic principles by Gabriel Lippmann in 1881 [1]. The first practical application for piezoelectric devices was sonar (sound navigation and ranging), first developed during World War I. After the end of World War II, advances in ultrasound technology brought improved possibilities for medical applications. Two researchers are noted in the history of ultrasound and medical imaging. Karl Theodore Dussik from Austria published the first paper on medical ultrasonics in 1942 based on his research on transmission ultrasound investigations of the brain [2]. In 1958 Professor Ian Donald from Scotland, who developed practical technology, including tissue differentiation in live volunteer patients, wrote one of the most important papers for the field of diagnostic medical imaging [3]. Further technical developments by Donald led to obstetric applications, thereby solidifying the role of ultrasound in medicine by the late 1970s.

The piezoelectric effect is exhibited in dielectric solids that produce a voltage across their surfaces when a mechanical stress (pressure) is applied. The mechanical stress displaces

the dipoles resulting in a temporary excess of surface charge. Conversely, a mechanical strain (deformation) results when an electric field is applied. For linear elastic materials, stress and strain are linearly related via Young's modulus as described in Hooke's Law. The amount of dipole displacement, D, is also linearly related to the applied stress, σ, via the piezoelectric charge constant, d, which measures the material specific polarization generated per unit of mechanical stress.

$$D = d\sigma \tag{3.1}$$

In general, greater stress applied will induce a greater charge displacement and produce a greater voltage between the surfaces [4].

Exposed to an alternating electric field a piezoelectric material will change dimension cyclically at the frequency of the field. The frequency at which the element vibrates most readily, and at which electrical energy is most efficiently converted into mechanical energy, is the resonance frequency. The electromechanical coupling coefficient, k_c, is a measure of the energy conversion, and is the ratio of electrical/mechanical energy out to mechanical/electrical energy in. The resonance frequency is determined by the composition, shape, and volume of the element. Generally, a thicker element has a lower resonance frequency than a thinner element of the same shape. The term ultrasound applies to acoustic energy with a (resonance) frequency above human hearing, ~20 kHz. Medical diagnostics operates within the range of 2-20 MHz [5].

3.2 Piezoelectric ceramics

Preceding the advent of piezoelectric ceramics in the early 1950's, piezoelectric crystals made from quartz were primarily used. Natural piezoelectric crystals have a large number of dipole moments but no net moment until a stress is applied. Many crystals exhibit a small piezoelectric effect at low temperatures but are unsuitable for ultrasound imaging because these properties do not exist at room temperature. In analogy to ferromagnetic materials, the Curie temperature is also used in piezoelectric materials to describe the temperature above which the piezoelectric properties disappear due to thermal oscillations that compete against the dipole tendency to align. Man made ceramic materials such as lead zirconate titanate (PZT) have been developed with improved properties, and can be tailored to specific requirements. For example, k_c for quartz is 0.11 whereas k_c for PZT is 0.7 [6].

Ceramics capable of exhibiting piezoelectricity are also ferroelectric materials that exhibit hysteresis. Groups of dipoles with parallel orientation are called Weiss domains, which are randomly oriented in ferroelectric and ferromagnetic materials. When the material is heated and a strong electric field is applied (›2000 V/mm), the Weiss domains align and roughly stay in alignment upon cooling, leaving a remnant polarization. This hysteresis treatment is known as poling. The electric field causes expansion or contraction parallel and perpendicular to the field (Fig. 3.1). The material can be depoled by reversing the poling voltage, increasing the temperature beyond the material's Curie point, or by inducing a large mechanical stress.

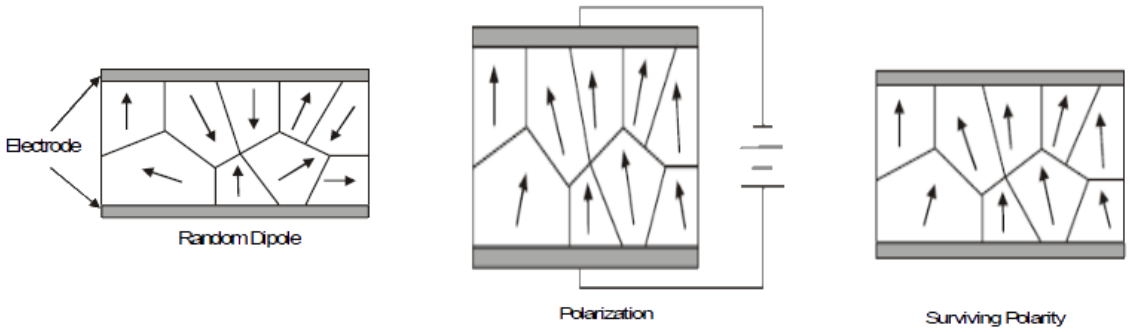

FIG. 3.1 Poling of a ferroelectric material to induce remnant polarization.

A traditional PZT ceramic is a mass of perovskite crystals arranged in a cubic lattice (Fig. 3.2) with a symmetric arrangement of positive and negative charges. After poling the unit cell exhibits asymmetry and a dipole moment. The remnant polarization permanently elongates the unit cell.

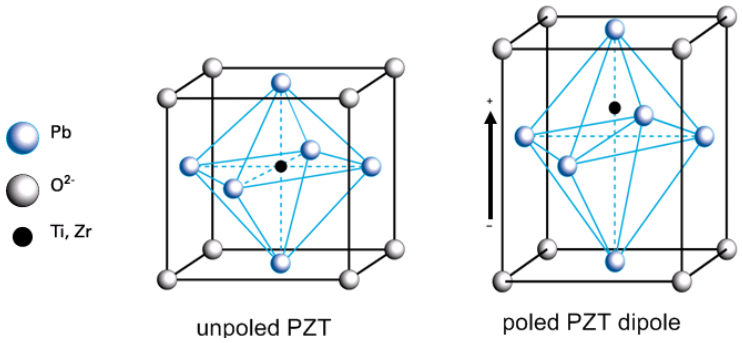

FIG. 3.2 The unit cell of PZT before and after poling.

Piezoelectric ceramics are the most widely used materials for actuator and sensor applications. Examples include scanning tunnelling microscopes, airbag sensors, microphones, inkjet printers, electric drum pads, and telescope mirrors. Ceramics manufactured from PZT exhibit great sensitivity and high operating temperatures [6].

3.3 Wave propagation

An oscillating piezoelectric element, compressing and expanding, generates a mechanical wave that propagates in surrounding media, whose particles move parallel to the direction of the wave. Such a longitudinal pressure wave has high and low density regions. The speed of the wave is determined by the elastic properties of the transporting medium. The speed of the wave, *c*, is not to be confused with the speed of the vibrating molecules in the medium, *v*. The mass and spacing of the molecules, and the attracting force between them, have an effect on the speed of the wave as it passes through. Ultrasound waves travel faster with increasing medium stiffness, and slower in compressible materials. The speed of ultrasound in different media relevant to radiation therapy is presented in Table 3.1.

Table 3.1 Characteristics of media that are relevant to diagnostic ultrasound [7].

Medium	Density (kg/m^3)	Impedance ($kg/m^2/s$)	Speed (m/s)
Air at STP	1.29	394	331
Lung	400	0.26×10^6	650
Fat	920	1.33×10^6	1446
Water	1000	1.48×10^6	1480
Blood	1050	1.66×10^6	1566
Muscle	1070	$1.65\text{-}1.74 \times 10^6$	1542-1626
Bone	1380-1810	$3.75\text{-}7.38 \times 10^6$	2070-5350

The characteristic acoustic impedance of a medium, Z_0, is a frequency dependent parameter. For a plane wave,

$$Z_0 = \rho c \tag{3.2}$$

$$Z_0 = \rho \lambda f \tag{3.3}$$

where ρ is the mass density of the medium, λ is the wavelength, and f is the frequency.

There are four types of interaction between an ultrasound wave and the propagating medium: reflection, refraction, scattering, and absorption. Differences in impedance between media cause the wave to be reflected and refracted at interfaces. The direction of the reflected ray (the echo) is governed by Snell's law of reflection, which states that the angle of incidence equals the angle of reflection (Fig. 3.3).

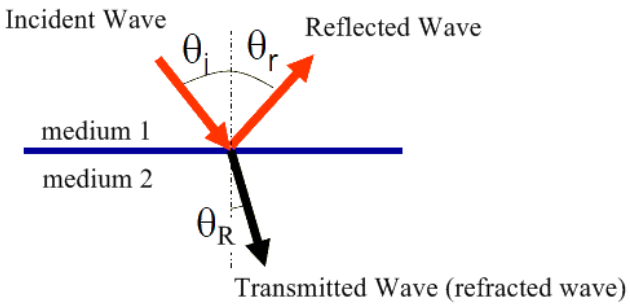

FIG. 3.3 Diagram of an incident wave on a boundary between media with different impedances. The definition of the angles of incidence (i), reflection (r), and refraction (R) are defined.

The reflection coefficient, R_A, gives the ratio of the amplitude of the reflected wave to the incident wave. If R_A = 1, then the wave is completely reflected. Similarly, the transmission coefficient is given by T_A = 1 - R_A. The reflection coefficient is on the order of 0.01 (1%) for soft tissue interfaces, 0.41 for skull/brain interfaces, and 0.99 for muscle/air interfaces [7].

$$R_A = \left| \frac{Z_1 / \cos\theta_i - Z_2 / \cos\theta_t}{Z_1 / \cos\theta_i + Z_2 / \cos\theta_t} \right| \tag{3.4}$$

Specular reflectors are large interfaces in the body between two different tissues, such as the heart and the lung. Specular reflectors are large compared to the wavelength of the wave and act as smooth surfaces so that the law of reflection applies. The greater the difference in impedance of the two materials (Z_2 - Z_1), the greater the bias towards reflection and the larger the amplitude of the reflected wave. Nonspecular reflectors are small compared to the

wavelength and result in diffuse reflection where the wave is reflected in many directions, thus producing a low intensity reflection.

The basic idea behind ultrasound imaging is to send waves into the body, and to receive reflected waves (the echo). The return time of the waves provides the depth of the reflecting interface. For a single piezoelectric element to register a reflected echo, the wave must be reflected back along the same path. Only when the incident wave is perpendicular to the interface will the reflected wave be received by the element (i.e. only when the angles of incidence and reflection are zero).

Ultrasound waves also interact through scattering and absorption, which attenuate the wave thereby reducing the signal strength as the wave travels through the patient. Scattering processes reflect the wave away from the transmitting element. Hyper and hypoechoic are terms that describe regions of higher and lower scatter amplitude, respectively. Most organs have characteristic structure that gives rise to a defined scatter signature. The signature can be used in tissue typing [8].

The attenuation coefficient, μ, is a measure of the relative intensity loss per centimeter of travel in a given medium for a given wave frequency. It varies approximately with f^2 for water and $f^{1.2}$ for soft tissue [7]. There is a rule of thumb that $\mu \sim 0.5$ dB/cm/MHz in soft tissue. Attenuation is exponential so there is a depth beyond which we cannot detect returned echoes. This depth depends on the frequency of the wave as lower frequency waves penetrate deeper. Lower frequency waves cause less molecular vibration and friction so that less energy is lost to heat and is absorbed. This effect also depends on the amplitude of the wave, but in the medical diagnostic range it is small as normal tissue perfusion dissipates heat quickly. Nonetheless, ultrasonic heating has been used in cancer therapy where tumours heated to > 43 °C can be treated effectively with a much lower dose of x-rays than an unheated tumour. High intensity focused ultrasound (HIFU) is also used to heat and destroy malignant tissue [9]. The choice of wave frequency is a trade-off between spatial resolution of the image and imaging depth: lower frequencies produce less resolution but image deeper into the body. For this reason abdomen, foetal, OB/GYN, and pelvic applications use frequencies around 3.5 MHz, whereas musculoskeletal and superficial applications use frequencies around 10 MHz [9]. Soft tissue is composed of a matrix of solid constituents that introduce inhomogeneities that are responsible

for both scattering and absorption [10]. At 3.5 MHz, nonspecular reflectors are on the order of 0.4 mm.

3.3.1 Nonlinear propagation

When mechanical waves propagate through a material, they act as a force that creates localized pressure changes. The speed of sound in a compressible material increases with pressure because the molecules transmitting the energy are closer. As a result, the wave travels faster during the high pressure phase of the oscillation than during the lower pressure phase. Consequently higher pressure sections of the wave shift further forward than lower pressure sections, resulting in a change in the shape of the wave. This affects the wave's frequency structure by introducing other frequency components. The pressure changes within a medium cause the wave energy to transfer to higher frequencies. Since attenuation generally increases with frequency, a counter effect exists that changes the nature of the nonlinear effect over distance. Because of their relatively high amplitude to wavelength ratio, ultrasound waves commonly display nonlinear propagation behaviour. This behaviour is taken advantage of in harmonic imaging with and without a contrast agent [11].

3.4 The pulse-echo principle

Two methods are commonly used to generate ultrasound waves. Continuous wave propagation requires separate transmitting and receiving elements because a single element cannot generate and detect a pressure wave at the same time. Continuous waves have applications in Doppler ultrasound, which employs the Doppler Effect to assess whether structures (usually blood) are moving at a given speed. Pulsed waves are produced by shocking a single element into oscillation with a quick change in voltage across its surfaces. The oscillation is damped quickly to create a pulse and shorten the spatial pulse length (the number of wave cycles in the pulse multiplied by their wavelength). The length of the pulse is determined by the ability of the damping or backing material behind the element to absorb the vibrations. A material backed ceramic will dampen the vibration faster than an air backed ceramic however, it will introduce additional frequencies as it decreases the amplitude of the pulse. This causes the pulse to have a bandwidth with a central resonance frequency. The shorter the pulse, the wider its frequency spectrum. The Q-factor is the ratio of the central frequency to the bandwidth, and describes how an element and damping block system will respond to a short voltage pulse. Imaging requires short pulses for better resolution and the ability to respond to echoes over a

wide range of frequencies due to the presence of harmonics. A low Q-factor of 2-3 is typically used [5]. Doppler ultrasound applications require high Q-factors to produce narrow bandwidth pulses in order to detect small frequency changes of moving blood (~2 kHz).

A typical pulse excitation would be a 1 μs voltage shock at 1 MHz, implying that the majority of the duty cycle is spent listening for returning echoes. The time delay between transmission and detection, as well as the amplitude, of the echo is recorded. The time delay, Δt, indicates the depth of reflection, and the amplitude is an indication of attenuation and reflection. The distance to the reflector, Δd, is calculated as,

$$\Delta d = 1/2\, c \Delta t \tag{3.5}$$

where all diagnostic ultrasound systems assume c = 1540 m/s to be constant within the human body, equivalent to the average speed in soft tissue. A constant is assumed based on the relative small variation among different soft tissues (±6%) [7]. For greater time delays the signal will be increasingly attenuated as it travels through more tissue to and from the element. Time-dependent attenuation causes severe signal loss if not compensated. All ultrasound systems are equipped with circuitry that performs time gain compensation; a time-varying amplification of the signal dependent on the time delay. In practice, most systems have additional (frequency dependent) potentiometers, which allow the gain to be determined interactively by the operator. This permits the user to manually adapt the system to special circumstances requiring either more or less gain so that subtle features can be seen in the images [12].

Ultrasound transducers house three main components for echo transmission and detection: the piezoelectric ceramic; the damping or backing material; and the matching layer. These components are shown in the schematic of Fig. 3.4. The ideal thickness of the ceramic element is half the wavelength of the resonant frequency that the element is to be vibrated at. This ensures that any wave reflected at the opposite end of the element will enhance the wave in the next cycle. Behind the element is the damping block. An air backed ceramic will transmit ultrasound to the casing, which is subsequently reflected from the casing back to the crystal to reinforce the wave propagated in the forward direction. A material backed ceramic suppresses ultrasound reverberation within the transducer, and often has a sloped rear surface to prevent

direct reflection. The matching layer provides an efficient transfer of energy between the element and the human body by impedance matching. The ideal impedance is given by,

$$Z_{match} = \sqrt{Z_{element} Z_{medium}} \tag{3.6}$$

The matching layer has a thickness of λ/4, which ensures that waves reflected within the matching layer stay in phase when they exit the layer [12,13]. These three components are housed in a plastic casing made of materials to enable maximum transmission into, and from, the body. In addition, a water-based coupling gel is used to eliminate any air pockets between the transducer and the patient's skin.

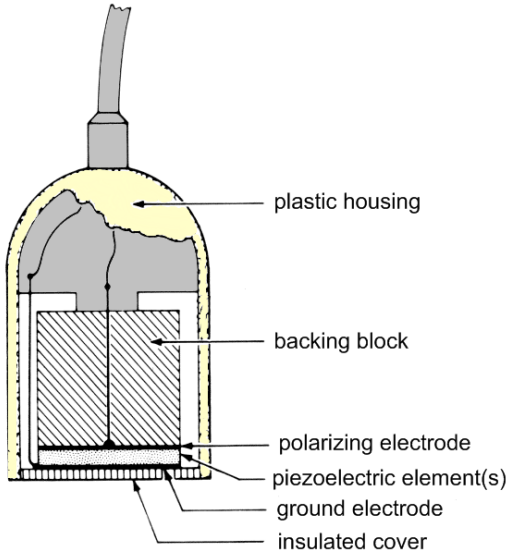

FIG. 3.4 A schematic of the essential components of an ultrasound transducer.

3.5 Multi-element beam propagation

A diagnostic ultrasound transducer is typically composed of 128-512 discrete elements. When consecutive elements are fired the waves interact with one another and the resultant simple pressure field can be described with Huygens' Principle. That is, an advancing wave front can be considered as the summation of many point sources. The classical Fresnel summation model describes two main features of the advancing wave front. Within the Fresnel zone (near

field) pronounced interference occurs as wave fronts from different elements arrive at points in front of the transducer at different times, but most of the energy is confined to a beam width no greater than the active portion of the element array (the effective transducer width). In the Fraunhofer zone (far field) the beam pattern is more uniform as the wave fronts are assumed to arrive at the same time, but some energy escapes along the periphery to produce a gradual divergence. This causes the beam pattern to change as one moves from the near field to the far field. Figure 3.5 shows interference patterns from a different number of active elements. At 3.5 MHz the near field of a 5 cm diameter transducer will extend to 142 cm. Generally such a beam will only penetrate ~40 cm before it is (completely) attenuated to 10^{-7} of the original intensity. Even for smaller transducers at higher frequencies, diagnostic ultrasound forms images from echoes received from the near field.

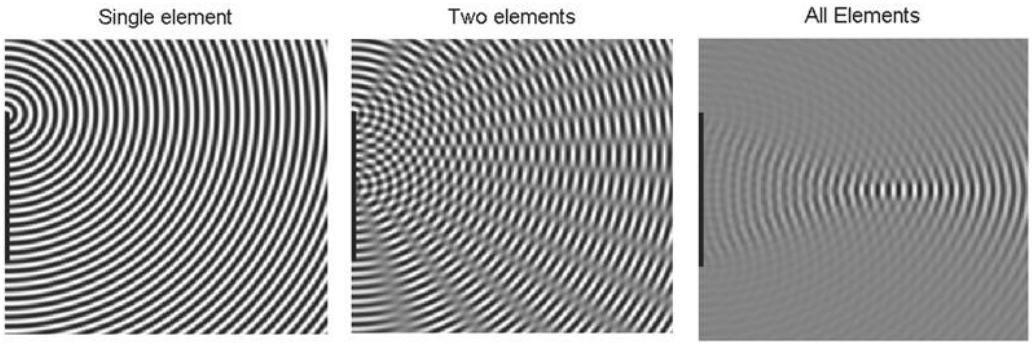

FIG. 3.5 Interference patterns produced from a different number of active elements.

As with all imaging modalities, image resolution is directly proportional to the frequency of the beam. The higher the frequency, the shorter the wavelength, and therefore the higher the resolution. For any given frequency, the minimum separation between two interfaces that can be resolved as separate echoes in the depth direction, known as the axial direction, must be greater than half the spatial pulse length. Perpendicular to the axial direction, the lateral resolution refers to the ability to discern two adjacent objects. In order to separate two objects that are closely spaced, a scan line (see section 3.6) must be more narrow than the space between them. As the diameter of the beam varies with distance from the transducer, so does the lateral resolution [4].

3.6 Array transducers

Most transducers today are multi-element, as the resolution of a single element depends on the geometry and cannot be changed. Multi-element transducers are constructed by slicing the piezoelectric ceramic into several small pieces. Each element has its own electrode and is isolated ultrasonically from adjacent elements. The most common configurations are linear and curvilinear transducers, as shown in Fig. 3.6.

FIG. 3.6 The curvilinear array (left) has a bandwidth between 1 and 4 MHz with abdomen, foetal, OB/GYN, and pelvic applications. The linear array (right) has a bandwidth between 5 and 14 MHz with cerebrovascular, musculoskeletal, peripheral vascular, and thyroid applications.

Linear transducers are typically used for real-time scanning of small rectangular sections of tissue such as for vascular and laparoscopic scanning. Such transducers are operated at higher frequencies and have a smaller transducer width. The elements in curvilinear transducers are arranged in a convex shape and have a larger trapezoidal field of view. They are used in the construction of probes for general abdominal and pelvic scanning.

A linear phased array transducer is operated by sequentially activating groups of ~15-20 adjacent elements so that a single scan line is created from a single activated group. Sequential scan lines are summed to compose an image. Acquisition of a single line takes ~260 μs, and a typical image has 120 lines for a total time of 31 ms. The images are reconstructed in near real-time resulting in a minimum temporal resolution of ~30 Hz as modern scanners can collect multiple scan lines simultaneously [12].

Beam forming is about controlling an interference pattern where the amplification occurs predominantly in one distinct direction. Phased array transducers use timing delays to sweep the

field of view, or electronically steer the beam in different directions, as shown in Fig. 3.7. Phased activation also allows for dynamic focusing at any selected depth in order to increase the lateral resolution in the near field however, decreasing the resolution in the far field due to a more rapid beam divergence. A focusing transducer will lead to all wave fronts arriving at the same depth at the same time, producing a beam that is more narrow at depth than the dimension of the transducer. This also results in a higher energy concentration available for reflection. This brings about the depth-of-field compromise: the stronger the focusing, the more narrow the beam width at the focus but the greater the far field divergence [12]. Phased arrays provide a large sector image through a small area of contact without the need to move the transducer, for example intercostal probes for cardiac scanning [5].

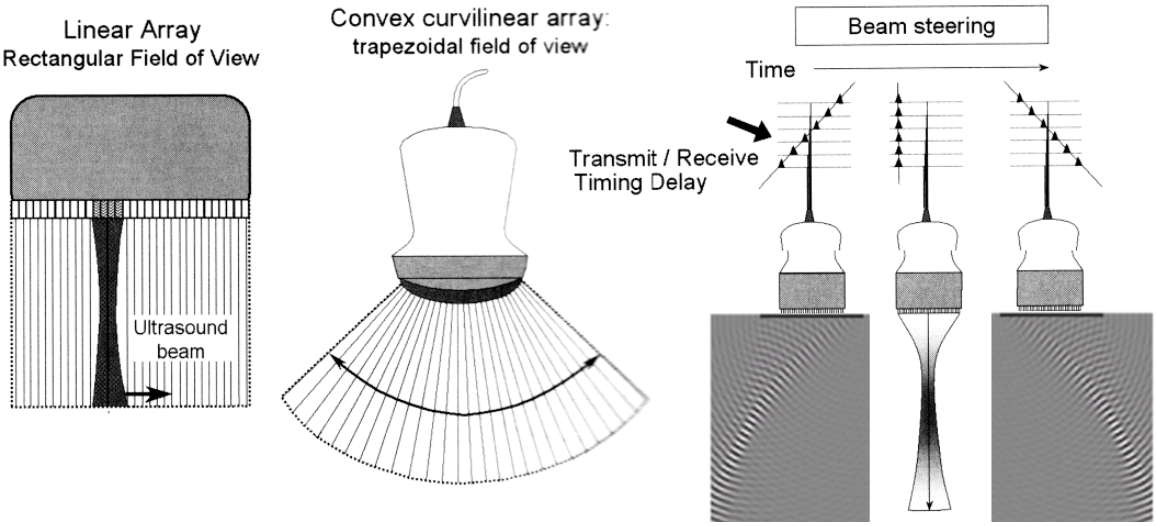

FIG 3.7 Beam propagation from linear, curvilinear, and phased array transducers.

3.7 Image formation

In ultrasound imaging there are three general modes of display. An A-mode (amplitude mode) scan displays a single scan line on a horizontal axis where the position of the pulse represents the depth of the returning echo and the amplitude of the pulse is directly proportional to the strength of the signal. A B-mode (brightness mode) scan, most commonly used today, displays amplitude as brightness. A set of B-mode image lines scanned through a cross section of the patient (also called a scan plane) generates a 2D grey scale image. Figure 3.8 is a 2D B-mode image of the prostate. Grey scale displays present both specular and nonspecular echoes for

diagnosis. An M-mode (motion mode) scan displays continuous A-mode data as dots instead of pulses. In this way, the dots are made to scroll across the screen creating bright curves indicating axial position changes of the reflectors with time. M-mode curves are popular in cardiology to show the motion patterns of various cardiac valves [12]. Doppler imaging, introduced in the 1980s, is a combination of all three modes where colour coded frequency shifts are used for the detection of blood velocity patterns.

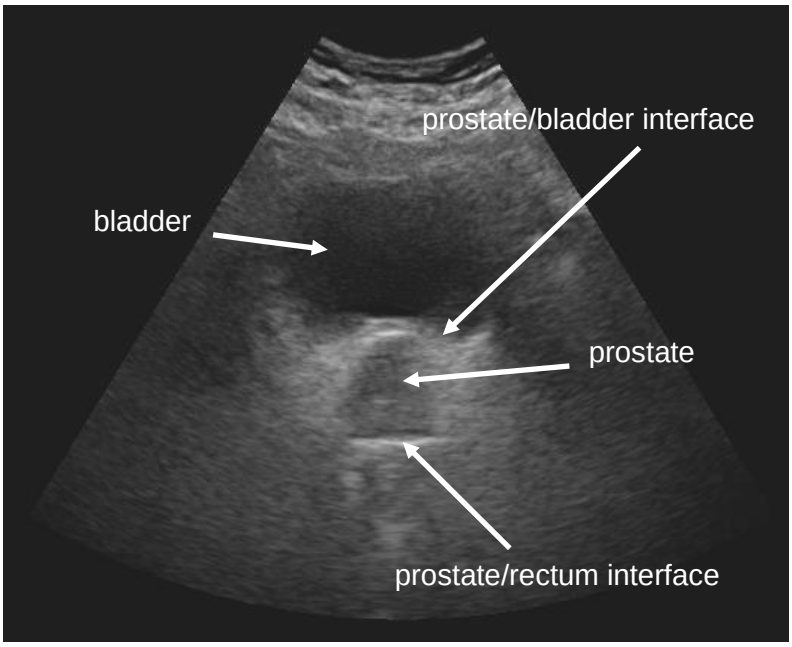

FIG. 3.8 Example of a B-mode ultrasound image of the prostate.

3.7.1 Artifacts

The ultrasound beam intensity changes in tissue occur at macroscopic and microscopic levels so that large tissue boundaries and small tissue structures are distinguished. The very high acoustic soft tissue contrast however, comes at a cost. Local absorption of acoustic energy is greater than ideal, making shadowing and enhancement artifacts quite prominent in images [17]. Acoustic shadowing occurs when sound waves encounter a substance that almost completely attenuates or reflects the beam. Because there is little energy to penetrate behind the highly attenuating substance, it appears as an echo free area. This artifact can be useful to find calcifications but can also be a hindrance, such as when rib shadows obscure deeper structures.

Enhancement occurs behind objects that do not absorb or reflect ultrasound. Distal objects receive an unattenuated beam and appear brighter in relation to surrounding tissue.

Phase cancellation can explain acoustical shadowing occurring at the edges of curved objects — a sharp, discrete shadow projecting down from the edge as displayed in Fig. 3.9. As a wave passes through inhomogeneous tissue, it is distorted because different portions of the wave travel at different speeds allowing some parts to move ahead of others. Upon contacting an element, an area may be at high pressure while another at low pressure causing small or fully cancelled signals [20].

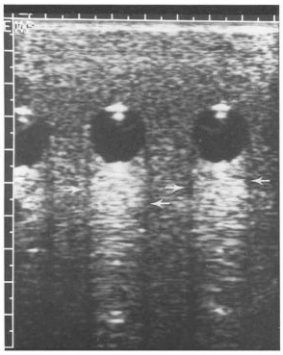

FIG 3.9 An ultrasound scan of a phantom with hypoechoic structures showing general speckle, strong reflection, distal enhancement, and phase cancellation artifacts.

The relative speed of propagation differences between tissues far exceeds the mass attenuation coefficient differences for ionizing radiation, leading to refraction and arrival time artifacts [18]. A refraction artifact occurs when ultrasound changes speed and direction as it passes between media with different impedances. This causes a misregistration artifact because the ultrasound system assumes the echo originated along a straight path so that the object is displayed in the wrong location. Scanning from different angles usually resolves this problem. Reverberation occurs when ultrasound echoes internally between interfaces of adjacent media. This can happen multiple times, resulting in additional echoes, which are interpreted as being deeper within the tissue than the original reflector. Reverberation artifacts are recognized by repeating horizontal linear echoes that are equally spaced with decreasing intensity.

Speckle and noise affect interpretation of the images and as a result, ultrasound imaging demands a high level of operator experience [19]. Speckle in ultrasound imaging (and all

coherent imaging systems) is caused by the interference of energy from randomly distributed scatterers too small to be resolved by the imaging system. Speckle degrades both the spatial and contrast resolution.

3.7.2 3D image formation in radiation therapy

2D B-mode sonography was the first ultrasound modality used in radiation therapy. The image plane in space was localized using a position sensing device attached to the transducer assembly. The first commercial ultrasound guided targeting device, B-mode Acquisition and Targeting (BAT (NOMOS, NAS, CA)) was launched in 1998. The transducer was mounted on a mechanical arm affixed to the isocentre in the treatment room via a docking device attached to the linac (Fig 3.10). Potentiometers at the arm joints were used to measure their rotation, allowing continuous determination of transducer position. Images in the axial and sagittal planes were acquired and localized with respect to the isocentre. The contours of the prostate, seminal vesicles, bladder, etc. from the planning CT could be imported and superimposed on the ultrasound images. If the CT structures did not coincide with the structures in the ultrasound images, the prostate was not positioned correctly for treatment. In this case the contours were manually aligned. The system recorded the translations performed and calculated the corresponding couch movement required for proper positioning. Similar ultrasound systems made use of a ceiling mounted infrared tracking device that monitored the position of infrared emitters attached to a freehand transducer.

In radiation therapy 3D ultrasound images are generally acquired by making use of a series of 2D images produced by 1D arrays. In 3D imaging, the relative position and angulations of the acquired 2D images must be known accurately, and the images must be acquired rapidly and/or gated to avoid artifacts due to respiratory, cardiac, and gastrointestinal motion. Two approaches have been used to reconstruct a 3D volume image from a digitized set of 2D images. In the 3D surface model approach the boundaries of the desired features are extracted from the 2D images and a 3D surface model of the anatomy is displayed. A disadvantage of this method is that identifying boundaries is time-consuming resulting in susceptibility to inaccuracy and variability. In the voxel-based volume approach the 2D images are built into a 3D voxel-based volume (3D grid) by placing each digitized 2D image into its correct location in the volume. An advantage to this method is that no information is lost during the 3D reconstruction, but the disadvantage is that large data files are generated [13].

The first commercial 3D ultrasound system for use in radiation therapy was the Sonarray system (Varian Medical Systems, Palo Alto, CA) [14,15]. It used a 2D transducer, an infrared tracking device, voxel-based volume reconstruction, and 3D visualization. Subsequently, a commercial 3D ultrasound system was developed (Restitu, Resonant Medical Inc., Montreal, Canada) to improve the accuracy of ultrasound image guided radiation therapy by removing discrepancies due solely to the imaging modality, and by reducing interobserver image acquisition and segmentation variations (Fig. 3.10) [16]. These include (and are shown in Fig. 3.11) 1) intramodality image registration (ultrasound to ultrasound) and position verification made possible by installing one ultrasound system directly in the CT simulation room and another in the treatment room, and 2) a semi-automatic 3D segmentation algorithm.

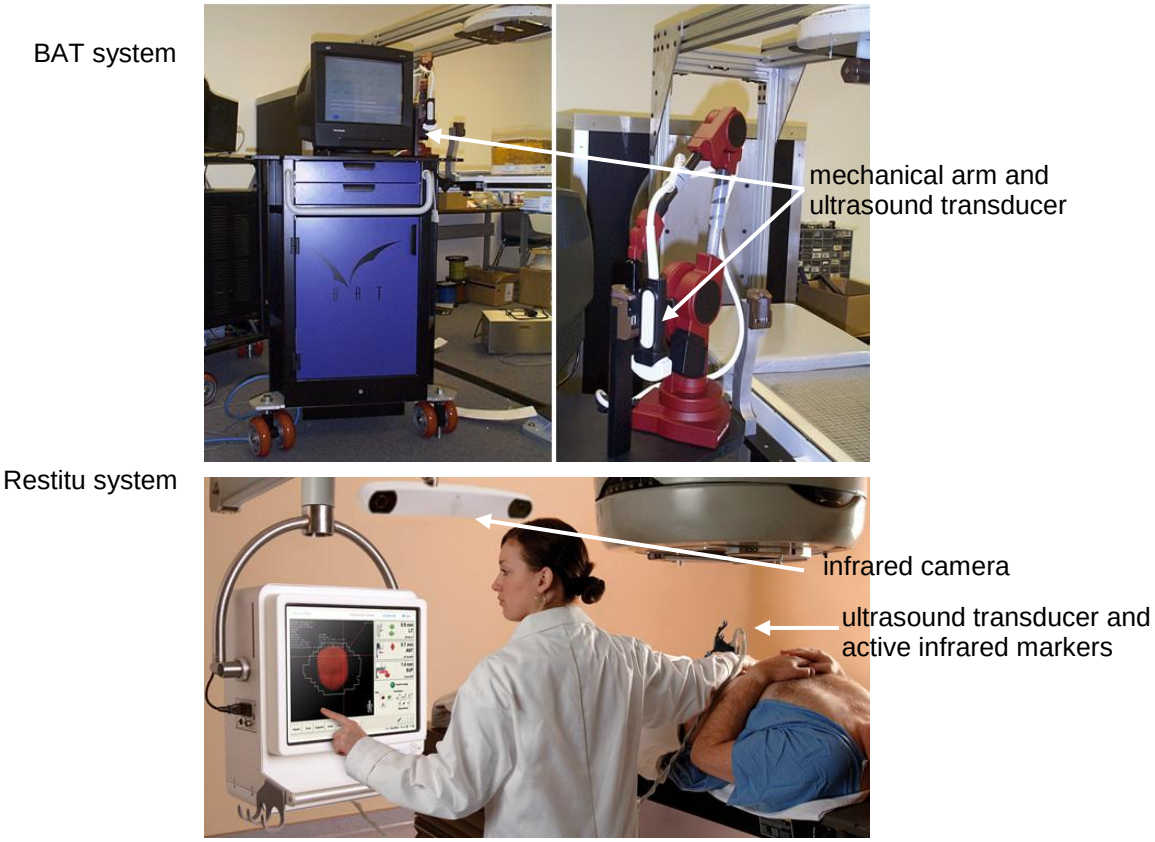

FIG. 3.10 The BAT system (top) showing the computer system, mechanical arm, and transducer. The Restitu system (bottom) showing the transducer with attached infrared markers and ceiling mounted camera.

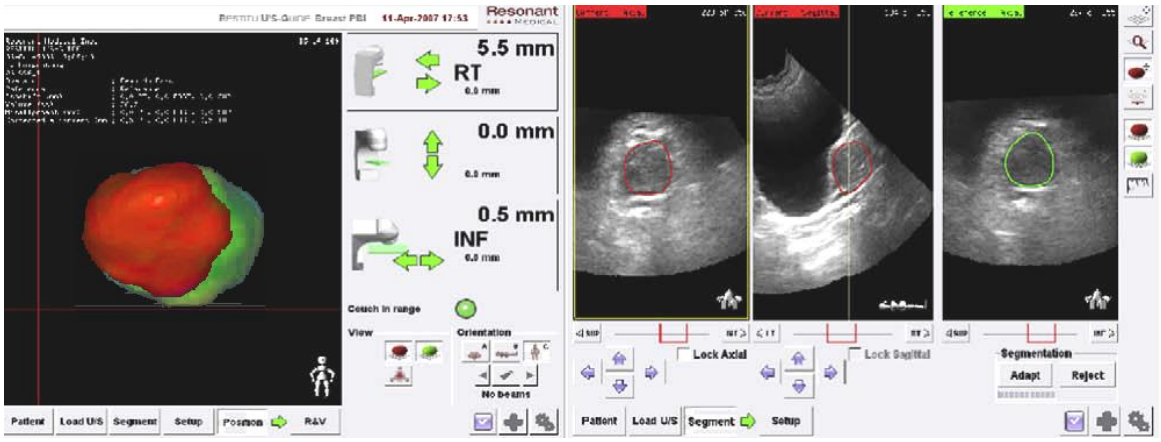

FIG. 3.11 Screen shot of Restitu graphical capabilities. The red shape is the semi-automatic segmented prostate acquired in the CT simulation room, and is compared to the green semi-automatic segmented prostate acquired in the treatment room. The right and left ultrasound images are axial slices and the central image is a sagittal slice, clearly showing the bladder (which shows up as hypoechogenic when full). 3D renditions are on the far left. The green arrows indicate the direction to move the couch in order to align the reference and treatment contours as calculated from their centre of mass.

3.8 Ultrasound equipment used in this thesis

The 3D ultrasound equipment used in this thesis was Restitu. It provides a new philosophy for ultrasound IGRT. The original treatment site application of Restitu was for transabdominal prostate imaging. For this purpose a curvilinear array with a central frequency of 3.5 MHz is used. This allows imaging to approximately 40 cm depth. However this does not preclude that the system cannot be used for imaging other sites as long as appropriate software/hardware changes are made. These changes primarily include:

- a transducer with a width and curvature to allow for good contact with the skin for the region of interest
- a central frequency to allow for optimal resolution at the depth of interest
- a tracking system that can track the position and orientation of the transducer over various volumes dependent on the treatment site

- differences in the semi-automatic segmentation algorithm in order to segment different organs
- possible changes in the configuration of the emitter array
- further changes in the software and reference comparison methods

Resitu is described in further detail in Chapter 5. It was used for imaging three cancer site applications in this work; head and neck (Chapter 5 and 6), prostate (Chapter 8), and breast (Chapter 9). For the breast application, the new version of the equipment was called Clarity.

3.9 References

[1] Lippman G. Principe de la conservation de l'électricité. *Annales de chimie et de physique* 1881; 24: 145

[2] White DN. Neurosonology pioneers. *Ultrasound Med Biol* 1988; 14: 541-561

[3] Donald I, MacVicar J, Brown TG. Investigation of abdominal masses by pulsed ultrasound. *Lancet* 1958; 1(7032): 1188-1195

[4] Zagzebski J. Essentials of Ultrasound Physics. (London: Mosby, 1996)

[5] Hill CR (ed). Physical principles of medical ultrasonics. (Chichester: Ellis Horwood, 1986)

[6] APC International Ltd. Piezoelectric ceramics: Principles and applications. (Pennsylvania: APC International, 2002)

[7] Goss SA, Frizzell LA, and Dunn F. Ultrasonic absorption and attenuation in mammalian tissues. *Ultras Med Bio* 1979; 5: 181-186

[8] Zhang P, Sunshine Osterman K, Liu T, et al. How does performance of ultrasound tissue typing affect design of prostate IMRT dose-painting protocols? *Int J Radiat Oncol Biol Phys* 2007; 67: 362-368

[9] Hughes S. Medical ultrasound imaging. *Journal of Physics Education* 2001; 36: 468-475

[10] Wells PNT. Ultrasonic Imaging of the Human Body. *Rep Prog Phys* 1999; 62: 671

[11] Burns PN. "Contrast Ultrasound Technology" in Contrast-enhanced ultrasound of liver diseases. ed L Solbiati, A Martegani, E Leen, JM Correas, PN Burns, 1- 19 (Milan: Springer, 2002)

[12] Hedrick W, Hykes D, Starchman D. Ultrasound physics and instrumentation (London: Mosby, 1992)

[13] Rankin RN, Fenster A, Downey DB, Munk PL, Levin MF, and Vellet AD. Three-dimensional sonographic reconstruction: techniques and diagnostic applications. *AJR* 1993; 161: 695-702

[14] Orton NP, Jaradat HA, and Tome WA. Clinical assessment of three-dimensional ultrasound prostate localization for external beam radiotherapy. *Med Phys* 2006; 33: 4710-4717

[15] Bouchet G, Meeks SL, and Goodchild G. Calibration of three-dimensional ultrasound images for image-guided radiation therapy. *Phys Med Biol* 2001; 46: 559-577

[16] Johnston H, Hilts M, Beckham W, and Berthelet W. 3D ultrasound for prostate localization in radiation therapy: A comparison with implanted fiducial markers. *Med Phys* 2008; 35: 2403-2413

[17] Drukker K, Giger ML, and Mendelson EB. Computerized analysis of shadowing on breast ultrasound for improved lesion detection. *Med Phys* 2003; 30: 1833-1842

[18] Moskalik A, Carson PL, Meyer CR, Fowlkes JB, Rubin JM, and Roubidoux MA. Registration of three-dimensional compound ultrasound scans of the breast for refraction and motion correction. *Ultrasound Med Biol* 1995; 21:769-778

[19] Carson PL and Fenster A. Anniversary Paper; Evolution of ultrasound physics and the role of medical physicists and the AAPM and its journal in that evolution. *Med Phys* 2009; 36: 411-428

[20] Rubin JM, Adler RS, Fowlkes JB, and Carson PL. Phase cancellation: A cause of acoustical shadowing at the edges of curved surfaces in B-mode ultrasound images. *Ultrasound Med Biol* 1991; 17: 85-95

CHAPTER 4
Monte Carlo simulations

Accurate calculation of accumulated absorbed dose in the presence of interfraction organ motion represents a necessary step toward adaptive radiation therapy. Margins, which have traditionally been used to account for patient-beam alignment errors, afford some protection against dose calculation errors near the periphery of the volume. Because image guided radiation therapy reduces setup errors and margins, the importance of accurate dose calculations increases. Monte Carlo techniques potentially lead to the highest degree of accuracy [1], and have been used extensively in medical physics applications. In this thesis all treatment unit modeling and patient dose calculations employed MC methods. MC methods were also compared with conventional algorithms. This section will briefly describe the fundamentals of these simulations.

4.1 Monte Carlo techniques in radiation therapy

Traditionally, patient dose calculations were based on interpolating measured dose distributions. The MC technique is the only dose calculation that considers all aspects of photon and electron transport within a heterogeneous phantom. This accuracy is accompanied by an increase in the amount of time required to produce a statistically meaningful dose distribution [1]. With intensive use of variance reduction techniques (see section 4.6.1) similar accuracy can now be achieved in time frames comparable to traditional calculation methods.

In radiation therapy MC methods rely on repeated pseudo-random sampling of probability distribution functions. These functions are capable of describing all physical processes that a particle undergoes, and therefore provide a detailed first-principles approach to solving the radiation transport problem. In external beam radiation therapy simulated particles

are tracked as they traverse the components of the treatment unit and subsequent absorbing medium. The accuracy provided by MC derives from scoring, or tallying, dosimetric quantities along the entire particle's track, providing for a complete history of events. Radiation transport essentially becomes a series of samples from interaction probability distribution functions, and a series of calculations at each step describing the particle's physical parameters resulting from the interactions.

Particle simulations are commonly divided into three regions similar to Udale et al's two step approach [2]. The first region is a model of the upper portion of the treatment unit's head, and consists of simulating static components that are common to all radiation field configurations of interest. The second region is the lower portion of the head, and consists of moving components such as the jaws and multileaf collimators, as well as patient specific collimation devices such as wedges and electron beam cerrobend inserts. The third region is everything below the head including patient geometry. As imaging techniques become more crucial for daily dose calculations, some authors simulate the imaging systems distal to the patient and backtrack the photon fluence to reconstruct the delivered dose to the patient [3].

The results (phase space data) of the first simulation are scored in a plane at the bottom of the region. A particle's phase space* is a collection of variables (position, direction, velocity, energy, particle type, weighting factor, location of first and last interaction, etc.) that describe the particle's behaviour at a certain plane in the simulation geometry. The particles in the first phase space file are used as source input and transported through the second region, under which a second scoring plane is defined. The third simulation samples from the second scoring plane and the results in a 3D dose distribution. A full simulation of a primary particle and all its secondaries is called a particle shower, and a single history includes all the transport details and scored quantities. By simulating a large number of histories average values of macroscopic quantities such as particle fluence, energy spectrum, and absorbed dose distribution can be calculated.

4.1.1 Monte Carlo codes

Some of the well known radiation therapy MC codes are MCNP [4], PENELOPE [5], and GEANT [6]. One of the more popular codes, and the code used in this thesis is EGSnrc (Electron-Gamma-Shower) [7-9]. It was developed at the National Research Council (Ottawa, Canada) and is an extended version of EGS4 originally developed at the Stanford Linear

* The term phase space is used according to the terminology of the EGSnrc particle transport code.

Accelerator Centre. The EGSnrc code is a general purpose package for MC simulation of coupled electron-photon transport in arbitrary geometries with an energy range applicable to 1 keV - 10 GeV. The code is not fast enough for routine clinical treatment planning but is known to be very accurate under non-charged particle equilibrium, such as in the build up region, at the boundary of heterogeneities, and during deliveries with moving collimation [10]. Within the EGSnrc family of codes is BEAMnrc [11] and DOSXYZnrc [12]; developed as part of the OMEGA project (with the University of Wisconsin) for 3D treatment planning. BEAMnrc is a system for modeling radiation therapy sources and DOSXYZnrc is a system for calculating dose distributions in rectilinear voxel phantoms.

MC algorithms are notoriously slow and new calculation techniques have been suggested to improve efficiency such as Macro Monte Carlo [13] and Voxel Monte Carlo (VMC) [14] for electron beams, and Super Monte Carlo [15] and PEREGRINE [16] for photon beams. The second MC code used in this work is XVMC [17], which is based on VMC for electron beams. XVMC was chosen for studies requiring a lot of calculations such as when many patients were involved (Chapters 7 and 8), or when a few patients required many dose calculations (Chapter 6).

4.2 Particle interactions and transport

Ionizing radiation can be either indirectly ionizing (neutral particles) such as photons and neutrons, or directly ionizing (charged particles) such as beta particles, protons, alpha particles, and heavy ions. Indirectly ionizing radiation deposits energy in a two step process. First, energy is transferred from uncharged to charged particles, and second, charged particles deposit energy through Coulomb interactions with other charged particles causing damage to the medium. The energy transferred from ionizing particles to the absorbing medium is called the energy imparted, and is only concerned with the energy that remains within the volume of interest. Absorbed dose is the expectation value of the energy imparted per unit mass, and is defined at a point. Dose is considered the most important radiation dosimetric quantity because it quantifies locally absorbed energy leading to biological damage. MC simulations transport ionizing radiation particles and track their energy deposition. Radiation transport has five major components:

- a definition of the geometry through which the particle traverses, including voxel boundary crossing logic;

- cross-section data is used to derive probability distributions for each interaction type, and the distance to the next interaction (dependent upon the energy of the incident particle and the physical properties of the absorber);
- a (pseudo) random number generator to arbitrarily sample the probability functions;
- a method for scoring quantities of interest;
- and a transport algorithm that calls on the above information at the appropriate time.

Once the problem has been initialized, with particle specification and medium physical and geometrical properties, the transport algorithm commences. A random number generator is used to: sample source particle energy, direction, starting position, etc.; sample the distance to the first interaction site from probability distributions; sample the type of interaction; and sample energy, direction, etc., of all resultant particles (Compton electrons, scattered photons, photoelectric electrons, characteristic photons, Auger electrons, pair/triplet electrons and positrons). The dosimetric quantities from all resultant particles in the volume of interest are scored. The process is repeated with a new particle until a statistical uncertainty in the scored quantity of interest is achieved.

4.2.1 Photons

Energy can be lost from photons to charged particles via four types of interactions that dominate in the radiation therapy energy range of interest. In order of probability of occurence from lower energy photons to higher energy photons they are: the photoelectric effect; Rayleigh scattering; Compton scattering; and pair/triplet production, each described by their respective linear attenuation coefficient, $\mu_i(h\nu, Z)$. Photon attenuation is governed by the well known exponential attenuation law so that the probability that a photon does not interact after traveling a distance z is given by $e^{-\mu z}$. Photon transport refers to deciding the distance between interactions and is therefore described by,

$$z = \frac{1}{-\sum_i \mu_i} \ln(1 - R) \tag{4.1}$$

where R is a random number. Once the particle's path length, z, is determined, the type of interaction is sampled from the appropriate relative probability obtained from the ratio of cross sections $\sigma_i \Big/ \sum_i \sigma_i$.

4.2.2 Electrons

Whereas photons may pass through matter with a small number of interactions and little energy loss, or participate in a limited number of catastrophic events, charged particles interact with essentially every atom they pass. Light charged particles (electrons and positrons) can interact with the absorber through soft collisions or hard collisions resulting in atomic excitation or ionization, respectively, through radiative events producing bremsstrahlung or annihilation photons, or through elastic scattering.

One of the main difficulties in describing electron transport is the very large number of interactions that take place, often resulting in only minor changes in energy and direction of travel. This makes an event-by-event simulation unrealistic due to limitations in computing power. Modern MC electron transport uses condensed history techniques, first introduced by Berger [18], which sample from distributions that describe large numbers of transport and collision processes. In this manner many processes are condensed into a single electron step. The condensed history techniques used in the EGSnrc system have been shown to produce an accurate implementation for the most stringent tests of ionization chamber simulations and backscattering scenarios [8].

4.3 Linear accelerator modeling

In BEAMnrc each part of a tretament unit is called a component module, and can be specified with geometry, material, and certain variance reduction techniques. Models of Varian linear accelerators (Varian Medical Systems, Inc., Palo Alto, CA) were simulated using a collection of component modules (phase space files could be scored under each one) whose geometry was according to the manufacturer's specifications. Figure 4.1 is a schematic diagram of a 100 cm isocentric CL 21EX in electron mode. The model includes a monoenergetic cylindrical electron beam passing through the primary collimator and incident on the vacuum exit window, dual scattering foils, monitor chamber, light field mirror, shielding, adjustable upper and lower secondary collimators (jaws), and electron applicator. The applicator is a collimation device attached to the head of the linac. While photons pass through air essentially unattenuated, as

light electrically charged particles, electrons are easily scattered by air molecules. The electron beam exiting the linac head is collimated with the aid of an electron applicator that extends to a few centimeters above the patient's surface. The bottom of the applicator holds a metal plate with a patient specific cerrobend insert. The electron applicator is shown in Fig. 4.2. The vertical spacers in the applicator were not modeled as they were expected to have minimal impact on dose calculations.

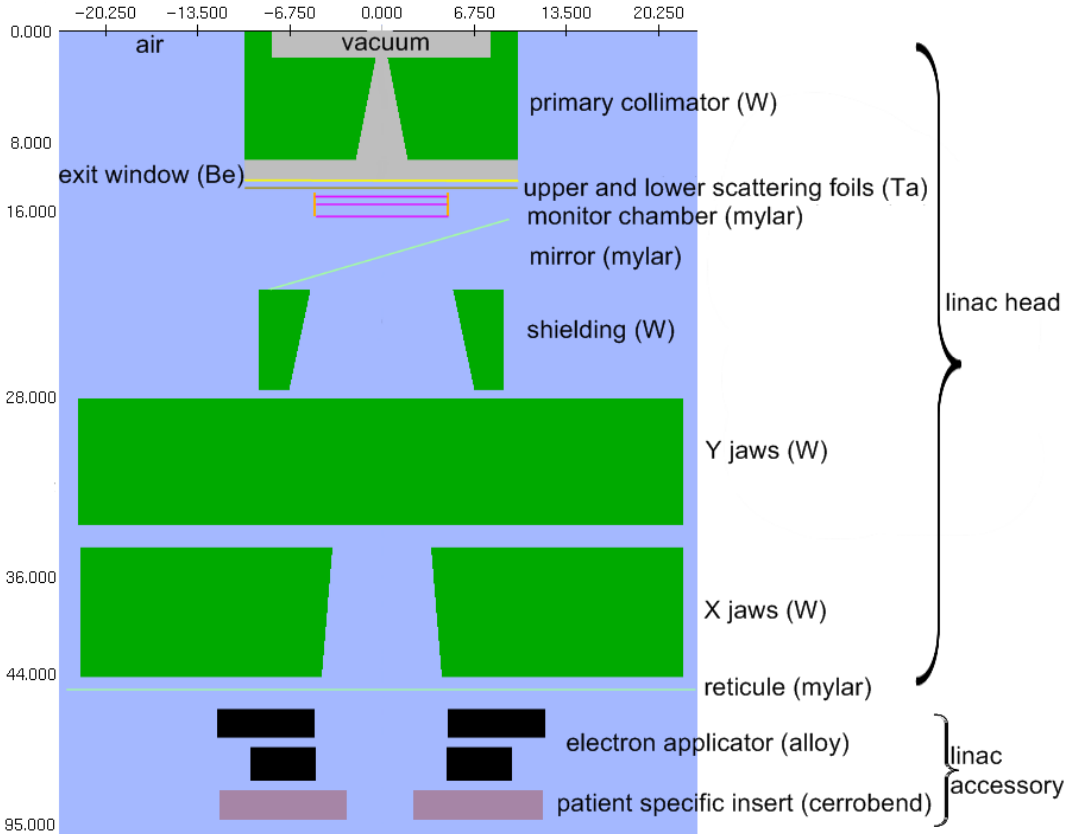

FIG. 4.1 Schematic of linac components (electron beam configuration). The material of each component module is specified in parentheses. The axis labels are in centimetres. The vertical axis is not to scale.

In photon mode, the monoenergetic cylindrical electron beam impinges on a tungsten/copper target and produces primarily forward scattered bremsstrahlung collimated by the primary collimator. The scattering foils are replaced with a copper flattening filter to even out the intensity horizontally. Above the reticule resides a tungsten MLC, which is completely

open in electron mode and so not modeled, but used exhaustively in photon mode. The models are discussed in their relevant chapters.

FIG. 4.2 The electron applicator that mounts on the bottom of the linac head. The black arrows indicate where a cerrobend insert slides into the bottom plate in the applicator.

4.4 Dose calculations in a computed tomography matrix

In radiation therapy typically only CT (or more recently cone beam CT) images of the patient are available for dose calculations. MC algorithms extract material chemical composition and mass density applied to CT images when performing particle transport. This is made possible by dividing the range of Hounsfield units into bins, with each bin corresponding to a definite material, and by assigning mass density based on linear interpolation of a density versus CT number curve (Fig. 4.3).

The conversion in this work was determined by comparing a CT scan (Philips Brilliance CT Big Bore Oncology CT scanner) of a phantom with inserts of known chemical composition and mass density similar to human tissue (Fig. 4.4). This calibration curve was specific for breast patients and was acquired at 120 kVp and 284 mA, similar to patient CT image acquisition (120 kVp, 230 mA). It was used for all DOSXYZnrc dose calculations (Chapter 9). Cross-section data for all materials used in a MC simulations must be specified. The cross-sections for photon interactions used the XCOM data from Berger and Hubbell [19], while the stopping powers, including the density effect, were imported from the NIST database developed by Berger and Seltzer [19].

In XVMC explicit material specification is circumvented by directly relating the CT Hounsfield unit numbers to material interaction coefficients, based upon parameterization of materials representative of the patient [14], for example those tabulated in ICRU Report 46 [21].

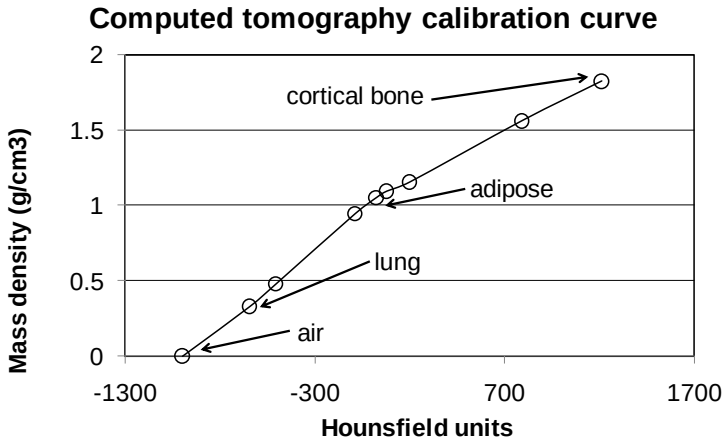

FIG. 4.3 Computed tomography calibration curve for EGSnrc simulations.

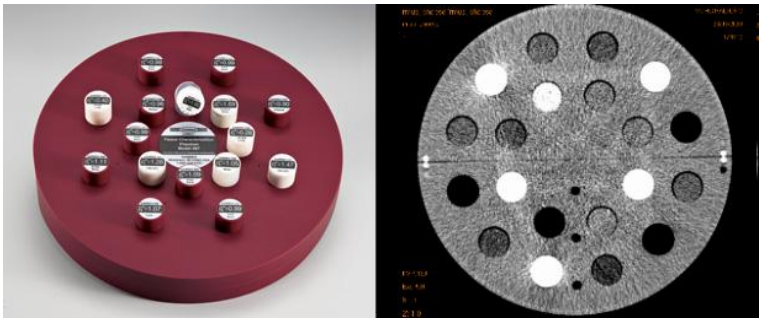

FIG4.4 The Gammex 467 tissue characterization phantom (Gammex, Middleton, WI), and corresponding computed tomography image.

4.5 Reference dose calibration

In EGSnrc calculations with a BEAMnrc simulated source (phase space file), doses are normalized by the number of primary histories incident in the BEAMnrc simulation. Calculation of the dose requires multiplication by conversion factors under reference conditions (central axis, depth of dose maximum in water, 10 x 10 cm^2 field defined at 100 cm source-to-surface distance), and is specific to the beam model used (including the energy of the incident electron beam).

Linacs are calibrated in terms of the dose to a reference point (depth of dose maximum, or 10 cm, etc.) per monitor unit (MU), 100 cGy/100 MU, so that the prescription is given in terms of Gy and treatment is delivered in terms of MUs. An MU is a quantity to denote the monitor chamber reading for a specified amount of radiation. The dose from a single MC simulated treatment field is calculated as,

$$D_{converted}^{MC}[Gy] = \left(\frac{D_{ref}^{calibration}[Gy/MU]}{D_{ref}^{MC}[Gy/particle]} \right) \left(D^{MC}[Gy/particle] \right) B(x,y) \left(MU \right) \qquad (4.2)$$

where

$D_{converted}^{MC} = [\text{Gy}]$ converted MC calculated dose for the specified monitor units in the treatment plan

$D_{ref}^{calibration} =$ [100 cGy/ 100 MU] linac calibration value (measured dose to the reference point under reference conditions)[†]

$D_{ref}^{MC} = [\text{Gy/particle}]$ MC calculated dose under reference conditions, using a simulated digital water phantom

$D^{MC} = [\text{Gy/particle}]$ raw MC calculated dose

$B(x,y) =$ backscatter fraction on the monitor chamber

$MU =$ monitor units prescribed in the treatment plan

For a treatment plan with multiple fields the summed dose is weighted by the MUs per field.

The backscatter fraction accounts for backscattered radiation into the monitor chamber from downstream linac components, causing the monitor chamber to accumulate the required number of MUs to be delivered faster, thereby switching the linac off earlier. This influences the linac output and changes primarily with secondary collimator field size. Verhaegen et al showed that for a 6 MV photon beam the change in backscatter was ‹ 0.5% for square fields of 5 x 5 cm^2

[†] 100 cGy / 100 MU is a linac calibration to dose to water. Dose to other mediums could be used by scaling the cGy / MU calibration by the ratio of mass attenuation coefficients for the medium and water. For instance, a calibration of 100 cGy/100 MU in soft tissue will give 101 cGy/ 100 MU in water.

to 15 x 15 cm^2 [22]. They also noted that the change decreased for higher energy beams, and for a monitor chamber composed of mylar. The backscatter factor was always considered to be unity in this thesis because the photon beam calculations were performed at 6 MV and 18 MV with secondary field sizes up to 10 x 10 cm^2, and the electron beam calculations were all performed at 10 x 10 cm^2.

4.6 Uncertainty

The MC method is a statistical simulation method based on random sampling. The results of a simulation are affected by both systematic and statistical uncertainties. Systematic uncertainties result from the uncertainties in the cross-section data, theories used in the random sampling processes, inaccuracies in simulation geometry, etc. Since, in general, the dosimetric quantities simulated are relative quantities, such as the ratios of dose values under different conditions, the effect of systematic uncertainties is sometimes reduced due to cancellation [1]. Statistical uncertainties can be reduced by running more particle histories so that their effect becomes insignificant for a particular application. However, the statistical uncertainty in a calculated dose will approach the finite latent uncertainty associated with the phase space source, regardless of the number of times that phase space is sampled [23]. A 2%/2 mm criterion (including all uncertainties) has been used to commission MC based dose calculation systems, and has been shown to not significantly affect isodose lines, dose volume histograms, or biological indices [24].

The total dose in each voxel of the patient simulation is highly variable due to the stochastic nature of the simulations. Thus it is unsafe to prescribe and report dose to a point (a voxel). Integrated dose quantities, such as DVHs are less sensitive to statistical uncertainty. Following this method, and as used in this work, the American Association of Medical Physicists Task Group 105 recommends using the fractional uncertainty in the average dose for voxels with dose values greater than 50% of the maximum dose [25].

4.6.1 Variance reduction techniques

Every MC simulation results in statistical estimates of calculated quantities by averaging the scored value over a given set of particle histories. The variance in a scored value is an estimate of the standard deviation from many histories, and using the central limit theorem the standard deviation decreases with an increased number of simulated particles as $N^{-1/2}$, in the limit of infinite N. For clinical applications, a standard deviation of about 2% is desirable for the region

around the point of maximum dose, yet a full simulation of all particle showers for each history is time consuming [10]. Variance reduction techniques are used to reduce the time it takes to calculate a result without altering the variance. Assuming that the average value of quantities from a sample population is distributed normally, the efficiency, ϵ, of a simulation is defined as a function of simulation time T, and relative error $s(\bar{x})/\bar{x}$,

$$\epsilon = \frac{1}{\left(s(\bar{x})/\bar{x}\right)^2 T} \tag{4.3}$$

where $\bar{x}$ is the average value from a sample of the population, and $s(\bar{x})$ is the estimated standard deviation of the average. Variance reduction techniques are tricks that reduce the uncertainty in the scored quantities without increasing the number of histories (time).

There are many techniques to increase simulation efficiency and only those used in this thesis will be described. One of the simplest methods to reduce the simulation time for a given number of primary particles is to increase the transport energy cutoffs [26]. Particle transport will terminate once the particles reach the cutoff energy, and their remaining energy will be deposited on the spot. This is useful because both photons and electrons produce a large amount of secondary electrons, the majority of which have small residual ranges, especially in metals with high atomic numbers. If secondary electrons cannot leave the region in which they were produced then tracking them wastes calculation time. Transport energy cutoffs can be specified independently for electrons (ECUT) and photons (PCUT). ECUT is especially useful because in the process of slowing down, a typical fast electron undergoes on the order of 10^5-10^6 collisions with surrounding matter. A rule of thumb is that ECUT should be set to a value for which the residual range is smaller than half the smallest voxel dimension in the simulation. In this thesis the kinetic energy cutoff was set to either 10 keV (ECUT = 521 keV) or 189 keV (ECUT = 700 keV), so that the range in water was 0.003 mm or 0.5 mm, respectively. Photons have much longer ranges than electrons and their common PCUT value is 10 keV. It should be noted that, strictly speaking, modifying transport energy cutoffs is not a true variance reduction technique as it can introduce systematic bias and errors if not used with caution [10].

The fast XVMC particle transport code uses several approximations and simplifications in radiation transport. In XVMC bremsstrahlung photons are produced but their path is not simulated as they often leave the geometry of interest (Fig. 4.5). XVMC also only considers the

photon cross-sections from Compton scattering and pair production. Rayleigh scattering and the photoelectric effect have only a small influence in the energy range used in radiation therapy, each comprising less than 0.08% of the total cross-section in water at energies above 1 MeV. The interactions of secondary electrons are simulated by scaling the distances traveled in water by the physical density in each voxel.

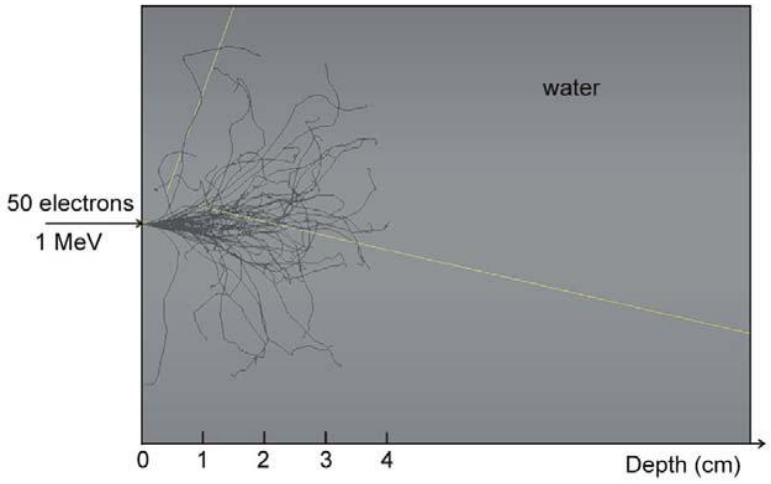

FIG. 4.5 A 1 MeV electron pencil beam incident on a water phantom. The jagged black lines represent electron multiple scattering and the two straight lines represent bremsstrahlung photons. Courtesy of J. Seuntjens, McGill University.

4.7 References

[1] Ma CM and Jiang SB. Monte Carlo modelling of electron beams from medical accelerators. *Phys Med Biol* 1999; 44: R157-R189

[2] Udale M. A Monte Carlo investigation of surface doses for broad electron beams. *Phys Med Biol* 1988; 33: 939-954

[3] Jarry G and Verhaegen F. Patient-specific dosimetry of conventional and intensity modulated radiation therapy using a novel full Monte Carlo phase space reconstruction method from electronic portal images. *Phys Med Biol* 2007; 52: 2277-2299

[4] Briesmeister JF. MCNP — a general Monte Carlo N-particle transport code. Technical Report LA-12625-M (Los Alamos National Laboratory, 1993)

[5] Salvat F, Fernandez-Varea JM, and Sempau J. PENELOPE, a code system for Monte Carlo simulation of electron and photon transport. (OECD Nuclear Energy Agency, 2001)

[6] Agostinelli S, et al. Geant4 — a simulation toolkit. Nucl Inst and Meth in *Phys Research*, Section A, 2003; 506: 250-303

[7] Kawrakow I. Accurate condensed history Monte Carlo simulation of electron transport I. EGSnrc, the new EGS4 version. *Med Phys* 2000a; 27: 485-498

[8] Kawrakow I. Accurate condensed history Monte Carlo simulation of electron transport II. application to ion chamber response simulation. *Med Phys* 2000b; 27: 499-513

[9] Kawrakow I and Rogers DWO. The EGSnrc code system: Monte Carlo simulation of electron and photon transport. PIRS 701 (NRCC, 2003)

[10] Verhaegen F and Seuntjens J. Monte Carlo modelling of external radiotherapy photon beams. *Phys Med Biol* 2003; 48: R107-R164

[11] Rogers DWO, Faddegon BA, Ding GX, Ma CM, Wei J, and Mackie TR. BEAM: A Monte Carlo code to simulate radiotherapy treatment units. Med Phys 1995; 22: 503-524

[12] Walters BRB and Rogers DWO. DOSXYZnrc Users Manual. PIRS 794 rev B (NRCC, 2007)

[13] Neuenschwander H and Born E. A macro Monte Carlo method for electron beam dose calculations. *Phys Med Biol* 1992; 37: 107-125

[14] Kawrakow I, Fippel M, and Friedrich K. 3D electron dose calculation using a Voxel based Monte Carlo algorithm (VMC). *Med Phys* 1996;23: 445-457

[15] Keall PJ and Hoban PW. An accuracte 3D x-ray dose calculation method combining superposition and pregenerated Monte Carlo electron track histories. *Med Phys* 1996; 23: 479-485

[16] Hartmann Siantar CL, Bergstrom PM, Chandler WP, et al. "Lawrency Livermore National Laboratory's PEREGRINE project," in LLNL Report No. UCRL-JC-126732 1997

[17] Fippel M. Fast Monte Carlo dose calculation for photon beams based on the VMC electron algorithm. *Med Phys* 1999; 26: 1466-1475

[18] Berger MJ. Monte Carlo calculation of the penetration and diffusion of fast charged particles. *Methods in Comput Phys* 1963; 1: 135

[19] Berger MJ, Hubbell JH, and Seltzer SM. XCOM: Photon cross sections database. NIST Standard Reference Database 8 (XGAM) (Gaithersburg, MD: National Institute of Standards and Technology, 1998)

[20] Berger MJ, Coursey JS, and Zucker MA. ESTAR, ASTAR and PSTAR: Computer programs for calculating stopping power and range tables for electrons, protons and helium ions (version 1.21). Technical report (NIST, 1999)

[21] ICRU (International Commission on Radiation Units and Measurements). Photon, electron, proton and neutron interaction data for body tissues ICRU Report 46 (Bethesda, MD: ICRU, 1992)

[22] Verhaegen F, Symonds-Tayler R, Liu HH, and Nahum AE. Backscatter towards the monitor ion chamber in high-energy photon and electron beams: charge integration versus Monte Carlo simulation. *Phys Med Biol* 2000; 45: 3159-3170

[23] Sempau J, Sánchez-Reyes A, Salvat F, ben Tahar HO, Jiang SB, and Fernández-Varea JM. Monte Carlo simulation of electron beams from an accelerator head using PENELOPE. *Phys Med Biol* 2001; 46: 1163-1186

[24] Keall PJ, Siebers J, Jeraj R, and Mohan R. The effect of dose calculation uncertainty on the evaluation of radiotherapy plans. *Med. Phys* 2000; 27: 478-484

[25] Chetty IJ, Curran B, Cygler JE, et al. Report of the AAPM Task Group No. 105: Issues associated with clinical implementation of Monte Carlo-based photon and electron external beam treatment planning. *Med Phys* 2007; 34: 4818-4853

[26] Bielajew AF and Rogers DWO. "Variance reduction techniques," in Monte Carlo transport of electrons and photons, ed, TM Jenkins, WR Nelson, and A Rindi, 861-920 (New York: Plenum, 1988)

CHAPTER 5

Evaluation of a prototype 3D ultrasound system for multimodality imaging of cervical nodes for adaptive radiation therapy

In this chapter, we present a conference publication in the *Proceedings of SPIE Medical Imaging 2007: Visualization and Image-Guided Procedures*. This was an evaluation of a commercial 3D ultrasound system for imaging cervical lymph nodes in the neck. Although readily used in diagnostic radiology, this is a not a traditional site for ultrasound in radiation therapy. Therefore we proposed to monitor superficial neck tissue with malignant disease on a regular basis throughout treatment.

The original equipment application was for transabdominal prostate imaging and much of the system remains the same for other site applications, such as the philosophy of comparing interfraction ultrasound images with a reference ultrasound image (intramodality referencing) instead of with the CT simulation dataset. The most obvious change for neck scanning is the use of a higher frequency 10 MHz linear array probe instead of a 3.5 MHz curvilinear transabdominal probe. The arrangement of the infrared emitters on the probe, which are used to track the probe in 3D space, was also changed from a 4 marker design to a 16 marker design allowing for a greater range of motion. We describe in detail the equipment and image acquisition procedure. Hardware and software changes that were suggested to and implemented by the manufacturer.

Title: Evaluation of a prototype 3D ultrasound system for multimodality imaging of cervical nodes for adaptive radiation therapy

Authors: Fraser D, Fava P, Cury F, Vuong T, T Falco, and Verhaegen F

Published in the Proceedings of SPIE Medical Imaging 2007: Visualization and Image-Guided Procedures, Volume 6509, (2007) 65090Y (8pp)
doi: 10.1117/12.709299

5.1 Abstract

Sonography has good topographic accuracy for superficial lymph node assessment in patients with head and neck cancers [1]. It is therefore an ideal noninvasive tool for precise interfraction volumetric analysis of enlarged cervical nodes. In addition, when registered with computed tomography (CT) images, ultrasound information may improve target volume delineation and facilitate image-guided adaptive radiation therapy. A feasibility study was developed to evaluate the use of a prototype ultrasound system capable of three dimensional visualization and multimodality image fusion for cervical node geometry. A ceiling mounted optical tracking camera recorded the position and orientation of a transducer in order to synchronize the transducer's position with respect to the room's coordinate system. Tracking systems were installed in both the CT-simulator and radiation therapy treatment rooms. Serial images were collected at the time of treatment planning and at subsequent treatment fractions. Volume reconstruction was performed by generating surfaces around contours. The quality of the spatial reconstruction and semiautomatic segmentation was highly dependent on the system's ability to track the transducer throughout each scan procedure. The ultrasound information provided enhanced soft tissue contrast and facilitated node delineation. Manual segmentation was the preferred method to contour structures due to their sonographic topography.

5.2 Introduction

Image guided radiation therapy (IGRT) strives to account for tumour motion and patient set-up errors. It developed out of the need for tighter target and organ at risk margins as required by precision radiation therapy. Images acquired immediately after patient set-up on the treatment couch, and before beam delivery, are used to correct for interfraction organ position relative to reference images. Figure 5.1 illustrates the feedback loop around image guidance and beam delivery in the context of the treatment planning process. Image guided adaptive radiation

therapy (IGART) expands the loop to include information acquired during treatment in order to adjust the treatment plan. Common in patients with head and neck tumour sites, dose delivery can be modified to compensate for changes in tumour volume and geometry, as well as patient weight loss. Both IGRT and IGART are dependent upon a reference CT image defined at the time of treatment planning, while efficient daily information is often gathered using a different imaging modality. Multimodality registration of images acquired at different times, and including organ motion, is not straight forward. This feasibility study describes a prototype 3D ultrasound system for cervical node imaging, which is capable of multimodality image fusion of data acquired sequentially in the CT room, and intramodality image fusion of data acquired in the treatment room.

Initial applications of external beam radiation therapy used simple planning techniques consisting of visual inspection of the patient's surface to define the treatment area. Subsequently x-rays in the kilovoltage range, and later megavoltage range, improved target definition largely through bony anatomy visualization despite the dose to the patient. Modern treatment planning systems (TPS) are CT based and employ patient specific geometrical information to develop treatment plans. Using a CT-simulator (similar to a diagnostic CT but with a flat couch, larger bore, and a room coordinate system), anatomical information of the patient in the treatment position is acquired. The images are imported into a TPS whereby beam geometry is overlaid on the anatomy to produce an optimized dose distribution, providing a maximum dose to malignant regions while sparing healthy tissue. Currently CT-sim images are well integrated into the treatment planning process because the images are referenced to the coordinate system in the CT-sim room and matched to the coordinate system in the treatment room. This greatly facilitates the transfer of planning information between patient and linear accelerator. Figure 5.1 describes a) the treatment delivery process for ultrasound guided therapy, and b) the theoretical treatment delivery process with the prototype system used in this study.

Assessment of the relative orientation between patient alignment on the treatment couch and the treatment fields has been performed using portal images, cone beam CT, and daily CT-sim images. Portal images are acquired in the treatment room and use a small fraction of the megavoltage treatment beam as the imaging beam. The images are a projection of the patient in 2D, and suffer from large amounts of scatter resulting in low contrast and image artifacts [2-4]. Images acquired with kilovoltage cone beam CT present a 3D alternative but are degraded in the presence of high atomic number material, while megavoltage cone beam CT exhibits the same

characteristics of port-films. Cone beam CT also delivers additional dose to the patient and is highly dependent on the image correction and reconstruction algorithm [5].

Small changes in patient shape and set-up errors are accounted for by adding margins to the target volume. Ideally the margins are reduced as much as possible. For example, radiation beam geometries and fluence patterns have become increasingly complex and make use of tighter margins and steep dose gradients, leading to the need for more accurate target and organ at risk localization.

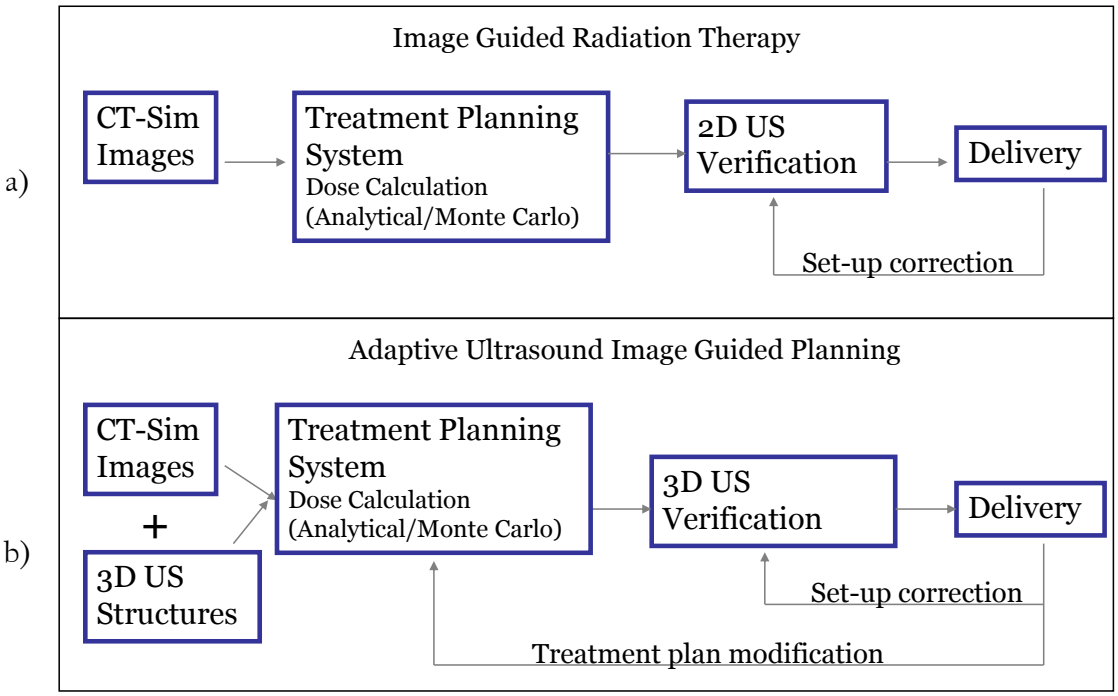

FIG. 5.1 The flow chart emphasizes the possible uses of ultrasound information in the treatment delivery process for a) IGRT, and b) IGART. The treatment planning process begins with volumetric patient information acquired with a CT-sim. The images are imported into a TPS whereby an optimized treatment plan is developed. The plan (and CT-sim images) is transferred to the treatment room where subsequent images are used for target localization and alignment correction before beam delivery. The images can not only be used for patient set-up corrections but also for modifying the treatment plan.

Despite good surface and bony anatomy alignment, as some image guidance methods use, interfraction organ motion may occur and degrade tumour control [6]. The prostate, situated between the bladder and rectum, is an organ easily imaged with ultrasound to correct for interfraction movement assuming the correct position is known. Image guidance relies on accurately registering the patient and treatment room geometries. Popular practice employs grouped contours defined from CT data visually superimposed on two orthogonal B-mode ultrasound images. Studies have also shown that CT prostate volumes may be as much as 30-50% greater than transrectal ultrasound volumes [7-9]. The discrepancy has been attributed to CT slice thickness and the inability to discern the extent of the base and apex of the prostate (without contrast) [7,10]. The uncertainty in the superior-inferior direction has also led to systematic prostate localization differences between CT and transabdominal ultrasound [11]. Daily ultrasound localization in the treatment room has been compared to daily CT images in the CT-sim room, and a good correlation in organ targeting was found. Nevertheless CT localization requires significant technological and human resources that limit this application [12]. Patient set-up using portal images has been compared to ultrasound, and it was found that significant prostate motion occurred, unrelated to the position of bony anatomy [6,13]. Volume changes in such soft tissue targets may also lead to a re-evaluation of the treatment plan. Cross modality image registration provides additional anatomical information. Nevertheless, previous cross modality comparisons between the reference and treatment times have shown the disadvantages and inconsistencies of different imaging modalities.

Sonography is a highly sensitive technique for examination of cervical lymph node metastases. It is therefore an ideal noninvasive tool for precise interfraction volumetric analysis of metastasized cervical nodes. In addition, when registered with CT images, ultrasound information may improve clinical target volume (CTV) and planning target volume (PTV) delineation.

5.3 Equipment

The ultrasound system used in this study is based on 3D target visualization, intermodality registration, and intramodality position referencing. It uses two tracking systems; one in the CT-simulator room and one in the treatment room. Ultrasound images taken at the time of treatment planning in the CT-sim room are the reference for organ positioning, and are compared to ultrasound images taken at the time of treatment for approximately thirty-six fractions. A volume of the scanned area is constructed from 2D serial image slices. 3D

intramodality position referencing eliminates cross modality discrepancies and provides complete geometrical information of the treatment area. The ultrasound reference image and planning CT image can be registered for improved organ delineation. Figure 5.2 describes the image acquisition flow process.

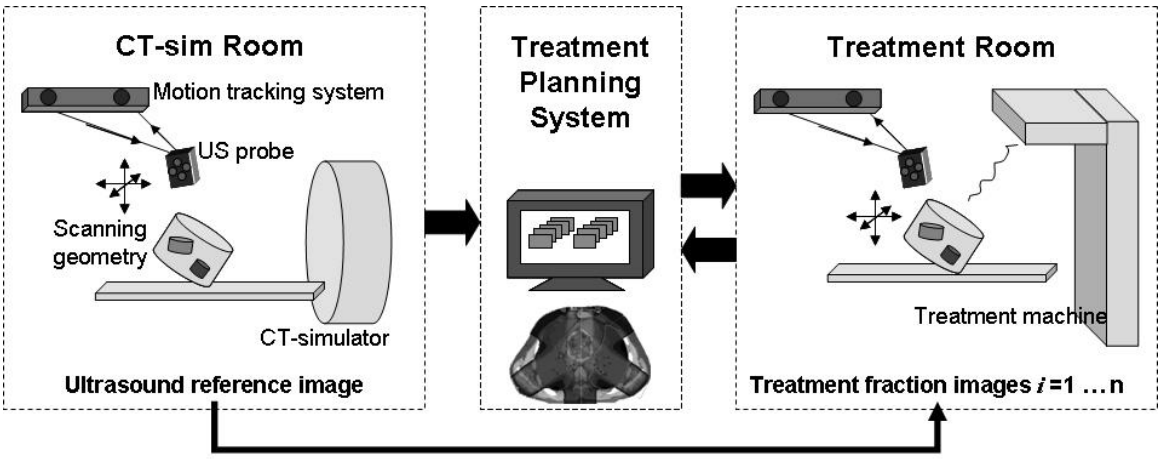

FIG. 5.2 On the left, CT-sim and reference ultrasound images are acquired one after the other in the CT-sim room. On the right, daily ultrasound images are subsequently acquired for each radiation fraction in the treatment room.

5.3.1 Tracking system

In order to construct a 3D volume from ultrasound images, a tracking system composed of an optical camera and an infrared emitter array was used. The ultrasound images were obtained with a variable frequency free-hand linear phased array transducer of width 38 mm and operated at 10 MHz. Each image is a two dimensional slice through part of the neck, with depths ranging from 4 cm to 6 cm, depending on patient size and metastasis location. The scanning technique involved transverse scans along the sternocleidomastoid muscle with an anterior rotation near the clavicle. Sagittal scans around the perimeter of the neck were also used. The images were obtained with an average frame rate of twenty frames per second resulting in approximately one hundred and twenty slices. The spatial relationship between the frames was derived as the location of the transducer was tracked. Attached to the front of the transducer was an array with active infrared markers. The probe was tracked with a ceiling mounted real

time Polaris tracking system. The number of markers, and their position, on the probe evolved throughout the project with scanning experience and technique.

Figure 5.3 illustrates changes in the probe design. Unlike transverse scans of the abdomen where the emitters directly face the camera, transverse neck scans may block the camera line of sight behind the shoulders. In addition, maintaining contact with the skin, while remaining visible to the camera, was not straight forward for areas with large masses that deformed the neck surface. Sagittal scanning required markers angled almost ninety degrees from the scan direction.

The initial marker design involved four markers arranged evenly around the perimeter of an oval as shown on the left of Fig. 5.3. This design worked well for transabdominal images, which was the original application of the device. The head and neck application required more flexibility in tracking the emitters at different probe angles and orientations. Subsequent designs incorporated multiple emitters grouped together and arranged in an arc. Three emitter groupings were able to span an angle of 120°. Four emitter groupings, to make a sixteen marker array, were able to span an angle of 120° in one plane and 90° in an orthogonal plane as shown on the right of Fig. 5.3. The sixteen marker array is the finalized array configuration.

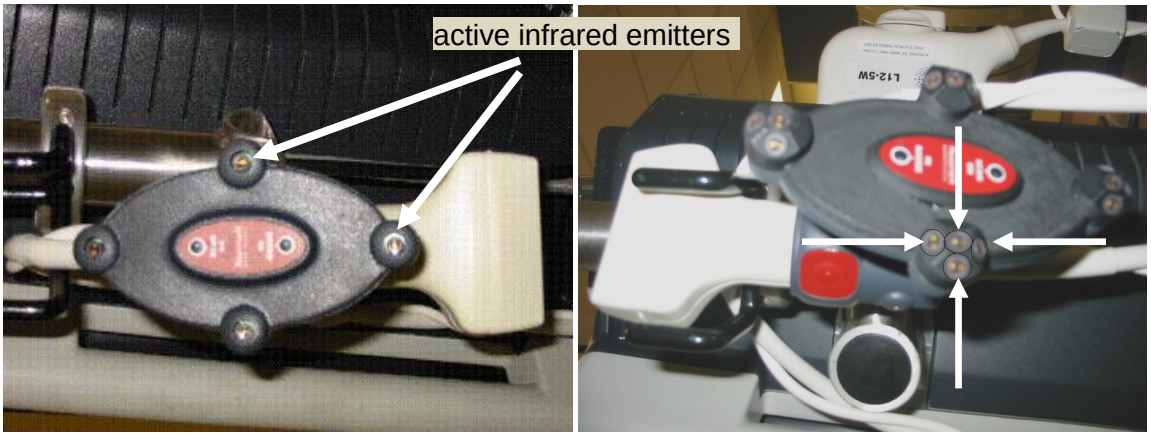

FIG. 5.3 Development of the active infrared emitter array to accommodate the line of sight for probe orientations in a wide range of angles with respect to the camera for neck scanning.

2D image slices are synchronized with their 3D orientation through a set of two coordinate transformations derived from spatial calibrations linking the probe and camera. A homogeneous phantom with known internal structures of different contrast was used to define

the probe coordinate system, whereby the structures' relationship to the probe emitter array was derived from images at multiple angles in the phantom. The phantom also has external passive markers that, when aligned with the lasers in the CT-sim or treatment room, allow the camera to determine the location of the isocentre and define the room coordinate system. Together these two coordinate transformations, the probe and room, provide sufficient information to be able to determine the absolute position of a voxel in the image to the room's frame of reference. As a quality control measure, a tilt detector is mounted on the camera to detect any camera movement, which would alter the calibration values.

5.4 3D ultrasound system for head and neck scanning

5.4.1 Volume determination

Organ volume determination follows image reconstruction and segmentation. It depends on the quality of the 3D reconstruction, which depends on the quality of the image acquisition. A fast scanning technique, or slow frame acquisition rate, requires interpolation between slices that are separated by a large distance. This results in a blurring of data between slices where organ edges are not distinguishable (Fig. 5.4). Another form of missing data occurs if the probe cannot be tracked by the camera. Even though images can be acquired, the lack of spatial information inhibits reconstruction.

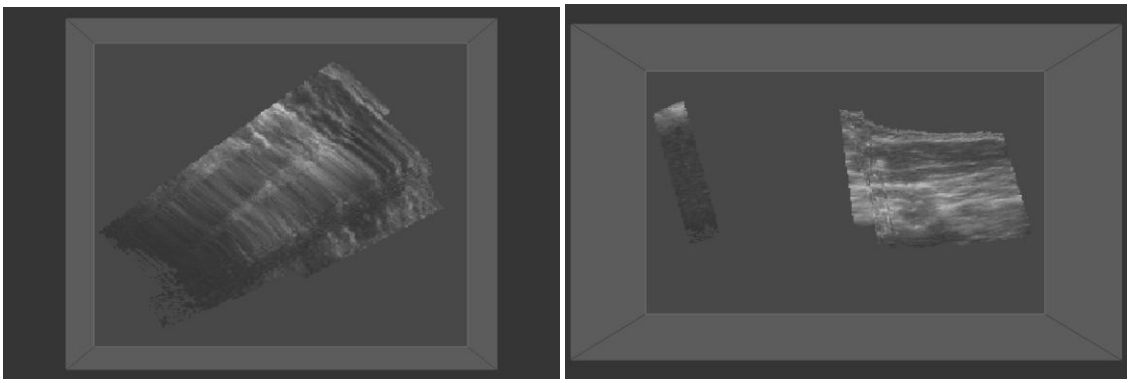

FIG. 5.4 Slices with large separations rely on interpolation between grey scale pixel patterns that may miss important details (left). The interpolation distance is 0.89 cm. If spatial information of the probe is missing, due to blocking of the line of sight between the tracking camera and the infrared markers on the probe, then the volume cannot be reconstructed (right). The missing information spans 4.86 cm.

Several tools were developed for contour segmentation. The semiautomatic process is based on grey scale differences between pixels and a predetermined shape. To run smoothly this process requires a few contours in two of three dimensions as a starting point. It is based on ultrasound characteristics of the prostate, as was the original application. Qualitatively, the system is not able to accurately contour cervical nodes automatically, most likely due to organ geometry differences, the difficulty in contouring small areas (as small as 0.1 cm^3), and because the nodes do not benefit from sharp echo differences with surrounding tissue, as does the prostate base with the bladder. It was found that manual segmentation was the best method for contouring. Fortunately individual nodes are typically not more than 20 mm in the maximum longitudinal axis, although many nodes may exist. It was found that manual contouring is greatly facilitated by viewing the structure of interest from more than one angle. Figure 5.5 provides an example of using reconstruction in the coronal plane to delineate a node in the axial plane.

The top images present the same axial slice where a node was identified and whose boundary was uncertain. The bright echo differentiating the two contours could have been the extent of the node or the hyperechoic central line characteristic of the hilum. The bottom images present different coronal planes whose position is denoted by the white horizontal lines in the axial plane. It is clear from the most anterior coronal plane that the node does not extend into the larger contour. This image set was acquired two weeks after the start of radiation therapy where the node's longitudinal/transverse diameter ratio and volume measured 9.38mm/8.40mm = 1.12 and 0.225 cm^3, respectively, compared to the beginning of treatment when the longitudinal/transverse diameter ratio and volume measured 11.7mm/10.5mm = 1.27 and 0.577 cm^3, respectively.

Figure 5.6 shows a reconstructed axial slice inside the total reconstructed volume (seen as a box). Two nodes are visible after 3D segmentation, and are shown in relationship to the treatment room's isocentre (crosshairs through the box). The volumes of the left and right nodes are 0.577 cm^3 and 0.455 cm^3, and the positions of the centres of the left and right nodes, from the treatment target centered at the room's isocentre, are (-33.05 mm, 49.20 mm, 2.63 mm) and (-16.80 mm, 57.40 mm, 14.03 mm), respectively.

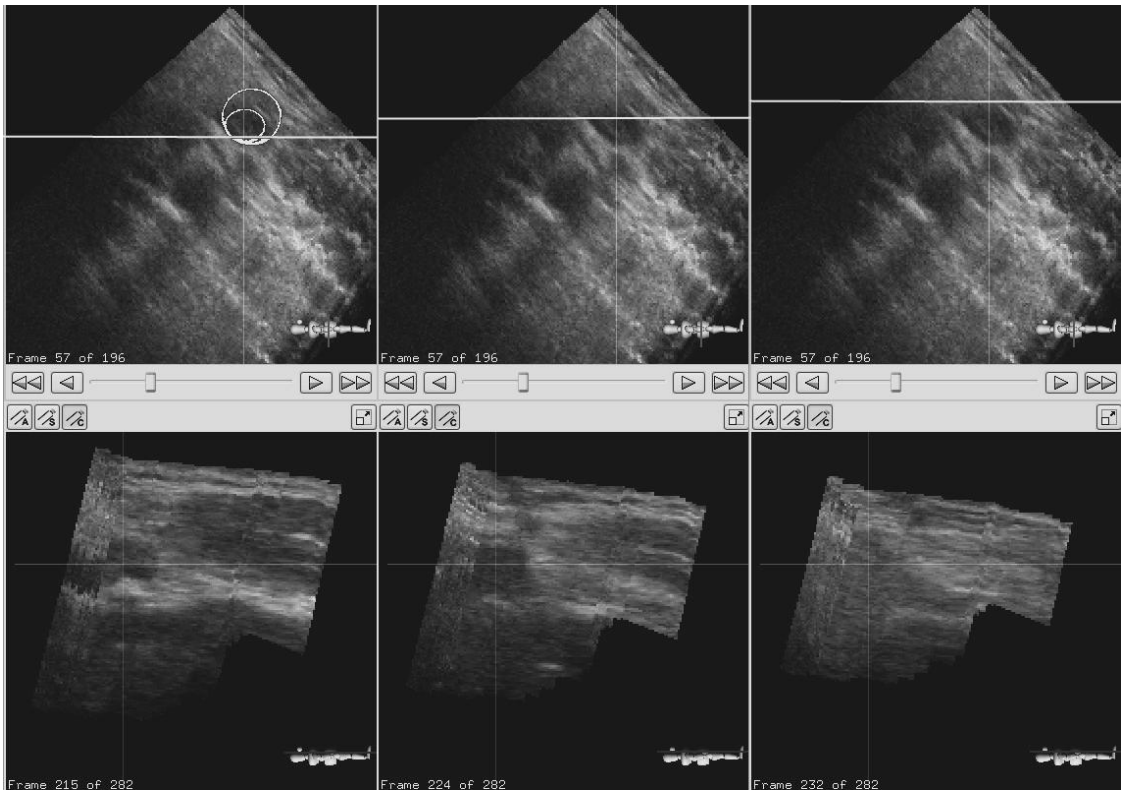

FIG. 5.5 After volumetric reconstruction from a transverse scan, two possible contours of a node are presented in the top left image. All of the top images are of the same axial slice. The bottom coronal slices are at planes denoted by the white horizontal lines in the top images. The coronal view helps define the anterior edge where the axial image does not provide enough information.

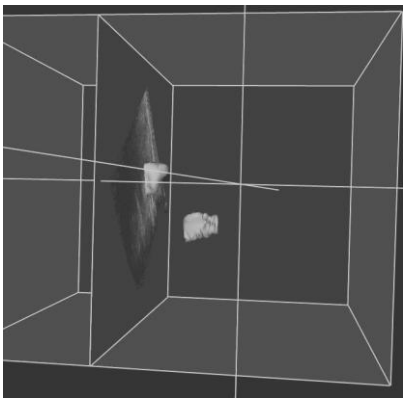

FIG. 5.6 Example of two nodal volumes and one axial slice visualized with respect to the scan volume (box) and treatment room isocentre (crosshairs).

5.4.2 Ultrasound and computed tomography image fusion

3D ultrasound reconstruction is also required for fusion with CT images. Because the ultrasound tracking system has the same frame of reference as the CT, registration is performed automatically. It is limited by the accuracy of the calibration and is independent of soft tissue deformation and image quality [14]. An ultrasound image acquired immediately following the treatment planning CT scan helps to ensure minimal organ motion and good synchronization between x-ray and ultrasound tomographic images. The registered ultrasound images are sampled at the same slice spacing and position as the CT. Figure 5.7 illustrates a fusion match of the phantom. The volume of a sphere as determined from the CT is 0.973 cm^3, and from the ultrasound system is 0.821 cm^3. In the sagittal plane a reverberation ultrasound artifact is visible in the centre of the sphere as the beam is reflected by the parallel edges of the sphere medium. Figure 5.8 illustrates good registration with ultrasound and CT data for a patient.*

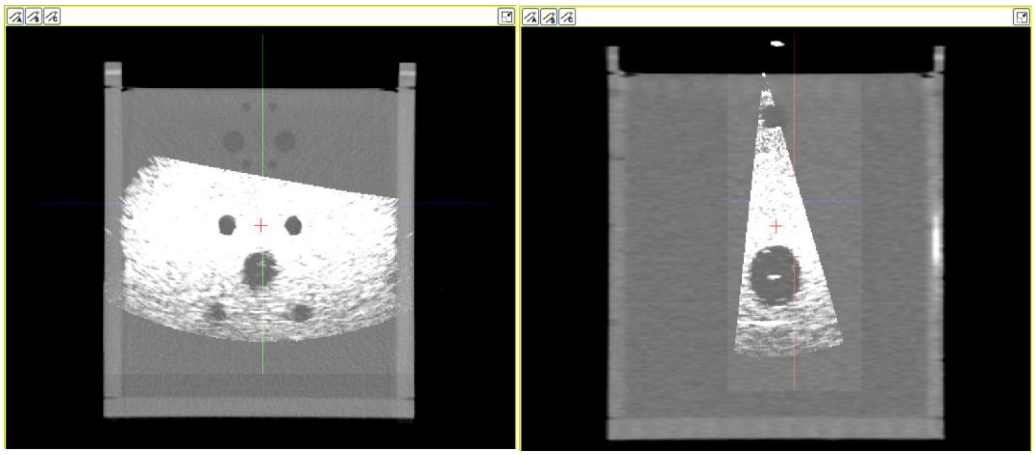

FIG. 5.7 Axial (left) and sagittal (right) images of ultrasound and CT phantom registration.

* Please note that these are the images used for this publication, but that better resolution images are shown in Chapter 7.

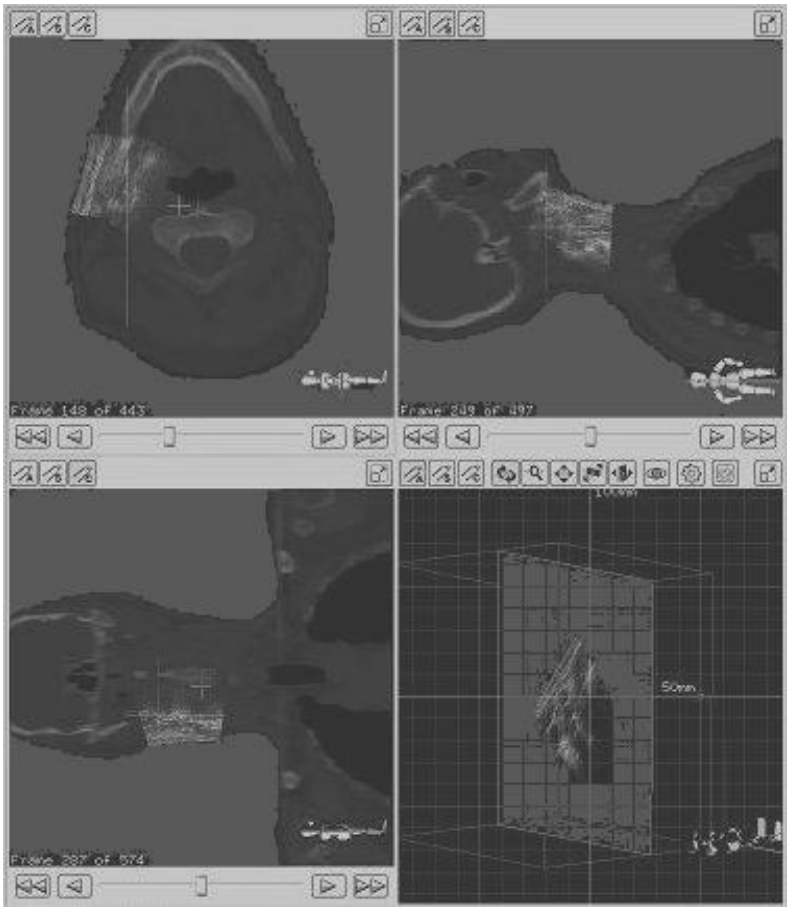

FIG. 5.8 Patient registration in the axial plane (top left), sagittal plane (top right), and coronal plane (bottom left). The bottom right image displays a reconstructed ultrasound axial slice within the scanned boxed volume.

5.4.3 Intramodality position referencing

The same room and probe calibrations apply in the treatment room between the tracking system and the linear accelerator. The simulation and treatment images are thus paired within the same coordinate system. The manufacturer states a calibration precision of 1 mm in each room and an overall precision of 2 mm between rooms. Position referencing uses the isocentre extracted from the radiation therapy plan sent through DICOM protocol in order to know where the radiation target should be located with respect to the treatment machine isocentre. Based on measurements of a spherical structure in the phantom, the average discrepancy and two sigma confidence interval between the two room set-ups was 1.2 ± 2 mm in the left/right direction, 0.4 ± 2.6 mm in the inferior/superior directions, and 0.3 ± 2 mm in the anterior/posterior

direction. Contour definitions are more clear in the anterior/posterior direction because the ultrasound beam is orthogonal to surfaces along the beam axis.

Position referencing for cervical nodes is dependent upon the ability to maintain correct patient alignment and probe pressure during scanning. Head and neck cancer patients are often uncomfortable due to airway restrictions and long treatment times. In addition, weight loss and nodal geometry may cause changes in neck anatomy.

5.5 Conclusion

After some re-engineering, the prototype 3D ultrasound system for a head and neck application was able to track image formation for position referencing and registration, and it was able to reconstruct scanned and contoured volumes. The registration accuracy and precision do not depend on user subjectivity or matching algorithms because they are based on room and probe calibrations that define a common coordinate system. Reconstruction worked best for transverse scans, and intramodality comparisons were facilitated when the same scanning technique was used at each treatment fraction. Manual segmentation was the preferred method of organ contouring because nodal boundaries did not always sharply contrast with surrounding media. Ultrasound image acquisition was efficient and may provide additional information on tissue changes during the course of radiation therapy, with a potential application in adaptive radiation therapy.

5.6 Afterward

In this chapter we presented a prototype ultrasound system for neck scanning. It was shown that changes to an existing system allowed for imaging in this region. Two main features make this system unique in radiation therapy. First, intramodality verification only exists with one other modality, in-room CT, but is not common in the clinic. Second, semi-automatic segmentation is not standard practice in image guidance systems. The majority of the system is the same when imaging other treatment sites. Chapter 6 revisits the neck region and includes a dosimetric study. Prostate imaging is performed in Chapter 8 and breast imaging is performed in Chapter 9.

5.7 References

[1] Bruneton JN, Matter D, Lassau N, Dassonville O. "Lymph Nodes," in Application of Sonography in Head and Neck Pathology, ed JN Bruneton, 137-163 (Germany, Springer-Verlag, 2002)

[2] Boyer AL, Antonuk L, Fenster A, et al. A review of electronic portal imaging devices. *Med Phys* 1992; 19: 1-16

[3] Jaffray DA, Battista J, Fenster A, Munro P. X-ray scatter in megavoltage transmission radiography: Physical characteristics and influence on image quality. *Med Phys* 1994; 21:45-60

[4] Yin F, Guan H, and Lu W. A technique for on-board CT reconstruction using both kilovoltage and megavoltage beam projections for 3D treatment verification. *Med Phys* 2004; 32: 2819-2826

[5] Ning R, Tang X, and Conover D. X-ray scatter correction algorithm for cone beam CT imaging. *Med Phys* 2004; 31: 1195-1202

[6] Little DJ, Dong L, Levy L, Chandra A, and Kuban DA. Use of portal images and BAT ultrasonography to measure set-up error and organ motion for prostate IMRT: implication for treatment margins. *Int J Radiat Oncol Biol* 2003; 56: 1218-1224

[7] Kälkner KM, Kubicek G, Nilsson J, et al. Prostate volume determination: Differential volume measurements comparing CT and TRUS. *Radiother Oncol* 2006; 81: 179-183

[8] Hoffelt SC, Marshall LM, Garzotto M, et al. A comparison of CT scan to transrectal ultrasound-measured prostate volume in untreated prostate cancer. *Int J Radiat Oncol Biol* 2003; 57: 29-32

[9] Narayana V, Roberson P, Pu AT, et al. Impact of differences in ultrasound and computed tomography volumes on treatment planning of permanent prostate implants. *Int J Radiat Oncol Biol* 1997; 37: 1181-1185

[10] Sandler HM, et al. Localization of the prostatic apex for radiation therapy using implanted markers. *Int J Radiat Oncol Biol* 1993; 27: 915-919

[11] McNair HA, Mangar SA, Coffey J, et al. A comparison of CT and ultrasound-based imaging to localize the prostate for external beam radiotherapy. *Int J Radiat Oncol Biol* 2006; 65: 678-687

[12] Lattanzi J, McNeeley S, Pinover W, et al. A comparison of daily CT localization to a daily ultrasound-based system in prostate cancer. *Int J Radiat Oncol Biol* 1999; 43: 719-725

[13] Powell TM, Van den Heuvel F, Kahn M, and Forman JD. Independent prostate motion as measured by daily BAT ultrasound and electronic portal imaging. *Int J Radiat Oncol Biol* 2001; 51(Suppl 1): 215

[14] Foroughi P, Abolmaesumi P, and Hashtrudi-Zaad K. Intra-subject elastic registration of 3D ultrasound images. *Med Image Anal* 2006; 10: 713-725

CHAPTER 6

The dosimetric impact of geometrical changes in cervical node-positive disease using 3D ultrasound imaging

In this chapter we present a manuscript submitted to the peer reviewed journal *Radiotherapy and Oncology*. This case study is a follow up study from Chapter 5, and determines the dose to changing anatomy for head and neck cancer patients using 3D ultrasound as the localizing imaging modality.

It is common to use intensity modulated radiation therapy for the head and neck region due to the complex geometry of the targets and surrounding healthy tissue. IMRT techniques inherently incorporate a simultaneous boost to the target because they allow dose escalation to smaller parts of the volume to be treated. Therefore replanning throughout treatment is not performed unless there are visible changes in the patient. But anatomical changes may take place weeks before they are visible to the eye (with or without radiographic imaging), necessitating frequent in-room imaging. This is a retrospective dosimetric study using ultrasound images obtained during the course of treatment. Therefore no patient realignment was performed and the dosimetric errors associated with missing the target are real. Implementation of ultrasound IGRT for head and neck cancers is discussed in order to prevent future such errors.

Title: The dosimetric impact of geometrical changes in cervical node-positive disease using 3D ultrasound imaging

Authors: Fraser D, Poon E, Fava F, Vuong T, Falco T, and Verhaegen F

Submitted to Radiotherapy and Oncology October 2009

6.1 Abstract

Purpose: To geometrically monitor disease-positive cervical lymph nodes in patients with head and neck cancers using 3D ultrasound image guidance, and to evaluate the dosimetric impact with Monte Carlo dose calculation techniques.

Methods and materials: Two typical patients cases are reported on; 1) a shrinking node, and 2) weight loss and a displaced node. Ultrasound images were acquired for several fractions during treatment delivery, and a trained sonographer contoured the lymph nodes of interest. Dose calculations quantified the dosimetric impact of changing nodal geometry and position, as well as a changing patient habitus in time frames relevant to radiation therapy.

Results: The volume of the shrinking node decreased to 17% of its initial size after 33 fractions. The average of the mean fraction doses to the node was 10 cGy (5%) higher than the prescribed dose. Because the node was located in a homogeneous region the mean nodal doses per fraction were within 2 cGy of each other. For the patient who lost weight, the node's centre of mass moved up to 1.3 cm away from the position at fraction 1, causing a decrease in D95 of 4.5%.

Conclusion: Routine image guidance shows that neck tissue deformation causes misalignment in parts of the target volume. When using intensity modulated radiation therapy techniques, cervical node dose coverage may be improved if image guidance is used as a trigger to determine when adaptive replanning may be necessary.

6.2 Introduction

One of the many factors for successful image guided radiation therapy (IGRT) is how well the dose is maintained at the target [1-3]. Head and neck cancer patients often experience marked anatomic changes due to primary tumour and lymph nodal mass reduction, as well as weight loss causing geometrical changes in target definition throughout treatment. These changes to soft tissue may not be visible without sensitive imaging techniques, and may have already progressed substantially before physical changes are noticed. No consensus exists on triggers for reimaging and replanning [4] despite reported discrepancies in the delivered dose due to anatomic changes [5-7].

More than 90% of head and neck cancers are squamous cell carcinomas, and 80% of nasopharyngeal squamous cell carcinomas have positive nodal involvement [8]. The development of recurrent tumours in the neck is the single most common type of treatment failure in these patients, and nasopharyngeal cancers are reported to have the highest morbidity rate for long term survivors [9,10]. Target localization and response monitoring throughout treatment are essential.

Current image guidance systems for head and neck cases include portal imaging, megavoltage/kilovoltage cone beam computed tomography (CT), megavoltage tomotherapy units, and integrated CT/linear accelerators. However, since the 1980s ultrasound (US) has been a valuable tool for cervical node examination and yet it has not been fully realized in radiation therapy. It has good topographic accuracy for superficial lymph node assessment in patients with head and neck cancers, and is an ideal noninvasive tool for precise interfraction volumetric analysis of enlarged cervical nodes [11]. Compared to CT, US has been shown to be superior in depicting nodal structure resulting in higher sensitivity and specificity [12-15]. Magnetic resonance has also been shown to be a sensitive technique for assessing nodal involvement but is limited by expense, personnel, time/availability, and online imaging capabilities [16-18]. The main advantages of US over the above mentioned modalities are that it is noninvasive, cost effective, real-time, and image guidance can be completed within about five minutes [19].

This case study uses 3D US to investigate the dosimetric impact of changes in position and geometry of two patients with disease positive cervical lymph nodes treated with intensity modulated radiation therapy (IMRT). The dosimetry is discussed in terms of using image guidance for hypothetical patient repositioning or adaptive replanning. The dosimetric impact in treatment plans are evaluated with Monte Carlo (MC) techniques in order to properly account for heterogeneities and irregular surfaces in the head and neck region, and to more accurately model the treatment beam geometry [20].

6.3 Methods and materials

6.3.1 Ultrasound system

The Restitu system (Resonant Medical Inc., Montréal, QC (now known as Clarity)), was used for 3D US image acqusition in this study. The system is calibrated to the treatment room's isocentre allowing the position of US images to be referenced to the isocentre, permitting automatic intermodality (US to CT) and intramodality (US to US) image fusion. This study

makes use of images captured in the treatment room. A high frequency 10 MHz linear phased array transducer was used to permit higher resolution at shallow depths. The width of the transducer was 3.8 cm allowing for good contact with the neck surface with minimal transducer pressure. The generic system calibration process and procedure for measuring interfraction organ motion are outlined in Johnston et al [20]. Similar to that study we also found reproducibility within 0.5 mm for daily and monthly phantom measurements in the CT-simulator room. A more complete technical description of the system is given in Fraser et al [21].

6.3.2 Patients

Two patients diagnosed with carcinoma of the nasopharynx and positive cervical lymph nodes are reported on as representative of two distinct cases; 1) a shrinking node, and 2) weight loss and a displaced node over the treatment course. The patients were treated at 6 MV with IMRT using seven beam angles. They were treated with a Varian CL21EX linear accelerator fitted with a Varian Millennium 120 leaf collimator (Varian Medical Systems, Palo Alto, CA). The prescribed dose to the nodal region planning target volume (PTV) was 63 Gy for patient 1 and 55 Gy for patient 2. Both patients were treated concurrently with cisplatin chemotherapy given on days 1, 22, and 43. Each patient had two plans and two CT datasets. For patient 1 (shrinking node) the second plan began on fraction 18. For patient 2 (weight loss and displaced node) the second plan began on fraction 21. The analysis for each day of US imaging is based on the relevant CT scan and treatment plan. Any differences in isocentre set-ups have been taken into account when comparing the changing geometry of the node.

At the time of treatment planning, the patients were imaged in the CT simulation room in the same position as for treatment. They were immobilized with a thermoplastic mask and a standard head rest. During the course of treatment delivery, the patient and mask were aligned on the treatment couch with the room lasers and a portal image was acquired to correct for cervical vertebrae bony anatomy misalignment. After treatment, US scans were acquired in the treatment position. The mask was removed and non-permanent marks were made on the patient's skin at the position of the lasers. These daily marks allowed the technician to check if the patient moved during the scan. Different methods to keep the patient from moving were considered, such as bite blocks, but it was found that daily marks were sufficient to monitor movement and realign the neck. Transverse scans were performed along the sternocleidomastoid muscle with an anterior rotation near the clavicle. The images were obtained with an average

frame rate of twenty frames per second resulting in approximately one hundred and twenty 2D serial slices, however the area of interest for contouring was only a small group of these slices while the rest served to help localize the region of interest. The semi-automatic segmentation methods provided by the manufacturer make use of an atlas for a given organ (prostate, bladder, GYN), and are not ideal for our organ of interest. For this reason a single sonographer manually drew contours of individual nodes on the US images using the manufacturer's software offline.

6.3.3 Dose calculations

The EGSnrcmp/BEAMnrc [22] MC code was used to model the linear accelerator and beam parameters for each treatment plan. MC techniques can properly account for heterogeneities and irregular surfaces in the head and neck region, and accurately model the treatment beam geometry [23]. The treatment unit geometry and multileaf collimator component module have been previously validated at our institution demonstrating that IMRT MC simulations agree with dose measurements within 1% [24]. The fast MC code XVMC was used for dose calculations [25]. The dose distribution from each beam was calculated based on inhomogeneous CT voxel material and density assignments. The maximum statistical uncertainty was 1.7% of the maximum dose in each dose matrix. The voxel dimensions for all dose calculations and analyses were 0.234 cm anterior/posterior and right/left, and 0.5 cm superior/inferior. It is recognized that 0.5 cm slice spacing may introduce registration and volume averaging errors. However, the US system does not track voxels but overlays (fuses) images by interpolating the US images, which have greater superior/inferior resolution, to the position of each CT slice. Therefore image fusion is only as good as the room calibration. All nodal volume measurements were based on the US datasets. The US contours were exported in DICOM format to in-house software [26] developed in the MATLAB (The MathWorks, Natick, MA) environment for dosimetric analysis. The software also read in the CT images and CT contours, and the MC dose distribution. The US contours are compared to the physician drawn CT planning PTV contour.

In order to more closely assess the dose distribution in changing anatomy, the distribution on a simplified digital homogenous water phantom was simulated for various geometries. The phantom was designed to be a 15 cm long cylinder. A spherical contour imitating the shape and position of a lymph node was defined. MC simulations of the dose to the contour, using patient 1 and 2 beam geometries, were performed under situations that mimicked the changes seen in the patients in this study: a) the contour ranged in volume from 3.2 - 0.3 cm^3;

b) the diameter of the phantom ranged from 15.6-13 cm; and c) the contour was shifted away from the phantom surface in 2 mm increments.

6.4 Results

Figure 6.1 shows a) a CT image, b) an US image, and c) a CT/US fusion image for a patient. The crosshairs represent the isocentre and the diagonal line measures 49.4 mm from the isocentre to the skin surface. The same structures are visible on both imaging modalities. The fusion shows coincident skin surfaces within 1 mm (without the mask) and internal structure boundary alignment.

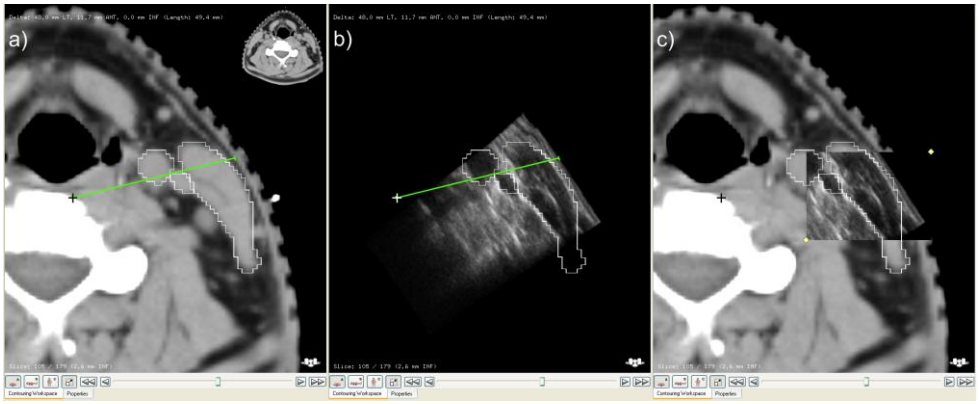

FIG. 6.1 Multimodality images of a patient with a) computed tomography (CT), b) ultrasound (US), c) CT/US fusion. The crosshairs represent the isocentre and the diagonal line measures 49.4 mm from the isocentre to the skin surface.

The data for the patients are reported in Tables 6.1 and 6.2. Each row represents the node that was imaged and contoured for the specified fraction. The dose statistics reported are the range, mean, standard deviation (SD), and dose to at least 95% of the volume (D95). Dose statistics to the nodal region PTV structures are also reported for comparison. Figure 6.2 displays the nodal geometrical changes with respect to the dose distribution from plan 1 for a) patient 1 and b) patient 2.

TABLE 6.1 Node statistics for patient 1. The first 4 rows represent a node that was contoured for the specified fraction, and the last two rows are the nodal region PTV contours for the specified treatment plan. Plan 1 was delivered for fractions 1-17 with a prescribed dose of 175 cGy per fraction, and plan 2 for fractions 18-33 with a prescribed dose of 210 cGy per fraction.

Patient 1 (shrinking node)				
Fraction	Volume (cm^3)	Dose range (cGy)	Mean dose ± SD (cGy)	D95 (cGy)
Node fx 1 (plan 1)	2.9	173 - 200	185 ± 6	175
Node fx 5 (plan 1)	2.8	174 - 195	185 ± 5	175
Node fx 17 (plan 1)	1.4	175 - 195	183 ± 5	177
Node fx 33 (plan 2)	0.5	70 - 228	184 ± 57	71
PTV Plan 1	341	163 - 220	184 ± 7	174
PTV Plan 2	359	182 - 258	223 ± 7	212

Abbreviations: SD = standard deviation, D95 = dose covering at least 95% of the volume.

TABLE 6.2 Node statistics for patient 2. The first 6 rows represent a node that was contoured for the specified fraction and the last two rows are the nodal region PTV contours for the specified treatment plan. Plan 1 was delivered for fractions 1-28 with a prescribed dose of 154 cGy per fraction, and plan 2 for fractions 29-35 with a prescribed dose of 171 cGy per fraction.

Patient 2 (weight loss and displaced node)				
Fraction	Distance from fx 1 (cm)	Dose range (cGy)	Mean dose ± SD (cGy)	D95 (cGy)
Node fx 1 (plan 1)	-	152 - 177	168 ± 7	153
Node fx 5 (plan 1)	0.5	144 - 167	156 ± 8	144
Node fx 8 (plan 1)	1.3	146 - 149	148 ± 2	146
Node fx 10 (plan 1)	0.8	146 - 164	154 ± 5	146
Node fx 13 (plan 1)	0.4	152 - 172	162 ± 7	153
Node fx 29 (plan 2)	0.4	176 - 185	182 ± 4	176
PTV Plan 1	-	116 - 250	176 ± 33	132
PTV Plan 2	-	120 - 249	197 ± 20	161

Abbreviations: SD = standard deviation, D95 = dose covering at least 95% of the volume.

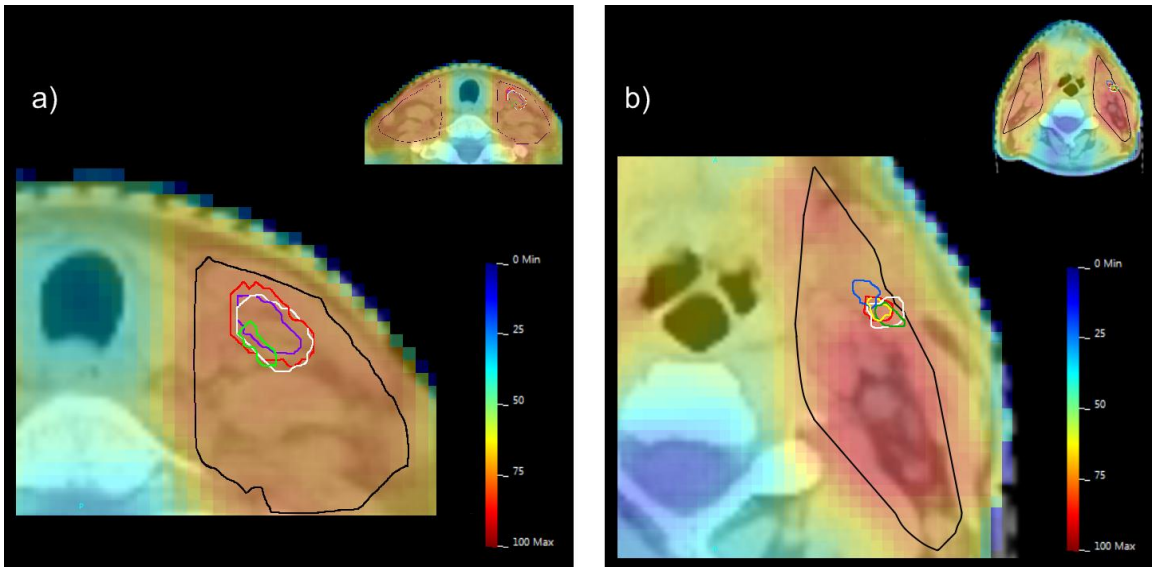

FIG. 6.2 Interfraction ultrasound nodal contours overlaid on the dose distribution from plan 1 for a) patient 1 (fraction 1 in red, fraction 5 in white, fraction 17 in blue, and fraction 33 in green), and b) patient 2 (fraction 1 in red, fraction 5 in white, fraction 8 in blue, fraction 10 in green, fraction 13 in yellow, and fraction 29 is not visible on this slice). The planning target volume contour is in black.

6.4.1 Patient 1: shrinking node

Data for patient 1 was acquired immediately after the delivery of fractions 1, 5, 17, and 33. The nodal volume reduction to 48% of the initial size after twenty-two days from the start of treatment (fraction 1-17) is in accordance with other studies [27,28]. As can be seen in Fig 6.3a, the node shows an almost concentric reduction in size.

The dose statistics for patient 1 during plan 1 remained essentially the same and similar to that prescribed for the nodal region PTV. The prescribed dose to the nodal region was 175 cGy per fraction for fractions 1-17 and 210 cGy per fraction for fractions 18-33. The MC calculated mean fractional dose to the node through plan 2 was constant, but the increase in range from 27 cGy for fraction 1 to 157 cGy from fraction 33 indicate that during plan 2 the node was in a high dose gradient region. Figure 6.3 shows axial, sagittal, and coronal views of the dose distribution for plan 2 and demonstrates the position of the node outside the PTV. Figure 6.4 plots dose volume histograms (DVH) for a) the patient and b) phantom simulations for one fraction of plan

1. For the phantom simulations the sphere was located at roughly the same distance from the phantom surface as the patient's node was from the skin surface. Due to the small size of the node at fraction 33, the DVH drops to 76 cGy for 82% of the volume, so that D95 is much smaller compared to previous fractions, even though the prescribed dose was larger. This fraction only encompassed 19 voxels compared to 104 voxels at fraction 1. Confirming the patient dose calculations, D95 to the phantom spheres were around 185 cGy.

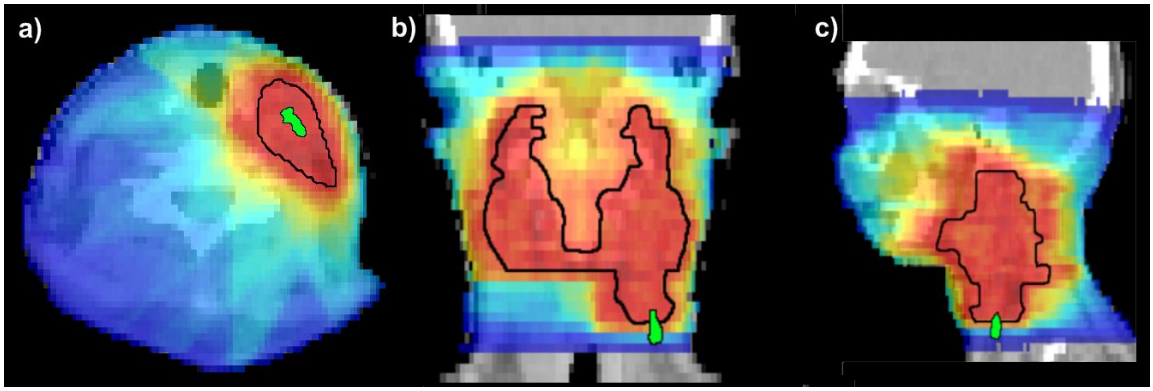

FIG. 6.3 Plan 2 dose distributions for patient 1 in the a) axial, b) sagittal, c) coronal planes for patient 1. The nodal region planning target volume (PTV) is outlined in black and the node contoured after fraction 33 is shown in bright green at the edge of the PTV.

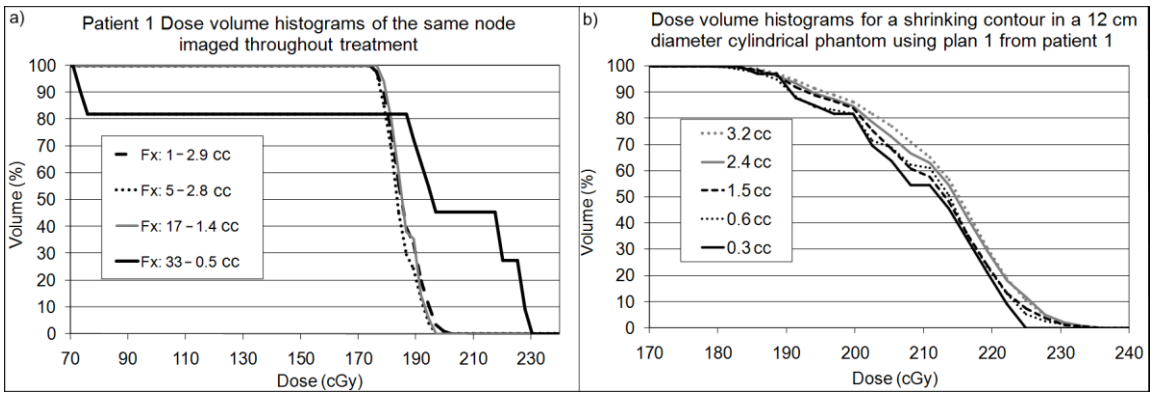

FIG. 6.4 a) Dose volume histograms of node contours for patient 1. The prescribed dose to the nodal region was 175 cGy per fraction for fractions 1-17 and 210 cGy per fraction for fractions 18-33. b) Dose volume histograms of a concentrically shrinking sphere of plan 1 from patient 1 on a digital phantom.

6.4.2 Patient 2: weight loss and displaced node

For patient 2 (weight loss) images were acquired immediately after the delivery of fractions 1, 5, 8, 10, 13, and 29. The external geometry of patient 2 changed substantially during the course of treatment. Figure 6.5a (plan 1) was acquired nineteen days before the start of treatment and Figure 6.5b (plan 2) was acquired twenty-eight days after the start of treatment. The change in surface area on this slice, as defined by the external contour, is a reduction of 21%. The patient was reported to have lost approximately 9 kg, a weight loss of 10%.

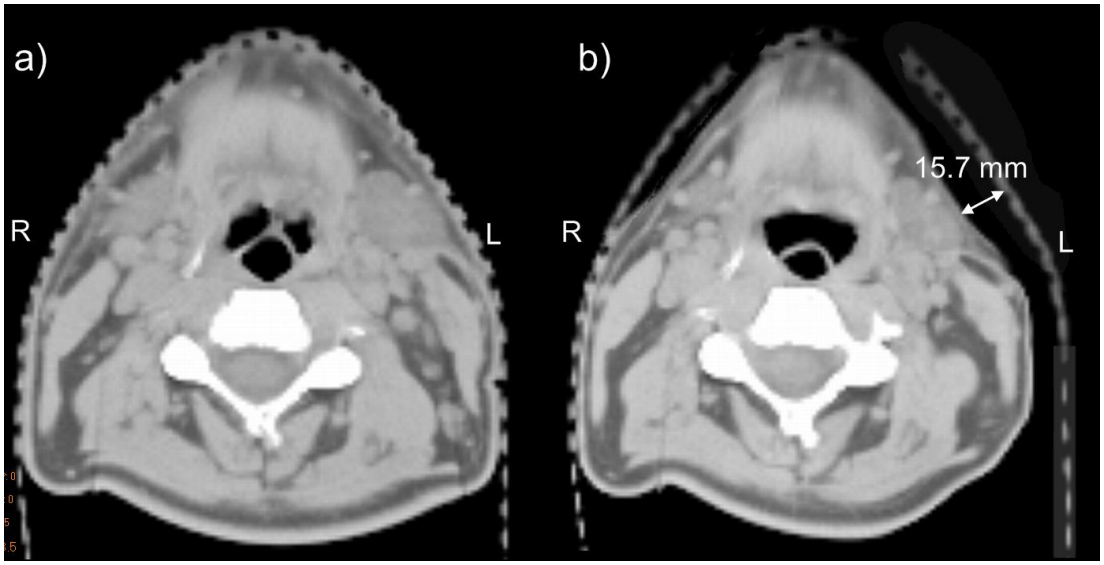

FIG. 6.5 CT images showing the shrinking external contour of patient 2; a) acquired nineteen days before the start of treatment, b) acquired twenty-eight days after the start of treatment.

The magnitude of the difference in node position from fraction 1 is listed in Table 6.2. The node's centre of mass moved up to 1.3 cm away resulting in 12% less dose coverage. The mean 3D nodal shift of 0.7 cm is similar to other reported cervical node displacements [4,29].

Patient 2 was replanned at fraction 21, which reduced dose range in the node from about 20 cGy to 9 cGy. DVHs for all patient 2 contours are plotted in Fig. 6.6a. The curves are relatively vertical due to the small size of the node. The DVHs demonstrate that for plan 1 the delivered dose varied, did not follow a trend, and did not follow the prescribed dose of 154 cGy per fraction.

Figure 6.6 also shows the results from two phantom simulations using plan 1 from patient 2, illustrating the consequence of changing patient geometry in IMRT fields. Figure 6.6b shows the degradation in DVHs to a 1.8 cm^3 contour as the diameter of the phantom decreased from 15.4 cm to 13 cm. A 6 mm diameter difference changed D95 and D50 to a 0.2 cm^3 structure by 2.1% and 3.4%, respectively. Figure 6.6c shows the change in DVHs when the contour's position changed by 12 mm from the surface. Moving from inside the phantom toward the surface, the mean dose and D95 decreased by 4% and 42 cGy, respectively.

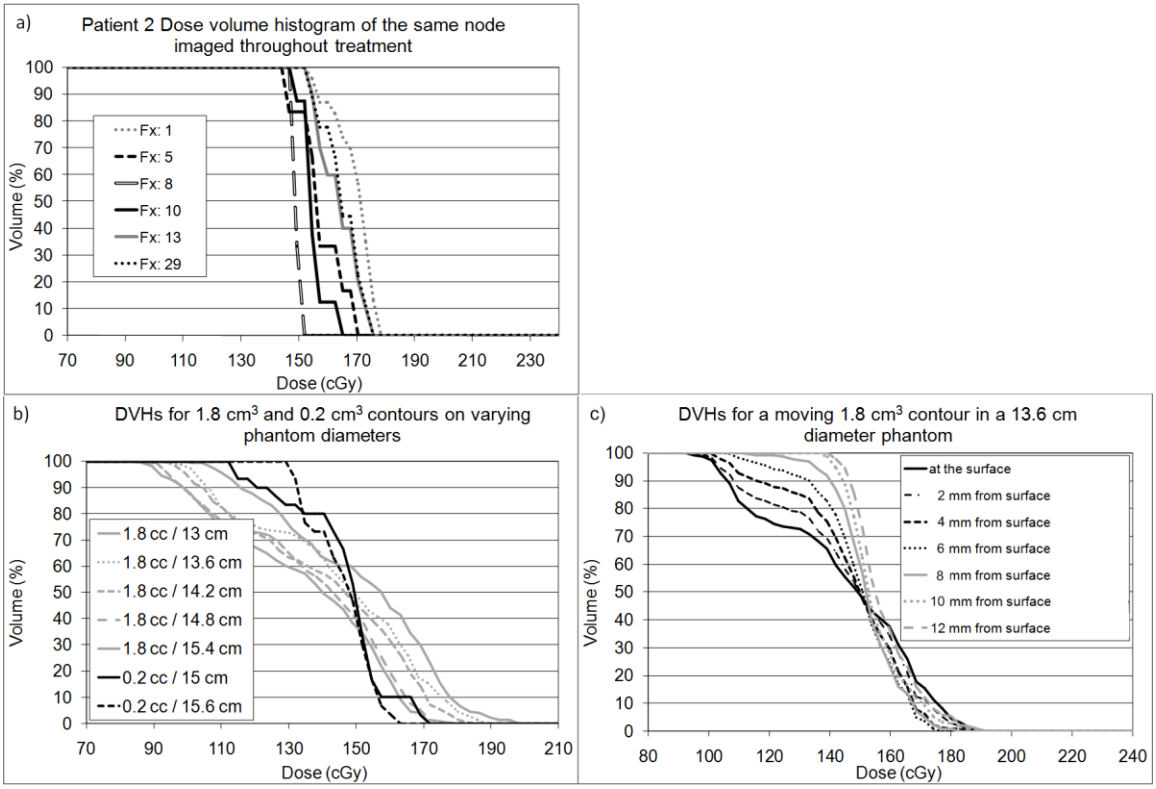

FIG. 6.6 a) Dose volume histograms of node contours for patient 2. The prescribed dose to the nodal region was 154 cGy per fraction for fractions 1-28 and 171 cGy per fraction for fractions 29-35. b) Simulated phantom and contour geometries with plan 1 from patient 2 using contours on varying phantom diameters, and c) varying contour positions on the same sized phantom.

6.5 Discussion

For IMRT targets in heterogeneous dose regions that change geometry in time frames relevant to radiation therapy, patient realignment may not be the best solution. Realigning the patient will reposition the beams with respect to not only the external surface contour, but also internal tissue boundaries. In Fig. 6.4 the node is located in a steep dose gradient of 76 cGy over 5 mm. It would require a 1 cm shift to completely locate the node inside the PTV, which is greater than many IMRT margins [30]. Shifting the patient will change the conformality of the plan by an unknown amount, especially when many gantry angles are used. Moreover, it is possible that one region of the PTV target is more susceptible to geometric changes than other regions, as Fig. 6.5 shows an asymmetric change in the external surface, so that realignment corrections may detrimentally impact the dose in other target regions.

For patients immobilized with thermoplastic masks, residual motion and positioning errors can still occur [30]. The range of motion of the centre of mass of the node can be substantial. An average 3D displacement of 0.7 cm, after thermoplastic mask and vertebrae alignment, is almost three times greater than reported systematic positioning errors using portal imaging (1.6-4.6 mm) [31], tomotherapy megavoltage CT (1.6-2.6 mm) [32], and kilovoltage cone beam CT (1.4-1.8 mm) [33]. Therefore tissue deformation cannot always be accounted for with PTV margins without reducing the benefit of IMRT conformality.

Image guidance that shows correct patient alignment is also not always a guarantee that the dose will be delivered as prescribed. It has been reported that aligning the spinal cord to match reference imaging did not correctly align level 1 lymph nodes. This resulted in a reduction of 2-6 Gy of the equivalent uniform dose to the nodes over the whole treatment [7]. Patient weight loss may also cause incorrect dose delivery when bony anatomy is aligned. For patient 2, as the skin surface moved toward the isocentre and the node shifted its position on a daily basis, the node repositioned closer to the surface as treatment progressed — an effect that cannot be corrected for with patient realignment. This is a concern for superficial targets because skin sparing demands a lower dose. Another study evaluated the impact of tissue loss to 45% of the PTV and found that even though target coverage was maintained, the dose to the spinal cord varied by up to 10% during treatment [34].

This case study illustrates some of the geometrical changes that can alter the expected delivered dose. It is recognized that only the motion of the node was considered, as it is understood that in the absence of daily CT images the true delivered dose cannot be calculated.

However, an estimate was made about dose coverage to displaced US contours on the same CT. The patient study and phantom simulations provide an idea of the magnitude of change in dose coverage for different scenarios. Replanning would provide better target coverage as shown in plan 2 for patient 2. Yet the imaging modality must be able to distinguish between different tissues in the area of interest. In the neck region, superficial targets (< 5 cm deep) are ideal candidates for US imaging, and new 3D systems promise to be more accurate than older technology [35,36].

6.6 Conclusion

An uncertainty in the delivered dose to lymph nodes in the head and neck region always exists because anatomic changes are unpredictable and patient specific. Current techniques to account for these changes are patient realignment under the treatment beams and/or replanning. Yet, the combination of anatomic changes in this region, and IMRT techniques, may better benefit with replanning. For soft tissue targets that are difficult to see with x-rays, US imaging may prove to be a viable, artifact free, and nonionizing option for image guidance, and can be used as a trigger to determine if and when replanning is necessary.

6.7 Acknowledgements

Geralyn Ochab and Resonant Medical are gratefully thanked for contouring the lymph nodes. Contributions from Clarisse Mark and Aichu Chang are also acknowledged. This work was supported by the Canada Foundation for Innovation New Opportunities Program (CFI grant #10036). FV was supported by the Fonds de la Recherche en Santé Québec.

6.8 Afterward

Ultrasound imaging in the neck region provides valuable information on anatomy that is known to respond to radiation and undergo geometric changes. We measured motion up to 1.3 cm and volume shrinkage down to 17% of the initial size. We demonstrated that these changes are dosimetrically relevant, and may lead to an under dose of tissue that is known to be a site of recurrent cancer thereby providing new information for the radiation therapy community. Unlike prostate cancer, where it has been shown that patient realignment does not substantially alter the delivered dose, patient realignment to account for cervical node changes may increase coverage in one area of the target while reduce it in another when IMRT techniques are used. Critical structures in the head region may also be adversely affected. Instead, ultrasound image guidance is proposed as a monitoring device and a trigger to determine when adaptive replanning

is necessary. With adequate training and experience, ultrasound imaging of the neck region could prove beneficial.

6.9 References

[1] Yorke ED, Keall P, and Verhaegen F. Anniversary paper: Role of medical physicists and the AAPM in improving geometric aspects of treatment accuracy and precision. *Med Phys* 2008; 35: 828-839

[2] Mageras GS and Mechalakos J. Planning in the IGRT context: Closing the loop. *Semin Radiat Oncol* 2007; 17: 268-277

[3] Dawson L and Sharpe M. Image-guided radiotherapy: rationale, benefits, limitations. *Lancet Oncol* 2006; 7: 848-858

[4] Huang F, Vakilian S,Parker W, and Shenouda G. Parameters for rescanning during radiotherapy for head and neck cancer [Abstract]. *Radiother Oncol* 2008; 88: S56

[5] Ruchala K, Olivera G, Lu W, et al. A dose-guided adaptive therapy process for treatment evaluation and correction. *Med Phys* 2003; 33: 1988

[6] Aubry, Cheung J, Yom S, et al. Calculation of the dose of the day using megavoltage cone-beam CT [Abstract]. *Med Phys* 2008; 35: 2914

[7] Chase D, Ramsey C, Mahan S, Seibert R. Image-guided adaptive radiation therapy for improving level I lymph node coverage for head and neck cases. *Med Phys* 2005; 32: 1946-1947

[8] Grégoire V, Coche E, Cosnard G, Hamoir M, and Reychler H. Selection and delineation of lymph node target volumes in head and neck conformal radiotherapy. Proposal for standardizing terminology and procedure based on the surgical experience. *Radiother Oncol* 2000; 56: 135-15

[9] Ridge JA, Glisson BS, Horwitz EM, and Meyers MO. Head and neck tumors. In: Pazdur R, Coia LR, Hoskins WJ, Wagman LD, editors. Cancer management: A multidisciplinary approach. Manhasset, NY: The Oncology Group, CMP Medica. 2003; 39-86

[10] Huguenin PU, Taussky D, Moe K, et al. Quality of life in patients cured from a carcinoma of the head and neck by radiotherapy: The importance of the target volume. *Int J Radiat Oncol Biol Phys* 1999; 45: 47-52

[11] Bruneton JN, Matter D, Lassau N, and Dassonville O. Lymph Nodes. In: Bruneton JN, editor. Applications of sonography in head and neck pathology. Germany: Springer-Verlag. 2002; 137-163

[12] Roper B, Nuse N, Busch R, Simmermann FB, Nahrig J, and Molls M. Tissue characterization of locoregionally advanced head-and-neck squamous cell carcinoma (HNSCC) using quantified ultrasonography: A prospective phase II study on prognostic relevance. *Radiother Oncol* 2007; 85: 48-57

[13] Sumi M, Ohki M, and Nakamura T. Comparison of sonography and CT for differentiating benign from malignant cervical lymph nodes in patients with squamous cell carcinoma of the head and neck. *AJR Am J Roentgenol* 2001; 176: 1019-1024

[14] Mende UH, Dinkel J, and Mende MB. Lymph node imaging: Ultrasound, CT or MRI? *Ultrasound Med Biol* 2006; 32: P14

[15] Hajek PC, Salomonowitz E, Turk R, Tscholakoff D, Kumpan W, and Czembirek H. Lymph nodes of the neck: Evaluation with US. *Radiology* 1986; 158: 739-742

[16] Nga WT, Lee AWM, Kan WK, et al. N-staging by magnetic resonance imaging for patients with nasopharyngeal carcinoma: Pattern of nodal involvement by radiological levels. *Radiother Oncol* 2007; 82: 70-75

[17] Lee K, Kam K, and King A. MRI of nasopharygneal carcinoma (NPC) patients in radiation treatment position to improve the delineation of the tumour and cervical lymph nodes [Abstract]. *Med Phys* 2007; 34: 2396

[18] Zhu S and Hu B. The current status of the delineation and determination of the targets and the radiation protocols for nasopharyngeal cancer with intensity-modulated radiotherapy. *Chinese J Clin Oncol* 2007; 4: 360-366

[19] Lattanzi J, McNeeley S, Hanlon A, et al. Ultrasound-based stereotactic guidance of precision conformal external beam radiation therapy in clinically localized prostate cancer. *Urology* 2000; 55: 73-78.

[20] Johnston H, Hilts M, Beckham W, and Berthelet E. 3D ultrasound for prostate localization in radiation therapy: A comparison with implanted fiducial markers. *Med Phys* 2008; 32: 2403-2413

[21] Fraser D, Fava P, Cury F, Vuong T, and Falco T, Verhaegen F. Evaluation of a prototype 3D ultrasound system for multimodality imaging of cervical nodes for adaptive radiation therapy. *Proc. of SPIE* 2007; 6509: 65090Y

[22] Rogers DWO, Faddegon BA, Ding GX, Ma CM, We J, and Mackie TR. BEAM: a Monte Carlo code to simulate radiotherapy treatment units. *Med Phys* 1995; 22: 503-524

[23] Mihaylov IB, Lerma FA, Fatyga M, and Siebers JV. Quantification of the impact of MLC modeling and tissue heterogeneities on dynamic IMRT dose calculations. *Med Phys* 2007; 34: 1244-1252

[24] Heath E and Seuntjens J. Development and validation of a BEAMnrc component module for accurate Monte Carlo modelling of the Varian dynamic Millennium multileaf collimator. *Phys Med Biol* 2003; 48: 4045-4063

[25] Kawrakow I and Fippel M. Investigation of variance reduction techniques for Monte Carlo photon dose calculation using XVMC. *Phys Med Biol* 2000; 45: 2163-2183

[26] Poon E, Le Y, Williamson JF, and Verhaegen F. BrachyGUI: An adjunct to an accelerated Monte Carlo photon transport code for patient-specific brachytherapy dose calculations and analysis. *J. Phys.: Conf. Ser.* 2008; 102 012018

[27] Schafer CB, Bartzsh OM, Feldmann HF, Molls M, and Allgauer M. Ultrasound volumetry of cervical lymph nodes during radiotherapy as a method of therapy monitoring. *Ultraschall Med* 1996; 17: 289-294

[28] Liszka G, Thalacker U, Somogyi A, and Németh G. Volume changes to the neck lymph node metastases in head-neck tumors: The evaluation of radiotherapeutic treatment success. *Strahlenther Onkol* 1997; 73: 428-430

[29] Barker JL, Garden AS, Ang KK, et al. Quantification of volumetric and geometric changes occurring during fractionated radiotherapy for head and neck cancer using an integrated

CT/linear accelerator system. *Int J Radiat Oncol Biol Phys* 2004; 59: 960- 970

[30] Vaandering A, Lee JA, Renard L, and Grégoire V. Evaluation of MVCT protocols for brain and head and neck tumor patients treated with helical tomotherapy. *Radiother Oncol* 2009; 93: 50-56

[31] Hurkmans CW, Remeijer P, Lebesque JV, and Mijnheer BJ. Set-up verification using portal imaging: Review of current clinical practice. *Radiother Oncol* 2001; 58: 105-120

[32] Schubert L, Westerly D, Tomé W, et al. A comprehensive assessment by tumor site of patient set-up using daily MVCT imaging from more than 3,800 helical tomotherapy treatments. *Int J Radiat Oncol Biol Phys* 2009; 73: 1260-1269

[33] Den RB, Doemer A, Kubicek G, et al. Daily image guidance with cone-beam computed tomography for head-and-neck cancer intensity-modulated radiotherapy: A prospective study. *Int J Radiat Oncol Biol Phys* 2009 Jun 17 [Epub ahead of print]

[34] Mechalakos J, Lee N, Hunt M, Clifton Ling C, and Amols HI. The effect of significant tumor reduction on the dose distribution in intensity modulated radiation therapy for head-and-neck cancer: A case study. *Medical Dosim* 2009; 34: 250-255

[35] Cury FL, Shenouda G, Souhami L, et al. Ultrasound-based image guided radiotherapy for prostate cancer-comparison of cross-modality and intramodality methods for daily localization during external beam radiotherapy. *Int J Radiat Oncol Biol Phys* 2006; 66: 1562-1567

[36] van Herk M. Different styles of image-guided radiotherapy. *Semin Radiat Oncol* 2007; 17: 258-267

CHAPTER 7

Comparison of conventional and Monte Carlo dose calculations for prostate treatments

In this chapter we present a manuscript published in the *Journal of Physics: Conference Series* from the Third McGill International Workshop: Monte Carlo Techniques in Radiotherapy Delivery and Verification. The purpose of the study was to compare different dose calculation algorithms for prostate cancer and to determine if time-consuming Monte Carlo methods were justified for this treatment site. In general, implementation of MC dose calculations have had the most success in heterogeneous cancer sites that contain tissue with a wide range of atomic numbers, such as the head and neck region which contains soft tissue, bone matter, and air cavities. Intuitively, the pelvic region would not benefit greatly from heterogeneity corrections, but in some cases the femoral heads may be directly in the treatment beam and metal alloy hip prostheses may be present. Moreover, the convex shape of the prostate lends itself to treatment fields defined by multileaf collimators, which are often inadequately modeled with analytical algorithms.

Dose calculation accuracy at the treatment planning stage becomes increasingly important when interfraction motion is considered (Chapter 8). Initial dose calculation errors may be systematically carried through further dose calculations, or more crucially their impact may be unknown in changing anatomy. This study sets the baseline for Chapter 8, and is widely applicable in radiation oncology as prostate cancer is the most commonly diagnosed cancer in Canadian men, with an estimated 25 500 new cases in 2009[*].

[*] Canadian Cancer Society's Steering Committee. Canadian Cancer Statistics 2009. (Toronto: Canadian Cancer society, 2009)

Title: Comparison of conventional and Monte Carlo dose calculations for prostate treatments

Authors: Fraser D, Mark C, Cury F, Chang A, and Verhaegen F

Published in the Journal of Physics: Conference Series, Volume 102 (2008) 012010
doi: 10.1088/1742-6596/102/1/012010

7.1 Abstract

Monte Carlo (MC) calculations are rapidly finding their place in clinical dose assessments. We investigated conformal prostate dose distributions as calculated by MC, and compared them to several analytical dose calculations. The treatment distributions for twenty prostate cancer patients, treated with 18 MV 3D conformal radiation therapy, were retrospectively assessed. The BEAMnrc code based on EGSnrc was used to model the beam from which phase space files were used as input into the XVMC algorithm. This was compared to conventional treatment planning system calculations (CADPLAN, Varian Oncology Systems, Palo Alto, CA) with and without inhomogeneity corrections. Results indicate that the CADPLAN generalized Batho Power Law, modified Batho Power Law, and equivalent tissue-air ratio methods contain inaccuracies in calculated dose to 95% of the prostate planning target volume of 3.5%, 3.3%, and 2.9%, respectively. The greatest discrepancies in the organs at risk were seen in the bladder where the inhomogeneity correction methods all predicted that 50% of the prescribed dose covered an average of 8.2% more of the bladder volume than that predicted from the MC calculation. Water equivalent MC and water equivalent CADPLAN calculations revealed important discrepancies on the same order as those between heterogeneous MC and heterogeneous CADPLAN calculations. The data indicate that the effect of inhomogeneities is greater in the target volume than the organs at risk, and that accurately modeling the dose deposition process is important for each patient geometry, and may have a greater impact on the dose distribution in the prostate region than correcting an analytical algorithm for the presence of inhomogeneities.

7.2 Introduction

The trend towards dose escalation in smaller target volumes has increased the drive for greater accuracy in dose calculations. Dose coverage is affected by tissue inhomogeneity not only in the planning target volume (PTV) but also in nearby organs at risk (OAR). The conventional method to predict the dose to a patient is to assume a homogeneous water medium. Inhomogeneous objects are then accounted for analytically by treating inhomogeneities as a

perturbation of the dose under the same beam conditions in a homogeneous water phantom. More recently, particle transport methods have been incorporated into treatment planning systems (TPS) either explicitly, or through convolution kernels. Accounting for tissue differences with improved algorithms reduces the uncertainty in absolute dose.

In this study dose calculations with four analytical algorithms from a commercial TPS, and two Monte Carlo (MC) methods, are compared for twenty external beam 3D conformal radiation therapy (3D-CRT) treatment plans for prostate cancer.

7.3 Methods

7.3.1 Patient Planning

3D-CRT treatment plans for twenty prostate cancer patients were generated using an 18 MV coplanar five field beam geometry: one anterior field (gantry at 0°); two parallel opposed lateral fields (gantry at 90°, 270°); and two posterior oblique fields (gantry at 110°, 250°). Each field was shaped with a 52 leaf collimator, and depending on the patient, the use of 15°-30° physical wedges in the oblique fields were used to protect the femoral heads. The patient model was determined from CT images, and the plans were manually optimized with an analytical algorithm based on a water equivalent patient without heterogeneities. The PTV was defined from the CT image as the prostate volume plus a 7 mm margin.

7.3.2 Retrospective Dose Calculations

Analytical dose calculations were performed with CADPLAN v6.0 (Varian Medical Systems Inc., Palo Alto, CA). CADPLAN's double pencil beam model (PB-wat), derived from broad beam data, is used to calculate dose distributions in water equivalent material. Inhomogeneities are considered via three common correction-based methods: the Batho Power Law (Batho); the modified Batho Power Law (MBatho); and the equivalent tissue-air ratio (ETAR). Batho is an empirical correction factor method that uses tissue-maximum ratios (TMR) for high energy beams, raised to a power that depends on the medium's electron density relative to water. It was originally developed for dose calculations in water below a single slab of lung tissue [1]. MBatho differs in its definition of depth. In high energy photon beams the build-up region can be several centimeters thick in which the TMR values are not valid. The modified method uses only the descending part of the TMR curves by adding the depth of maximum dose to the depth used in the previous generalized Batho method. ETAR scales the depth and radius of the TAR(z, A) derived in a unit density water medium according to the relative effective

electron density (along the primary ray path) of the inhomogeneous medium [2]. The treatment plan (beam geometry and monitor units) was developed for the homogeneous water equivalent material scenario, PB-wat. The second, third, and fourth calculations multiply the dose value from the PB-wat method with an inhomogeneity correction factor determined using the Batho, MBatho, and ETAR methods, respectively.

Monte Carlo radiation transport techniques use numerical methods to model the physical processes which govern interactions between radiation and their environment. These processes are described by probability distributions so that a first-principles approach is used. XVMC [3,4] is a fast 3D photon MC code based on the Voxel Monte Carlo [5] algorithm originally developed for electron beams. XVMC uses several simplifications and approximations to increase computational efficiency in the range of energies and materials encountered in radiation therapy. These include: (1) a fast electron transport algorithm and a fast ray tracing technique; and (2) the dose from low energy scattered photons and bremsstrahlung photons produced in the phantom matrix is estimated with a kerma approximation. The EGSnrc/BEAM [6] code was used to model a Clinac 2300 linear accelerator, and score phase space files for each beam in the treatment plan. The beam model used a 17.8 MeV electron pencil beam of radius 1.0 mm, and has previously been validated such that off axis ratios for a 10x10 cm^2 matched measurements at the depth of maximum dose and at 10 cm within 1% [7]. We also verified the beam model against the PB-wat algorithm for simple open field geometries, which only showed differences that were greater than the MC statistical error in the penumbra and build up regions. It is expected that the TPS' multileaf collimator model will further increase these differences with MC. The dose distribution for each beam was calculated with XVMC using a maximum statistical error of 2%, for an average simulation time of 60 minutes (five fields) on a single 2.7 GHz 64 bit AMD processor. XVMC distributions were calculated based on inhomogeneous CT voxel material and density assignments (XVMC-het), as well as assuming a homogeneous water equivalent patient (XVMC-wat). In-house software was used to calculate dose volume histograms for all dose calculations [8]. The absolute dose resulting from the XVMC simulations was calculated by relating the dose per incident particle to the dose per monitor unit (MU) from the linear accelerator calibration, and then multiplying by the number of MUs as specified in the plan. A MC simulation under calibration conditions (10x10 cm^2, 100 cm SSD, water phantom) was performed and the dose per incident particle at the depth of maximum dose was related to the calibration value of 1.00 cGy/MU in water. This approach ignores the effect of backscatter

towards the monitor ion chamber. However, it has been shown that for field sizes larger than 5x5 cm^2 such as the ones used in this research, this effect is negligible [9].

Analysis of twenty patients is performed with a comparison of dose-volume based indices. The dose (cGy) covering 95% of the PTV volume, $D_{95\%PTV}$, is used for the target, while in order to represent the shallow dose gradient regions in the OARs – rectum and bladder, the calculated doses are compared via the volume (cm^3) receiving 50% of the prescribed dose, $V_{50\%PD}$.

7.4 Results

Figure 7.1 is a graph of the difference in $D_{95\%PTV}$ between algorithms. The values are normalized to the prescribed dose (either 6600 cGy or 7200 cGy). The average and one sigma standard deviations of the differences are also indicated. The values of $\Delta D_{95\%PTV}$ calculated by CADPLAN are within 8.6% with an average value of 3.5%, and those calculated by XVMC-wat are within 2.4% with an average value of 1.7%. All calculations predicted a higher dose to the PTV than the full MC calculation that considered inhomogeneities. It has been shown that in cases where the electron density of an overlying inhomogeneous layer is greater than that of water the power-law method over estimates the dose [10]. Additionally, this method assumes semi-infinite slab geometry. In the treatment plans assessed, the two lateral and/or posterior oblique beams reach the PTV usually after passing through a portion of the femurs. These have finite dimension, are generally only partially in the field, and have a greater electron density than water. The Batho methods are therefore not ideally suited for this treatment plan geometry.

The average differences in $D_{95\%PTV}$ between PB-wat and Batho, MBatho, and ETAR are 0.9%, 1.1%, and 1.4%, respectively. The average difference in $D_{95\%PTV}$ between XVMC-wat and XVMC-het is 1.7%. The difference between analytical algorithms is of the same order as that between MC algorithms. CADPLAN's Batho algorithms average the electron density over each 1 cm interval between the dose point of interest and the source, thereby lowering the effective electron density of any bone intersecting the beam path. Similarly, the ETAR algorithm scales the depth by averaging the electron density along the volume elements in a direct path from the source to the point of interest, and scales the radius by multiplying the beam's equivalent circular radius by a weighted average of the electron density along that path. The weighting is determined from the difference between the scatter air ratio values at the point of interest and that at each point along the beam path. These methods do not incorporate inhomogeneities from adjacent horizontal volume elements, and reduce the effects of relatively small inhomogeneities in otherwise water-similar media. Figs 7.2a and 7.2b provide an example of one of the larger roles

inhomogeneities had on the PTV in our data set (patient 13). The difference in $D_{95\%PTV}$ between XVMC-het and XVMC-wat is 1.7%, and between MBatho and PB-wat is 1.0%. However, the MC data differs from the analytical algorithms by approximately 6% in the PTV. This substantial difference is seen in all organs for patient 13 in Fig. 7.2a, as well as in the PTV for all patients in Fig. 7.1. The maximum value of $\Delta D_{95\%PTV}$ for the analytical inhomogeneity corrections in Fig. 7.1 is 7.8% (Batho) with an average of 3.5% (Batho).

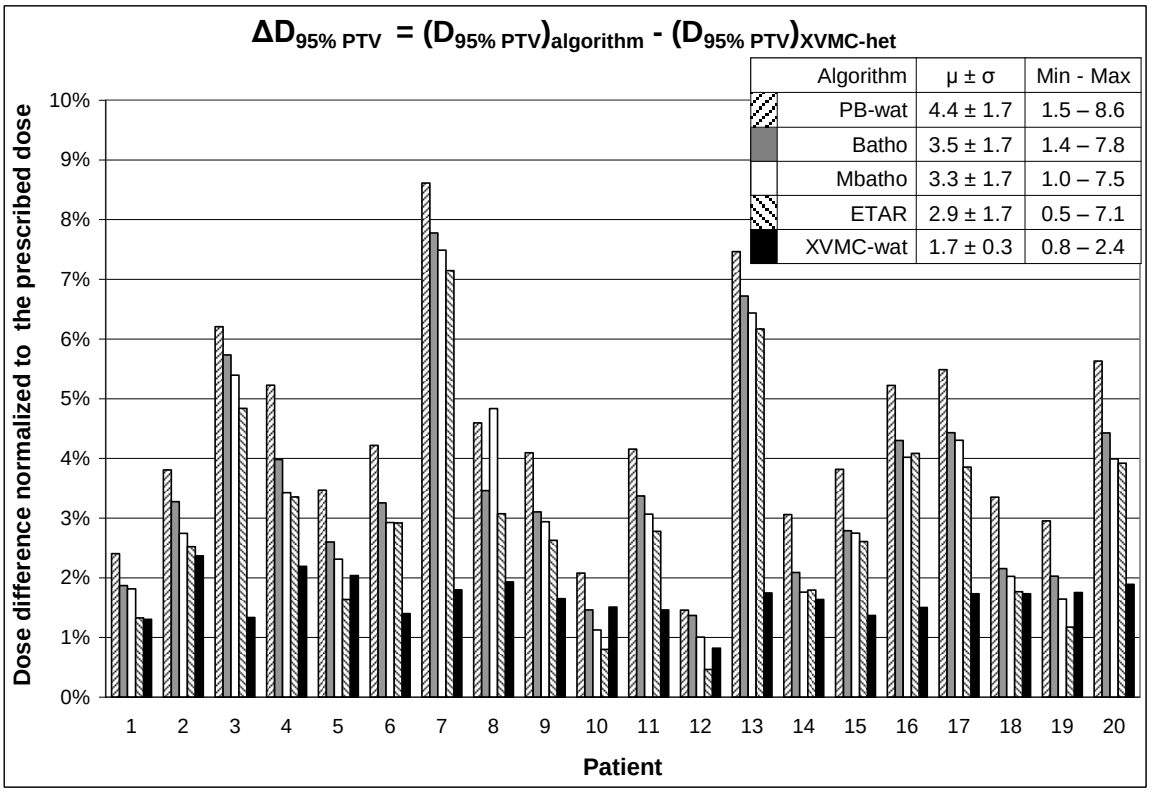

FIG. 7.1 Percentage difference in dose covering 95% of the PTV volume, $\Delta D_{95\%PTV}$, normalized to the prescribed dose.

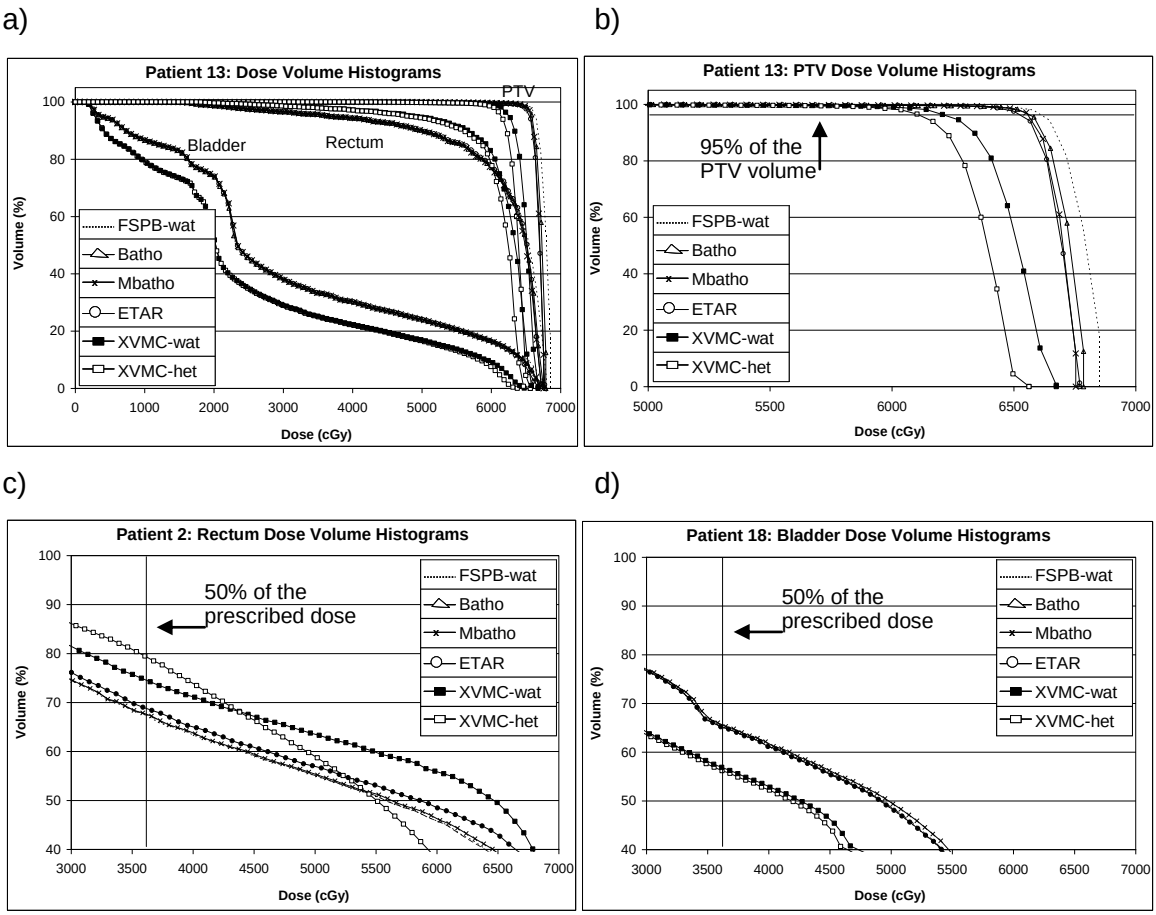

FIG. 7.2 Cumulative DVHs for a) all organs and b) the PTV for patient 13, c) the rectum for patient 2 where inhomogeneities had the largest impact on the rectum distribution, and d) the bladder for patient 18, which illustrates a typical case where the calculation method impacted the distribution.

Figures 7.3 and 7.4 are graphs of the difference between algorithms in $V_{50\%PD}$ for the rectum and bladder. The values are normalized to the total organ volume. The majority of $\Delta V_{50\%PD}$ for the rectum are negative, indicating that XVMC-het predicted dose coverage over a larger volume. For the bladder all $\Delta V_{50\%PD}$ are positive, indicating that XVMC-het predicted dose coverage over a smaller volume.

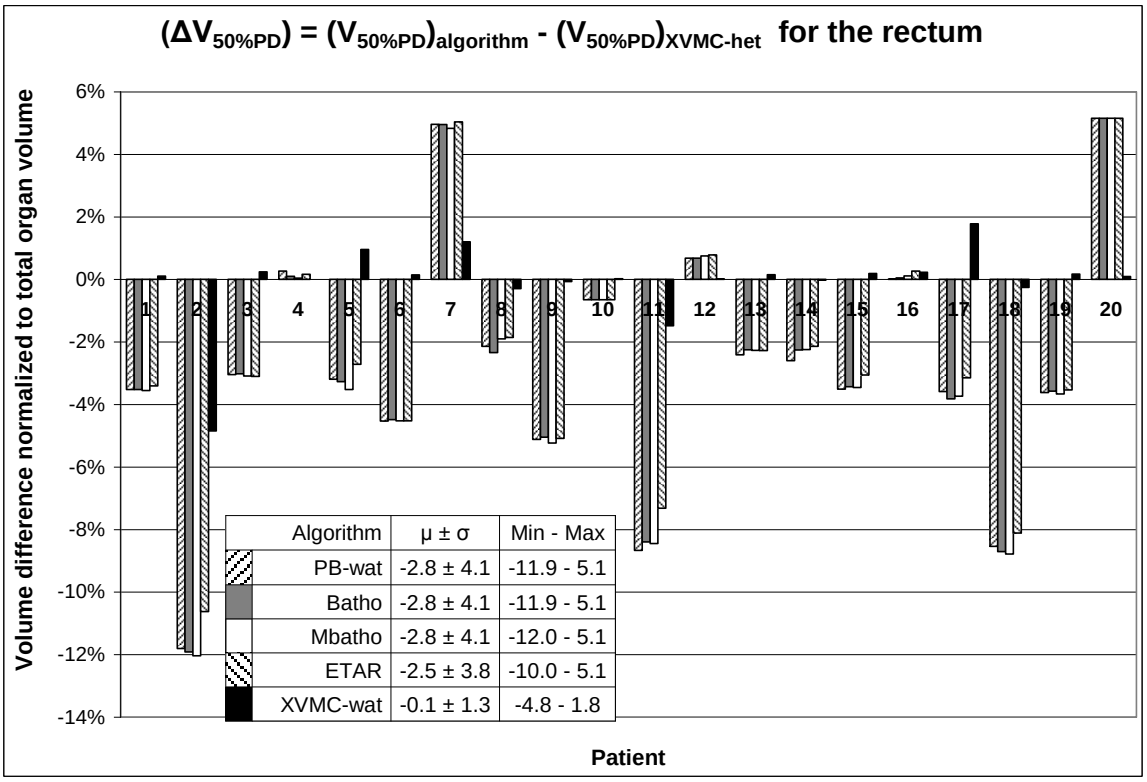

FIG. 7.3 Difference between rectum volumes contained within the 50% prescribed isodose line. The volumes are normalized to the total organ volume.

Among the four analytical calculations, the average and range of $\Delta V_{50\%PD}$ for each of the rectum and bladder separately are essentially the same. In MC simulations, the $\Delta V_{50\%PD}$ for XVMC-wat is generally very small and has an average value of -0.1% for the rectum and 0.4% for the bladder. These indicate that the effect of inhomogeneities on the dose to the rectum and bladder may be smaller than to the PTV. This may be explained from the inadequate lateral scattering model in the analytical calculations such that the dose to the rectum and bladder, which are tangential to four out of five beams, remain relatively the same. Similar results were found by Yang et al [11] for 10 MV photons in a coplanar geometry when comparing pencil beam homogeneous and inhomogeneous algorithms, and by du Plessis et al [12] where Batho and ETAR methods were accurate within 3% of MC simulations for a prostate model. Yang et al also found that MC and pencil beam algorithms predicted doses to the CTV within 3% of each other, which corresponds with the results in Fig. 7.1. Figure 7.2c graphs the cumulative DVH of the rectum for patient 2 (and shows $V_{50\%PD}$) who was an exception with a relatively large (-5.85%) discrepancy between XVMC-wat and XVMC-het. In the XVMC-wat simulation for this patient, the 50%

isodose line passes through the rectum, but the CT image showed that the rectum was filled with gas. Because the rectum lies in the descending portion of the depth dose curve, the presence of a gas cavity increases the penetration depth of the beam allowing for a greater rectum volume to be encompassed by the 50% isodose line in the XVMC-het simulation. Figure 7.2d graphs the cumulative DVH of the bladder for patient 18. This is a typical case in the data set demonstrating the small differences between homogeneous and inhomogeneous CADPLAN calculations, and the large differences between MC and analytical calculations.

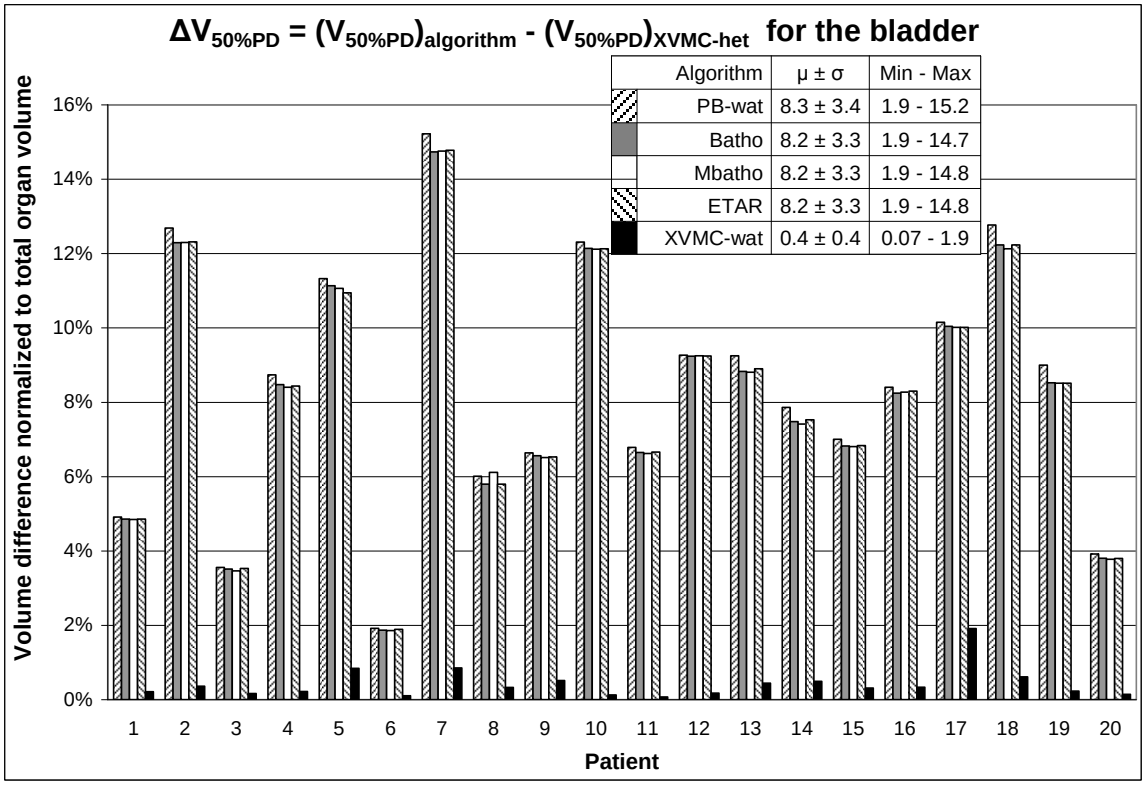

FIG. 7.4 Difference between bladder volumes contained within the 50% prescribed isodose line. The volumes are normalized to the total organ volume.

Prostate sites are similar to water due to the occurrence of mainly soft tissue, despite the presence of bone in the femoral heads. Although there is a small 1.7% difference in $D_{95\%PTV}$ for the PTV, and essentially no difference in $V_{50\%PD}$ for the OARs when inhomogeneities are considered, there is consistently a large difference between analytical and MC methods, indicating that the dose model has a greater impact than inhomogeneity corrections for the beam geometry used. In

addition, because of the large range in $V_{50\%PD}$ for both OARs and $D_{95\%PTV}$ for the PTV, the impact of the dose algorithm can only be approximated from averages, but the inaccuracies of analytical methods should be considered on a patient by patient basis from more accurate techniques.

7.5 Conclusion

The dose distributions of six dose calculation algorithms were compared in twenty prostate treatment plans. Of the three inhomogeneity correction techniques the ETAR correction factor most closely matched the MC dose calculations. Both analytical and MC inhomogeneity correction algorithms had a greater impact on the PTV than the OARs, when compared with their respective water equivalent calculation. Simulating the patient as a homogeneous water equivalent medium in MC calculations only marginally better matched the water equivalent analytical calculation, indicating that for this cohort of patients and beam geometry, the beam model and dose calculation method have a greater impact than do inhomogeneities. The standard deviations and ranges displayed in Figs 7.1, 7.3, and 7.4 are testament that the differences in dose calculations between MC and analytical algorithms are unpredictable and highly influenced by patient geometry to the point that MC dose calculations for this type of treatment are recommended.

7.6 Afterward

This chapter illustrates the importance of the dose calculation algorithm, and sets the stage for dose calculations in the remainder of the thesis. Although MC calculations have previously been compared with analytical algorithms, the comparison generally always uses MC considering tissue heterogeneities. A comprehensive study using MC without considering tissue heterogeneities had not been performed. It is known that heterogeneity corrections in analytical algorithms have shortcomings, but we revealed that the simplest homogeneous case is also characterized with inaccuracies. We validated the use of MC techniques in the homogeneous pelvic region treated with photon beams. However, it is understood that other analytical algorithms may better predict the dose than the pencil beam algorithm. Nonetheless, dose discrepancies become more important for heterogeneous tissue sites, such as the head and neck region (air cavities, bone, soft tissue), and for electron beams, which are highly influenced by small irregularities in the skin surface. Furthermore, in the presence of motion induced artifacts, as presented in Chapter 8, dosimetric errors become more pronounced, rendering the dosimetric accuracy of analytical-based dose computation unacceptable.

7.7 References

[1] Batho HF. Lung corrections in cobalt 60 beam therapy. *J Can Assoc Radiol* 1964; 15: 79-83

[2] Ahnesjö A and Aspradakis MM. Dose calculations for external photon beams in radiotherapy. *Phys Med Biol* 1999; 44: R99-R155

[3] Fippel M. Fast Monte Carlo dose calculation for photon beams based on the VMC electron algorithm. *Med Phys* 1999; 26: 1466-1475

[4] Kawrakow I and Fippel M. Investigation of variance reduction techniques for Monte Carlo photon dose calculation using XVMC. *Phys Med Biol* 2000; 45: 2163-2183

[5] Kawrakow I, Fippel M, and Friedrich K. 3D electron dose calculation using a Voxel based Monte Carlo algorithm (VMC). *Med Phys* 1996; 23: 445-457

[6] Rogers DWO, Faddegon BA, Ding GX, Ma C-M, We J, and Mackie TR. BEAM: a Monte Carlo code to simulate radiotherapy treatment units. *Med Phys* 1995; 22: 503-524

[7] Abdel-Rahman W. A study of the build-up region of megavoltage radiation beams. *PhD thesis McGill University* 2004 p.198

[8] Alexander A, DeBlois F, Stroian G, Al-Yahya K, Heath E, and Seuntjens J. MMCTP, a radiotherapy research environment for Monte Carlo and patient-specific treatment planning. *Phys Med Biol* 2007; 52: N297-N308

[9] Verhaegen F, Symonds-Tayler R, Liu H, and Nahum AE. Backscatter towards the monitor ion chamber in high-energy photon and electron beams: charge integration versus Monte Carlo simulation. *Phys Med Biol* 2000; 45: 3159-3170

[10] Wong J and Henkelman RM. Reconsideration of the power-law (Batho) equation for inhomogeneity corrections. *Med Phys* 1982; 9: 521-350

[11] Yang J, Li J, Chen L, et al. Dosimetric verification of IMRT treatment planning using Monte Carlo simulations. *Phys Med Biol* 2004; 50: 869-878

[12] du Plessis F, Willemse C, and Lotter M. Comparison of the Batho, and Monte Carlo dose calculation methods in CT based patient models. *Med Phys* 2001; 28: 582-589

CHAPTER 8

Dosimetric consequences of misalignment and realignment in prostate 3DCRT using intramodality ultrasound image guidance

In this chapter we present a manuscript published in the peer reviewed journal *Medical Physics*. It is a follow up study from Chapter 7, in which it was found that the particle transport algorithm has a significant impact on the calculated dose distribution, even in relatively homogenous treatment sites.

Prostate cancer was one of the first sites to routinely undergo image guided radiation therapy, and the vast majority of prostate cancer patients are treated in this manner. The impact of interfraction organ motion has been reported on, but not in a systematic way using the most accurate imaging and dose calculation techniques, nor for a large number of patients using measured (not simulated) data. This study reports on, and dosimetrically quantifies, the results of a treatment technique that has somewhat been taken for granted. That is, accounting for organ motion without performing an updated dose calculation on the new patient geometry.

Title: Dosimetric consequences of misalignment and realignment in prostate 3DCRT using intramodality ultrasound image guidance

Authors: Fraser D, Chen Y, Poon E, Cury F, Falco T, and Verhaegen F

Medical Physics 37(6) pp 2787-2795 (2010)

8.1 Abstract

Purpose: It is common practice to correct for interfraction motion by shifting the patient from reference skin marks to better align the internal target at the linear accelerator's isocentre. Shifting the patient away from skin mark alignment causes the radiation beams to pass through a patient geometry different from that planned. Yet, dose calculations on the new geometry are not commonly performed. The intention of this work was to compare the dosimetric consequences of treating the patient with, and without, setup correction for the common clinical scenario of prostate interfraction motion.

Methods: In order to account for prostate motion, 32 patients initially aligned to the room lasers via skin marks were realigned under the treatment beams by shifting the treatment couch based on ultrasound image guidance. An intramodality 3D ultrasound image guidance system was used to determine the setup correction, so that errors stemming from different tissue representations on different imaging modalities were eliminated. Two scenarios were compared with the reference static treatment plan: 1) uncorrected patient alignment; and 2) corrected patient alignment. Prostate displacement statistics and the dose to the clinical target volume (CTV), bladder, and rectum are reported. Monte Carlo dose calculation methods were employed.

Results: Comparing the uncorrected and corrected scenarios using the static treatment plan as the reference, the average percent difference in D95 for the CTV improved from 5.1 ± 9.0% to -0.0 ± 1.1%, and the average percent difference in V90 for the bladder changed from -11 ± 58% to -8.3 ± 13%, and for the rectum from -47 ± 50% to 0.9 ± 30%, respectively. There was no simple correlation between displacement and dose discrepancy before correction. After patient realignment the prescribed dose to the CTV was achieved within 1% for 75% (24/32) of the patients. For the bladder and rectum, 50% of the patients had doses that differed from the static treatment plan by 25% and 8%, respectively.

Conclusions: The dose degredation due to prostate motion (before correction) is not accurately predicted from the average trends for all patients. Outliers included smaller displacements that lead to larger dosimetric differences in the corrected scenario, especially for the bladder and rectum, which exhibited doses substantially different from that planned.

8.2 Introduction

It is well known that prostate interfraction organ motion occurs, and compromises the accuracy of the expected dose in radiation therapy [1,2]. The role of image guidance is to achieve greater accuracy of daily target volume positioning. It aims to position the target relative to the same reference point (isocentre) as in the reference computed tomography (CT) image so that the treatment plan may be delivered as expected [3].

If target organ motion is not corrected for, the dose distribution will be shifted and blurred due to systematic and random displacements. If organ motion is corrected for, the dose distribution will still differ by an unknown amount from that planned as shown in Fig. 8.1. The isodose volumes change shape because the beams intersect a new geometry (surface contour, depth of penetration, relative tissue position, etc.), placing external contour boundaries and tissue densities at points that are different from the reference CT image [1]. A study of this dosimetric discrepancy (when the patient is realigned under the treatment beams) has not been undertaken in a comprehensive manner in the literature to date and is addressed in this work.

Comparable dosimetric studies using measured organ motion have been limited in the number of patients studied, the dose calculation methods employed, and in the dosimetric analysis[4-6]. We aim to improve on these works by using a substantially larger sample patient population, an intramodality imaging system, accurate dose calculation techniques, and a dosimetric analysis relevant to current treatment plan evaluation methods.

We used an intramodality imaging system to monitor the prostate throughout a course of radiation therapy. Tissue geometry imaged with different techniques do not produce the same results, making a comparison between changes in geometry difficult. [7-11]. For example, averaged over ten patients, prostate volume ratios for CT/magnetic resonance (MR), ultrasound (US)/MR, and CT/US have been reported to be 1.16, 0.9, and 1.30, respectively [12], and prostate CT volumes can be larger than prostate MR volumes by up to 40% [13]. For image guided radiation therapy (IGRT), techniques such as projection radiography, portal imaging, and cone beam CT compare daily images with the reference CT. Only an in-treatment room CT system [14] and US system [15] are capable of true intramodality verification between daily and treatment planning images.

Monte Carlo (MC) dose calculation techniques, which use a first principles approach, are the most accurate dose calculation method. Fraser et al showed that the dose calculation method has a considerable impact on the dose distribution in the pelvic region, even in the

absence of large heterogeneities (for an 18 MV beam with an average photon energy of 6 MeV, the mass energy absorption coefficients for Compton scattering are essentially the same among bone, water, and muscle) [16]. For example, the difference in the dose to 95% of the prostate PTV volume (D95) between heterogeneous MC and heterogeneous analytical pencil beam algorithms has been reported to be a maximum of 7.8% (average 3.5%) for twenty patients, whereas the difference between homogeneous and heterogeneous MC calculations was only up to 2.4% (average 1.7%). This indicates a systematic non-negligible difference between MC methods and analytical algorithms in the pelvic region. MC methods are also better able to model the fluence through a multileaf collimator [17].

A dose volume histogram (DVH) analysis is performed for the clinical target volume (CTV), bladder, and rectum for each fraction for 32 patients. For each fraction, target misalignment and realignment scenarios were considered, and also summed over the entire treatment.

8.3 Methods and materials

8.3.1 Treatment planning and daily imaging

Thirty-two patients diagnosed with localized prostate cancer were treated curatively with 3D conformal radiation therapy using a five field coplanar beam technique. Patients underwent CT simulation imaging 4-6 weeks before the start of treatment. While in the supine position a knee support was used and a styrofoam block was placed between the ankles to ensure consistent leg positioning during planning and treatment. The CTV was defined as the prostate gland, as observed on 3 mm thick axial CT slices, with or without the proximal seminal vesicles depending on the risk of microscopic involvement. The planning target volume (PTV) included a 7 mm isotropic margin around the CTV. The median total dose was 72 Gy delivered in 2 Gy per fraction to the PTV.

During CT simulation and treatment, the patients were instructed to retain an empty rectum and a comfortably full bladder. The latter was verified by users experienced with US imaging, who were able to achieve adequate image quality with minimal probe pressure. Strong probe pressure has been reported to displace the prostate by a maximum of 3 mm [18,19], which is comparable to the interobserver variation in contouring the prostate on the planning CT images [12] and on daily megavoltage cone beam CT images [20].

For each fraction the patient was first aligned to the room lasers based on skin marks. Next, an US image of the prostate was acquired. In this manner, prostate displacement was determined as the difference in the position of the prostate, relative to skin marks, between the time of treatment planning and treatment delivery. Patients were then realigned based on the daily US localization. Reported in this study is prostate displacement, which is in the opposite direction to table motion used to correct patient alignment.

8.3.2 Intramodality ultrasound system

Image guidance was performed with an intramodality 3D ultrasound system (Restitu Platform V.2.0.0.334, Resonant Medical Inc., Montréal, QC (now known as Clarity System)). The procedure for measuring prostate motion is outlined in Johnston et al [8]. The key features of this system are that 1) daily 3D US images acquired in the treatment room are compared with another reference US image acquired in the CT simulation room at the time of treatment planning, and 2) the absolute position of the US image planes are known using tracked infrared emitters attached to the probe permitting automatic fusion of US and CT images. The 3D prostate contour on the reference US image was used to determine all daily displacements. This reference contour was automatically overlaid on the daily images at the reference position, and then manually moved until a best fit was obtained with the daily position. The difference between the reference position and the daily position determined prostate displacement. Using an US derived contour as the reference made this matching process easier to perform than using a CT derived contour. Cury et al used the same ultrasound system and concluded that intramodality US is more accurate than intermodality US [15].

The Restitu system has been reported to be reproducible within 0.5 mm for daily and monthly phantom measurements in the CT simulation room [8], to produce prostate US contours that overlap with CT contours within 90% [21], and to be accurate within 2 mm between the CT and linac rooms by the manufacturer [22]. In comparison, the accuracy of a kV imaging system (ExacTrac X-ray, BrainLAB, Germany) that also uses a Polaris camera to monitor couch motion, has also been reported to be accurate within 2 mm [23].

8.3.3 Prostate displacement

Organ displacement metrics were calculated based on van Herk et al [24] The mean and standard deviation (SD) of daily prostate displacements were determined per patient (patient mean and patient SD). The systematic/interpatient variation (Σ) is the SD of all patient means.

The random/intrapatient variation (σ) is the root mean square average of patient SDs. The group systematic displacement (M) is the mean of all patient means. 3D displacement was also calculated for each fraction before averaging over all fractions.

8.3.4 Dose calculations

All MC dose calculations used the EGSnrcmp [25]/BEAMnrc [26] code to model the linear accelerator (Clinac 2300 C/D; Varian Medical Systems Inc., Palo Alto, CA), previously validated at our institution [27], and the XVMC [28] algorithm to perform heterogeneous dose calculations. The patient density and dose matrices had a resolution of at least 2.15 mm in the right/left (RL) and anterior/posterior (AP) directions, and 3 mm in the superior/inferior (SI) direction. The statistical uncertainty for each dose calculation was about 1%.

For each patient the reference static plan was recalculated using MC techniques (original plans were performed with CADPLAN v6.0, Varian Medical Systems Inc., Palo Alto, CA). For each fraction two dose calculations, using the reference CT image, were compared as shown in Fig. 1. First, the uncorrected scenario simulated interfraction prostate displacement without realigning the patient. The dose distribution was calculated by rigidly translating the CT contours from the reference position on the planning CT image to the US measured displaced position. The bladder and rectum were shifted with the prostate. Although the bladder and rectum may undergo daily volume changes [29], the bladder and rectum tissue near the boundary with the prostate will move similarly to the prostate. This boundary tissue also receives the highest dose, which is important for determining organ at risk (OAR) toxicity [30]. For this reason, the volume receiving at least 90% of the prescribed dose (V90) is used as the dose metric for the OARs (bladder and rectum). Second, the corrected scenario simulated interfraction prostate displacement with patient realignment. In this scenario, the dose to the CTV, bladder, and rectum was recalculated by translating the patient (containing shifted contours) to locate the prostate at the isocenter of the radiation beams, thereby changing the entry point of the beams.

The cumulative dose to the CTV, bladder, and rectum were compared between the uncorrected and corrected scenarios using the percent difference (Δ) from the static plan. Outliers are defined with respect to the first and third quartiles, and the interquartile range. DVHs are shown for a single patient.

In order to compare with other studies, the strength of a linear relationship between displacement and percent dose difference was tested with the Pearson correlation coefficient (r), where $|r| = 1$ suggests a perfect positive or negative linear relationship.

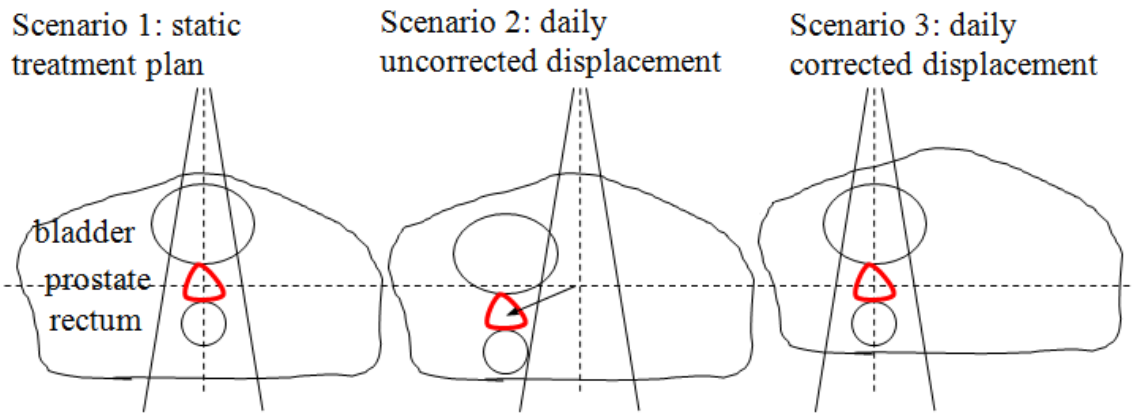

FIG. 8.1 Schematic representation of three different scenarios calculated for each patient, and used to assess the dosimetric consequences of isocentre misalignment and realignment during external beam radiation therapy. The scenarios are exaggerated to clarify the differences.

8.4 Results

8.4.1 Organ motion

The US measurements of interfraction prostate displacements are summarized in Table 8.1. The percentage of measurements that resulted in 3D prostate displacements outside of the 7 mm PTV margin was 73%. Large displacements exceeding 10 mm were more common in the posterior direction than in all other directions (19.3% posterior compared to 9.6% inferior and 5.3% left). Even though M is largest in the AP direction, 15/32 (47%) and 12/32 (38%) patients had larger SI and RL displacements than AP displacements, respectively. Consequently, a considerable number of patients did not follow the average trends. The values in Table 8.1 are in agreement with other reported studies (reference 8 and references therein).

Figure 8.2 displays histograms of the individual fraction shifts for all patients, as well as patient systematic shifts compared to group systematic shifts.

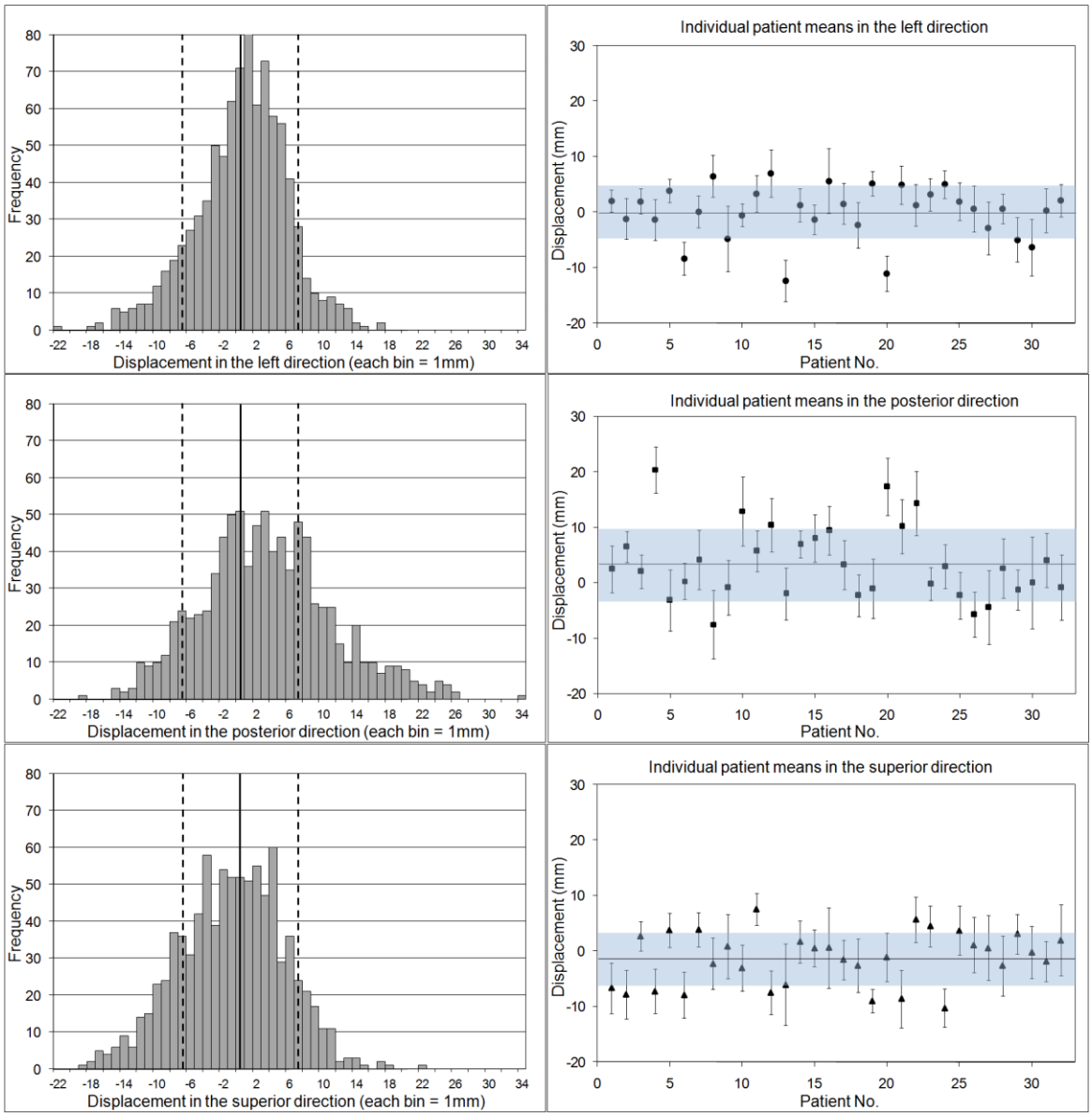

FIG. 8.2 Individual patient displacement data for interfraction prostate motion. The graphs on the left are histograms in each direction. The solid vertical lines indicate the origin/reference position, and the dashed vertical lines indicate 7 mm. The graphs on the right represent patient means (data points) and patient standard deviations (error bars). The thick solid band indicates the systematic variation Σ for each direction.

TABLE 8.1 Interfraction prostate displacement metrics. *Abbreviations*: M is the group systematic displacement, Σ is the standard deviation of all patient means, and σ is the root mean square average of patient standard deviations.

	Patient Left = + (mm)	Posterior = + (mm)	Superior = + (mm)	3D displacement (mm)
M (range)	0.0 (-12.4, 7.0)	3.5 (-7.5, 20.4)	-1.4 (-10.3, 7.6)	11.3 (5.6, 22.3)
Σ	4.8	6.7	4.8	4.1
σ (range)	3.6 (2.0, 5.9)	4.8 (2.4, 8.3)	4.5 (2.1, 7.3)	3.8 (2.1, 6.2)

8.4.2 Dose calculations

The group averages of Δmean dose to the CTV, bladder, and rectum in the uncorrected and corrected scenarios are given in Table 8.2. Also presented are the group averages of ΔD95 for the CTV, and ΔV90 for the OARs. Fig. 8.3 shows the association between uncorrected and corrected dose metrics for the CTV and OARs for each patient. In Fig. 8.4, ΔD95 for the CTV and ΔV90 for the OARs are compared with their respective mean 3D displacements for each patient.

When the patient was not realigned under the beams the average discrepancy in the mean dose to the CTV, bladder, and rectum are 2.1% (range 20% to 0.6%), 3.3% (range 23% to 56%), and 11% (range 50% to 28%), respectively. ΔD95 and ΔV90 are more sensitive to motion and show larger differences between patients. The average discrepancy in ΔD95 for the CTV and ΔV90 for the bladder and rectum are 5.1% (range 40% to 1.3%), 10.5% (range 84% to 232%), and 47% (range 100% to 108%), respectively. For all scenarios, there was a larger range in the OAR metrics than the CTV metrics. When the patient is corrected for target misalignment, the group averages of all corrected plan metrics are similar to those at the time of treatment planning, except for V90 for the bladder. However, the standard deviations and ranges show a large variation between, and demonstrate a strong dependence on, the patient in question. For example, outliers in ΔD95 for the CTV and ΔV90 for the bladder and rectum represent 13%, 6%, and 25% of the patients, respectively. Additionally, an outlier with respent to one organ does not always correspond to an outlier with respect to another organ. The data also shows that dose recovery is sometimes unpredictable as a smaller dose discrepancy in the uncorrected scenario does not always correspond to a smaller dose discrepancy in the corrected scenario.

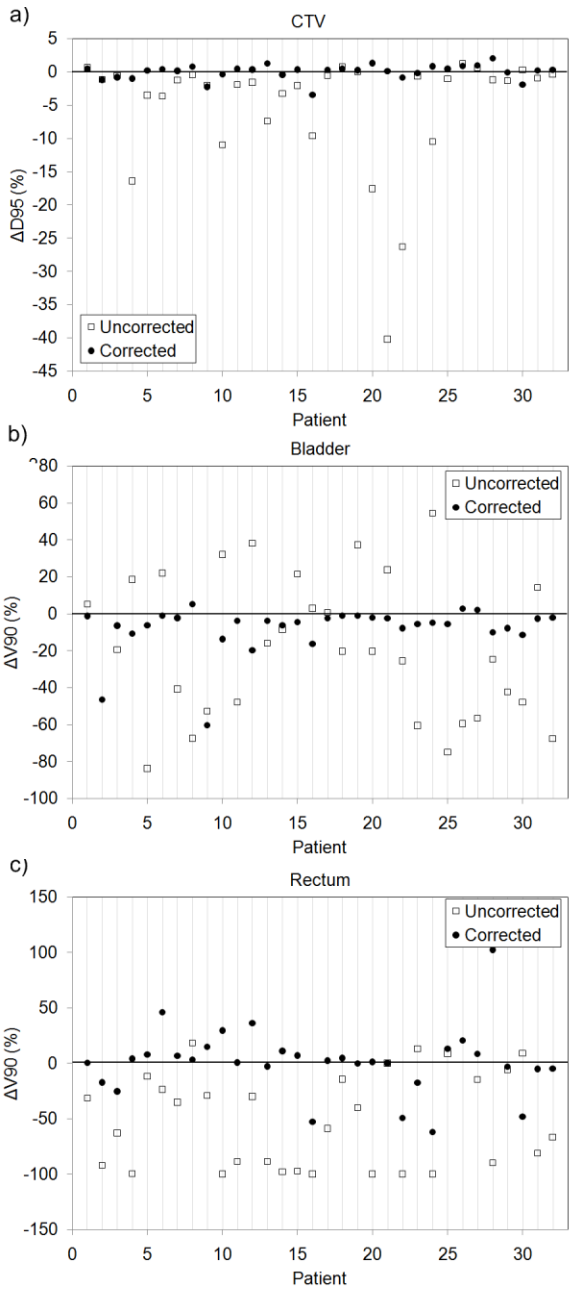

FIG. 8.3 Dose metrics from the uncorrected and corrected scenarios presented as a percent difference from the static treatment plan: a) dose covering 95% of the clinical target volume (CTV); and the volume of the b) bladder and c) rectum containing 90% of the prescribed dose. The uncorrected and corrected values corresponding to each patient are aligned vertically. Note that there is a bladder data point in the uncorrected scenario at 234% not shown on the graph.

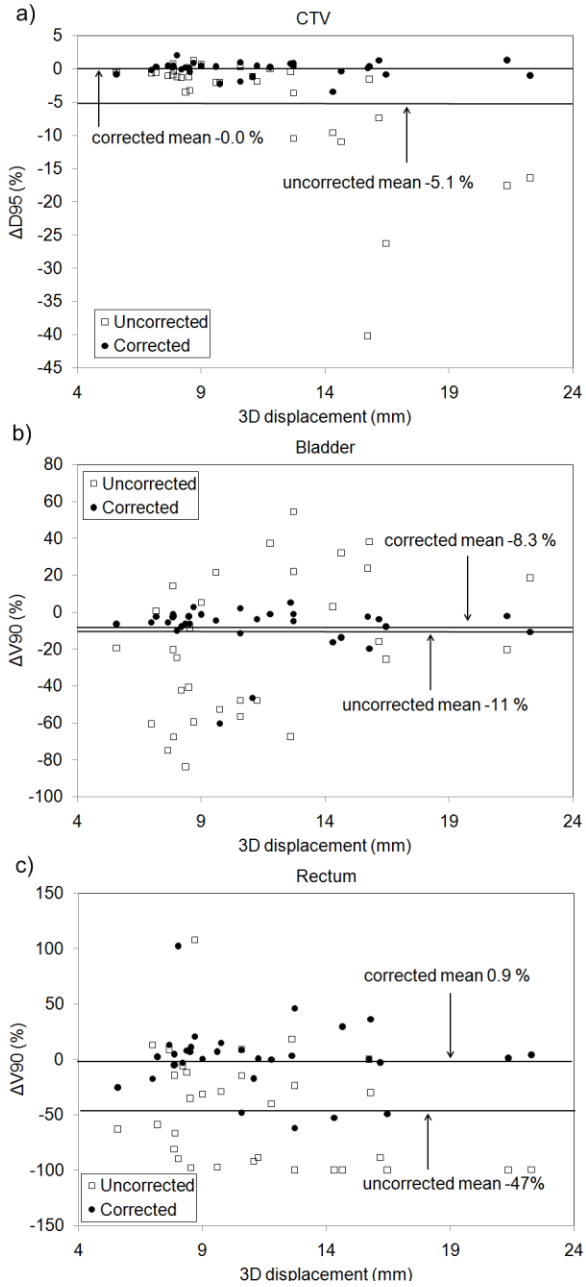

FIG. 8.4 Dose metrics as a function of 3D displacement presented as a percent difference with the static treatment plan for the a) clinical target volume (CTV), b) bladder, and c) rectum. The average uncorrected and corrected differences are indicated with horizontal lines. Note that there is a bladder data point in the uncorrected scenario at 234% not shown on the graph.

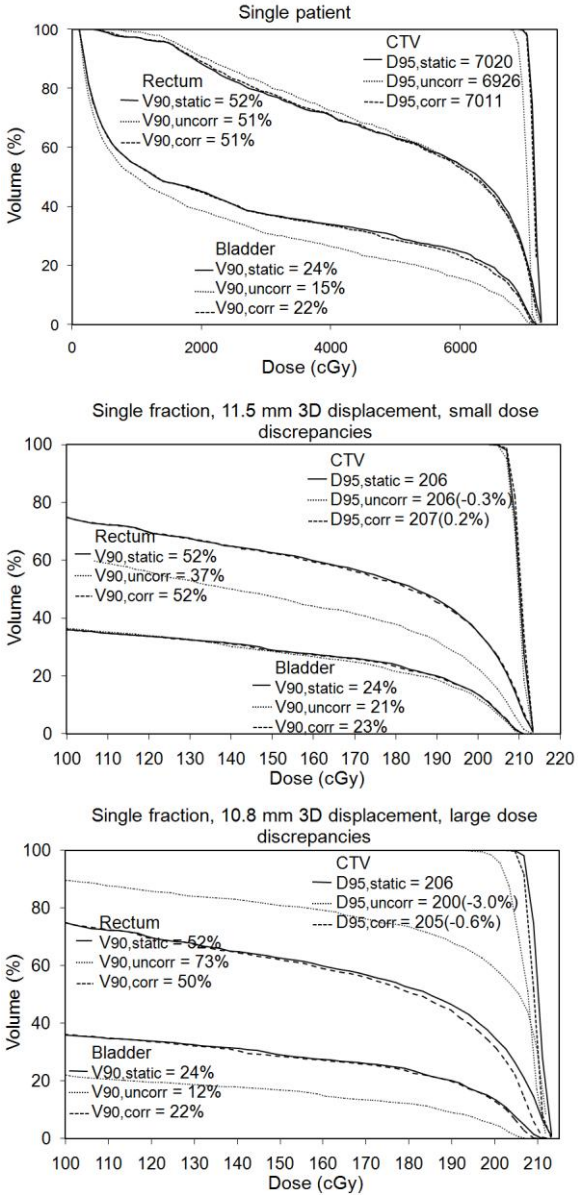

FIG. 8.5 Dose volume histograms for the static, uncorrected (uncorr), and corrected (corr) scenarios for a single patient for a) the entire treatment plan for the clinical target volume (CTV), bladder, and rectum, b) a single fraction that had a 10.8 mm 3D displacement for the CTV and a large CTV D95 uncorrected dose discrepancy (-3.0%), and c) a single fraction that had an 11.5 mm 3D displacement for the CTV and a small CTV D95 uncorrected dose discrepancy (-0.3%).

TABLE 8.2 Group averages of dose metrics to the cinical target volume (CTV), bladder, and rectum, presented as a percent difference (Δ) with the static treatment plan. *Abbreviations:* D95 is the dose to at least 95% of the volume and V90 is the volume containing at least 90% of the prescribed dose.

		Average ± standard deviation (range) (%)	
Organ	Metric	Uncorrected scenario	Corrected scenario
CTV	Δmean dose	-2.1 ± 4.0 (-20.3, 0.6)	-0.4 ± 0.8 (-2.7, 0.8)
	ΔD95	-5.1 ± 9.0 (-40.2, 1.3)	-0.0 ± 1.1 (-3.5, 2.0)
bladder	Δmean dose	3.3 ± 19.3 (-22.8, 55.7)	-0.6 ± 1.0 (-3.3, 2.2)
	ΔV90	-10.5± 58.3 (-83.8, 232)	-8.3 ± 13.1 (-60.5, 5.2)
rectum	Δmean dose	-10.7 ± 18.6 (-49.5, 27.8)	-0.1 ± 1.5 (-2.5, 7.1)
	ΔV90	-47.0 ± 50.2 (-100, 108)	0.9 ± 30.4 (-62.3, 102)

DVHs for three situations are shown in Fig. 8.5 for a single patient whose mean 3D displacement was 8.2 mm. Figures 8.5a and 8.5b demonstrate unpredictable behaviour, in that similar large displacements during two different fractions for the same patient vary in their impact on the uncorrected D95 to the CTV by 3%. On the other hand, in the corrected scenario, large and small uncorrected dose discrepancies can be reduced to almost zero. Figure 5c shows the DVH for the cumulative dose over the entire treatment.

8.5 Discussion

8.5.1 Uncorrected scenario

Averaged over the group of patients the reduction in D95 for the CTV in the uncorrected scenario was relatively small at -5.1 ± 9.0% for a group systematic 3D displacement of 11.3 mm. This is mostly explained by the 7 mm PTV margin. The OARs are more affected by motion in the uncorrected scenario than the target CTV, as shown in Fig. 8.4. The CTV is located in a homogenous dose region, but the bladder and rectum have a large dose gradient near, or within their boundaries, making the dose to the bladder and rectum more sensitive to motion. This conclusion was also drawn in a review on prostate motion [2]. Unlike the review we did not observe the amount of under or over dose to the organs to be directly proportional to the magnitude of the shifts. A weak to moderate correlation was found using the Pearson correlation coefficient (r). The correlation coefficient between the uncorrected dose to the CTV and patient

mean 3D displacement was -0.55 ($p \leq 0.001$) for Δmean, and 0.77 ($p \leq 3x10^{-5}$) for ΔD95. By taking r^2 we observe that only 30-60% of the variation in the CTV is associated with a variation in 3D displacement. In Fig. 8.4a larger ΔD95 values tend to be more negative as displacement increases. The relationship between dose and displacement depends on the shape and position of the contours with respect to the isodose lines. The change in dose, from the center of the CTV, along the direction of displacement would be better modeled by a nonlinear relationship, and would yield better correlation.

The dose metrics in Table 8.2 in the uncorrected scenario are more positive for the bladder and more negative for the rectum corresponding to an average posterior prostate displacement where the bladder would have been shifted closer to the isocenter, and the rectum farther.

8.5.2 Corrected scenario

The uncorrected ΔD95 for the CTV, and V90 for the bladder and rectum, were reduced in the corrected scenario to 0.0%, 8.3%, and 0.9%, respectively. The maximum corrected ΔD95 for the CTV was 3.5%. Orton et al [5], who used intermodality 3D US IGRT and the ADAC Pinnacle treatment planning system on five patients, also found that the prescribed dose was achieved with realignment. The patients were treated with IMRT and the analysis was performed on the PTV, both of which should increase sensitivity to motion. PTV margins are specifically designed to capture daily motion and setup uncertainties, so that focusing on the PTV instead of the CTV may be misleading. Repositioning studies should focus on recovering the dose to the CTV. Dose recovery may have been possible in their study because a rectal balloon was used to immobilize the prostate. However, the authors state that the rectal balloon, which is not common practice, may have introduced false organ motion for small sized prostates. Another dosimetric interfraction prostate motion study was performed by aligning ten patients to skin marks, bony anatomy, and intermodality 2D US measurements [4]. The authors used the minimum dose to a 0.1 cm^3 volume of the prostate as their metric and found that differences in the minimum dose depended on the alignment technique. Similar to our study they found that the results were not consistent across patients. The authors calculated the dose on CT images acquired on a daily basis, but they did not sum the dose distributions, so that the minimum dose may not have occurred in the same volume of tissue each day. Therefore, the reported minimum dose represents a worst case scenario. Wertz et al [6] compared CT images of empty and distended rectums for one fraction and also found a 10% improvement of the mean dose to the

rectum when the patient was corrected for bony anatomy misalignment. This result corresponds to the data presented in Table 8.2

Coplanar parallel opposed photon beams may reduce the impact of prostate motion in the direction parallel to the beams. That is, motion that reduces prostate depth for one beam will be compensated for with increased prostate depth with the opposite beam. However, this does not fully explain why, in general, the same dose was delivered in the planned and corrected scenarios. Only 2/5 beams were parallel opposed (gantry angles of 0°, 90°,110°, 250°, and 270°). This study shows that even though the beams intersect a different geometry after patient realignment, the expected dose to the CTV can be still be achieved for the majority of patients. Outliers, identified through daily dose calculations, and representing a substantial portion of the sample population, may benefit from replanning that takes into account the new geometry. Patient specific dose discrepancy is unpredictable with motion, and may be larger for smaller displacements. This is demonstrated in Figures 8.5a and 8.5b. Each figure is a DVH of a single fraction for the same patient in which ΔD95 in the uncorrected and corrected scenarios are larger for the smaller 10.8 mm 3D displacement (3.0% and 0.6%, respectively) than for the larger 11.5 mm 3D displacement (0.3% and 0.2%, respectively). This patient is an example that there is no monotonic trend between dose discrepancy and displacement. A closer look at the components of the displacement reveals that the largest component of the 10.8 mm 3D displacement was 9.6 mm AP, and for the 11.5 mm 3D displacement it was 10.5 mm RL. Figure 8.5c shows that after the entire treatment was delivered, the planned dose distribution was achieved for the CTV and rectum, and improved for bladder sparing. For 75% (24/32) of the patients in this study, the prescribed dose to the CTV after correction was achieved within 1%. In contrast, for 13% (4/32) of the patients the dose to the CTV was outside of 1.5 SD of the average ΔD95. For the bladder and rectum after patient realignment, 50% of the patients had doses that differed from the static treatment plan by 25% and 8%, respectively.

The advantages of using US were an intramodality image comparison, a non-invasive IGRT procedure, in terms of both zero imaging dose and no need of surgically implanted fiducial markers, the ability to collect volume information, and the ability to image at both the planning and treatment stages despite metal prostheses. However, it is recognized that US has limitations. Operator dependency affects image quality and daily to reference position comparisons. In this work, all US operators had four years experience with the BAT (North American Scientific, Chatsworth, CA) US system for prostate scanning, and went through several Restitu training sessions with the manufacturer. It is also noted that US systems assume a constant speed of

sound of 1540 m/s in all tissues (presupposing no elasticity or density differences between various human tissues). This is estimated to have a small impact on the absolute position of a pelvic organ, if the bladder was comfortably full at each fraction, because the daily prostate US position was measured relative to the reference US position acquired at treatment planning. This effect could have a larger impact for systems that compare US to a CT reference image. For organ displacement, our simple rigid model did not consider rotations, which have been shown to be on the order of a few degrees [31]. Our study also assumed that the OARs moved with the prostate (CTV), which is true near the CTV boundaries. For the dose calculations it is noted that the true dose to internally shifted organs cannot be determined daily without a pre treatment image that covers the full 3D volume in which the beams intersect the patient. Ideally this would require an imaging modality in which (relative) electron densities can be extracted. The use of DVH metrics in the analysis removes the spatial information of where within the organ under or over dose occurs.

Despite these limitations 3D US IGRT provides daily information to monitor organ motion and volume changes, such as during concurrent hormone therapy and radiation therapy. The data would be used as a trigger to decide when a patient would better benefit from realignment or re-planning.

8.6 Conclusion

This study quantified the change in target and OAR dose distributions caused by shifting the patient from skin mark alignment in order to correct for prostate interfraction motion. An analysis of the MC dosimetric impact of prostate interfraction organ motion for 32 patients, demonstrated that organ motion was not a good predictor of dose degradation. Organ motion also had a larger impact on the delivered dose to the bladder and rectum than to the CTV. In general, realigning the patient to correct for motion reduced dose discrepancies in the CTV, but outliers, and the large variation between patients, indicate that considerable changes in the dose distribution can remain after patient realignment. The remaining dose degradation may become more important for dose escalation and hypofractionation studies.

8.7 Acknowledgements

William Parker, Clarisse Mark, Aichu Chang, François deBlois, Philippe Fortier, Fred Francis, Martin Lachaine, and Rui Lopes are thanked for their valuable contributions. FV was supported by Fonds de la Recherche en Santé Québec. The US equipment and MC engine were

partially acquired with a New Opportunity Grant of the Canada Foundation for Innovation (CFI, Grant #10036). The research was also partially supported by an ACURA grant of the Canadian Association of Radiation Oncology.

8.8 Afterward

This chapter demonstrated that the dose delivered to a realigned patient is very close to that predicted in the static treatment plan for all organs. However, these results are specific to 3DCRT and a 7 mm CTV to PTV margin. The organs at risk were more affected by prostate motion than was the CTV because they lie on the boundary of a sharp dose gradient so that small movements can locate the organs in vastly different dose regions. In this study we modeled the impact of prostate motion on the organs at risk by rigidly shifting them with the prostate. This may be accurate for tissue boundaries with the prostate but does not represent their true deformation. Although possible with the ultrasound system used, we also did not take into account prostate rotation. It was also determined that prostate organ motion is unpredictable as outliers exist in the patient population. This dosimetric verification study confirms current clinical practice of shifting the patient on the treatment couch to locate the prostate at the isocentre.

8.9 References

[1] Bortfeld T, Jiang SB, and Rietzel E. Effects of motion on the total dose distribution. *Sem Radiat Oncol* 2004; 14: 41-51

[2] Byrne TE. A review of prostate motion with considerations for the treatment of prostate cancer. *Med Dosim* 2005; 30: 155-161

[3] Yorke ED, Keall PJ, and Verhaegen F. Anniversary paper: Role of medical physicists and the AAPM in improving geometric aspects of treatment accuracy and precision. *Med Phys* 2008; 35: 828-839

[4] O'Daniel JC, Dong L, Zhang L, et al. Dosimetric comparison of four target alignment methods for prostate cancer radiotherapy. *Int J Radiat Oncol Biol Phys* 2006; 66: 883-891

[5] Orton N and Tomé W. The impact of daily shifts on prostate IMRT dose distributions. *Med Phys* 2004; 31: 2845-2848

[6] Wertz H, Lohr F, Dobler B, et al. Dosimetric consequences of a translational isocenter correction based on image guidance for intensity modulated radiotherapy (IMRT) of the prostate. *Phys Med Biol* 2007; 52: 5655-5665

[7] Gayou O and Miften M. Comparison of mega-voltage cone-beam computed tomography prostate localization with online ultrasound and fiducial markers methods. *Med Phys* 2008; 35: 531-538

[8] Johnston H, Hilts M, Beckham W, et al. 3D ultrasound for prostate localization in radiation therapy: A comparison with implanted fiducial markers. *Med Phys* 2008; 35: 2403-2413

[9] Langen KM, Pouliot J, Anezinos C, et al. Evaluation of ultrasound-based prostate localization for image-guided radiotherapy. *Int J Radiat Oncol Biol Phys* 2003; 57: 635-644

[10] McNair HA, Mangar SA, Coffey J, et al. A comparison of CT- and ultrasound-based imaging to localize the prostate for external beam radiotherapy. *Int J Radiat Oncol Biol Phys* 2006; 65: 678-687

[11] Scarbrough TJ, Golden NM, Ting JY, et al. Comparison of ultrasound and implated seed marker prostate localization methods: implications for image guided radiotherapy. *Int J Radiat Oncol Biol Phys* 2006; 65: 378-387

[12] Rasch C, Barillot I, Remeijer P, et al. Definition of the prostate in CT and MRI: a multi-observer study. *Int J Radiat Oncol Biol Phys* 1999; 43: 57-66

[13] Smith W, Lewis C, Bauman G, et al. 3DUS, MRI and CT prostate volume definition: 3D evaluation of intra- and inter-modality and observer variability. *Med Phys* 2005; 32: 2083-2083

[14] Court L, Rosen I, Mohan R, et al. Evaluation of mechanical precision and alignment uncertainties for an integrated CT/LINAC system. *Med Phys* 2003; 30: 1198-1210

[15] Cury FL, Shenouda G, Souhami L, et al. Ultrasound-based image guided radiotherapy for prostate cancer-comparison of cross-modality and intramodality methods for daily localization during external beam radiotherapy. *Int J Radiat Oncol Biol Phys* 2006; 66: 1562-1567

[16] Fraser D, Mark C, Cury F, et al. Comparison of conventional and Monte Carlo dose calculations for prostate treatments. *J Phys: Conf Ser* 2008; 102: 012010

[17] Mihaylov IB, Lerma FA, Wu Y, and Siebers JV. Analytic IMRT dose calculations utilizing Monte Carlo to predict MLC fluence modulation. *Med Phys* 2006; 33: 828-839

[18] Artignan X, Smitsmans MH, Lebesque JV, Jaffray DA, van Herk M, and BartelinkH. Online ultrasound image guidance for radiotherapy of prostate cancer: impact of image acquisition on prostate displacement. *Int J Radiat Oncol Biol Phys* 2004: 59; 595-601

[19] Dobler B, Mai S, Ross C, Wolff D, Wertz H, Lohr F, Wenz F. Evaluation of possible prostate displacement induced by pressure applied during transabdominal ultrasound image acquisition. *Strahlenther Onkol* 2006; 182: 240-246

[20] Bylund KC, Bayouth JE, Smith MC, Hass AC, Bhatia SK, and Buatti JM. Analysis of interfraction prostate motion using megavoltage cone beam computed tomography. *Int J Radiat Oncol Biol Phys* 2008; 72: 949-956

[21] Dubé F and Sheldon T. Accuracy of Implicit Registration Between CT and 3D US in the Radiotherapy Simulation Process. *Med Phys* 2008; 35: 2683-2685

[22] Restitu Platform User Guide Vol. 1 U/S-Sim & U/S-Guide. Montreal QC: Resonant Medical 2006 p.57

[23] Hayashi N, Obata Y, Uchiyama Y, Mori Y, Hashizume C, and Kobayashi T. Assessment of spatial uncertainties in the radiotherapy process with the Novalis system. *Int J Radiat Oncol Biol Phys* 2009; 75: 549-557

[24] van Herk M. Errors and margins in radiotherapy. *Semin Radiat Oncol* 2004; 14: 52-64

[25] Kawrakow I. Accurate condensed history Monte Carlo simulation of electron transport. I. EGSnrc, the new EGS4 version. *Med Phys* 2000; 27: 485-498.

[26] Rogers DWO, Faddegon B, Ding G, et al. BEAM: a Monte Carlo code to simulate radiotherapy treatment units. *Med Phys* 1995; 22: 503-524

[27] Abdel-Rahman W, Seuntjens J, Verhaegen F, et al. Validation of Monte Carlo calculated surface doses for megavoltage photon beams. *Med Phys* 2005; 32: 286-298

[28] Kawrakow I and Fippel M. Investigation of variance reduction techniques for Monte Carlo photon dose calculation using XVMC. Phys Med Biol 2000; 45: 2163-2183

[29] Lebesque JV, Bruce AM, Kroes AP, et al. Variation in volumes, dose-volume histograms, and estimated normal tissue complication probabilities of rectum and bladder during conformal radiotherapy of T3 prostate cancer. *Int J Radiat Oncol Biol Phys*. 1995; 33: 1109-1119

[30] Huang EH, Pollack A, Levy L, et al. Late rectal toxicity: Dose-volume effects of conformal radiotherapy for prostate cancer. *Int J Radiat Oncol Biol Phys* 2002; 54: 1314-1321

[31] Aubry JF, Beaulieu L, Girouard LM, et al. Measurements of intrafraction motion and interfraction and intrafraction rotation of prostate by three-dimensional analysis of daily portal imaging with radiopaque markers. *Int J Radiat Oncol Biol Phys* 2004; 60: 30-39

CHAPTER 9

Dosimetric evolution of the breast electron boost target using 3D ultrasound imaging

In addition to photons, the second most common method of delivering external beam radiation therapy is with electrons, making a smaller but substantial contribution. They represent an important treatment modality in modern radiation therapy, often providing a unique option in the treatment of superficial disease (less than 5 cm deep) because of their finite range. At the Montreal General Hospital about 15% of treatments are delivered with electron beams, and breast cancer is one of them.

In women, breast cancer leads incidence with an estimated 22 700 new cases in 2009 in Canada, and it is the second leading cause of cancer mortality[*]. In this chapter we present a manuscript published in *Radiotherapy and Oncology*. This study uses a novel combination of two techniques for breast electron boost treatment. We first make the case that a CT based Monte Carlo dose calculation reveals the pitfalls of conventional treatment planning. Secondly, in a dosimetric analysis of interfraction motion, we incorporate geometric changes in the target, which are known to occur in time frames relevant to radiation therapy.

The electron beam model used in this work was verified, but is not presented in the following manuscript, and so will be described below. Section 4.3 describes some of the components of the model and provides a schematic of the parameters. The BEAMnrcmp MC code was used to model a Varian Clinac 21EX linear accelerator, starting with the electrons at the exit window and ending at the bottom of the electron applicator. This model has previously been verified at our institution for 9 MeV and square field sizes ranging from 5x5 cm^2 to 20x20 cm^2

[*] Canadian Cancer Society's Steering Committee. Canadian Cancer Statistics 2009. (Toronto: Canadian Cancer society, 2009)

(see reference 27). Some changes to this model were made for this thesis including the design of the monitor chamber, changes to some component materials, and the design of the applicator. For this work, we verified the changes, and beam geometries relevant to the patients in this study. Simulated and measured central axis PDD differences for 9 MeV, various field sizes, an extended source-to-surface distance, and an oblique gantry angle can be found in Fig. 9.1. Measurements were performed with a Welhöffer IC10 ionization chamber. The statistical uncertainty on the validation simulations was less than 0.5% (of the maximum dose) at the depth of 50% (R50). For all parameters, simulation and measurements matched within 0.5 mm and 1.2 mm at the depth of R50 and maximum dose, respectively. The differernce between simulation and measurement when the gantry was rotated 345° is due to the effective volume of the IC10 ionization chamber, 0.13 cm^3. At 39 mm depth the PDD exits the beam penumbra while the chamber averages the dose over it's volume, which has a diameter of 0.52 cm and a length of 0.58 cm. In no other measurement does the PDD leave the beam width.

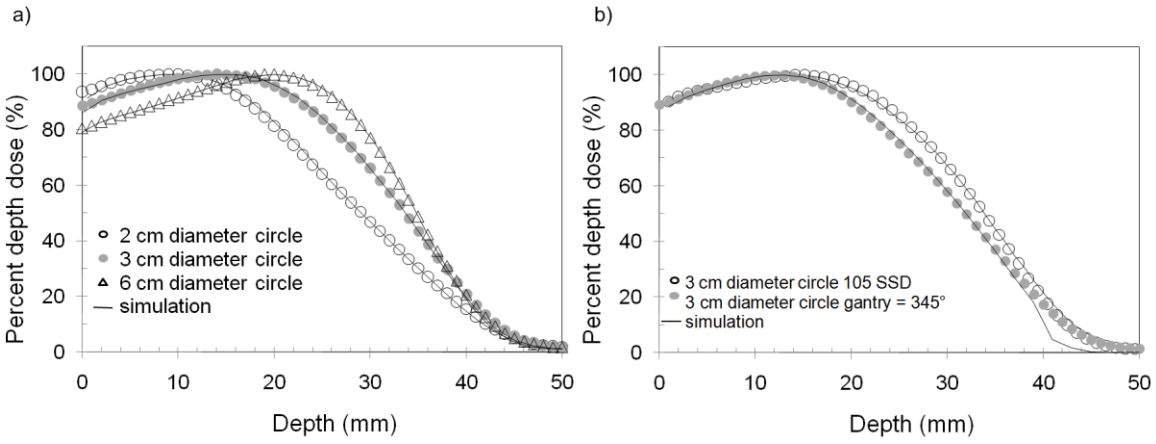

FIG. 9. 1 (a) Simulated and measured percent depth dose (PDD) curves in water for a 9 MeV beam at 100 cm source-to-surface distance (SSD). (b) PDDs at 105 cm SSD, and at 100 cm SSD with the gantry rotated 345°. All Monte Carlo error bars are smaller than the data points.

For patient dose calculations, phase space files were scored containing information on the particles crossing a plane immediately below the patient specific cerrobend block that is inserted into the last plate of the applicator at 95 cm. At least 390 000 particles cm^{-2} are contained in the phase space file ensuring a statistical uncertainty smaller than 0.2% on the quantities derived from that phase space. Patient dose distributions were calculated using

DOSXYZnrcmp by transporting particles from the scoring plane through the patient CT geometry, and taking into account any collimator, gantry, and couch rotations in the treatment plan. When called for, bolus was modeled with water equivalent medium on the patient's skin. The voxel sizes for patient dose calculations were 1.5 mm x 1.5 mm x 3 mm. The number of sampled particles from scoring plane 2 was made sufficiently high, recycling particles as necessary, so that the statistical uncertainty on doses > 50% of the maximum dose was about 0.5% of the maximum dose.

Title: Dosimetric evolution of the breast electron boost target using 3D ultrasound imaging
Authors: Fraser D, Wong P, Sultanem K, and Verhaegen F
Radiotherapy and Oncology doi:10.1016/j.radonc.2010.05.017 (2010)

9.1 Abstract

Purpose: To investigate treatment planning, patient set-up, and interfraction motion errors on the delivered dose for external beam electron boosts for postoperative early stage breast cancer patients.

Methods and materials: For 5 patients, 10-15 Gy was prescribed and administered via a conventionally defined electron boost treatment field — no dose distribution was calculated. Two computed tomography (CT) data sets were acquired an average of 47 days apart. Using Monte Carlo techniques the clinically defined electron beams were reconstructed on CT1 and CT2, and a dosimetric comparison between the two data sets was made. Additionally, 3D ultrasound (US) imaging was performed to monitor interfraction motion. 3D US images were acquired concurrently with the CT images, as well as prior to each boost fraction in the treatment room. Taking into account interfraction motion, the dose to the clinical target volume (CTV) was also calculated.

Results: Based on conventionally determined treatment fields the CT1-based CTV D95 averaged 49% (range 12–89%) of the prescribed dose. Representing setup errors, the CT2-based CTV D95 averaged 47% (range 16–91%) of the prescribed dose. Considering interfraction motion, the average radial displacement was 11 mm, and the resulting CTV D95 was further reduced in 2/5 patients.

Conclusion: Poor initial coverage at the time of planning is exacerbated by breast mobility and interfraction TB motion, increasing the uncertainty in the delivered dose.

9.2 Introduction

After breast conserving surgery (lumpectomy) for early stage breast cancer, a photon treatment plan is commonly followed by an external beam electron boost to the postoperative site – the tumour bed (TB) [1]. The TB is known to undergo tissue remodeling in time frames relevant to radiation therapy planning and delivery [2-5], and setup errors can be substantial [6-8], affecting the delivered dose [9]. Image guidance techniques are used to monitor the position of the target on a daily basis. Current modalities to image the TB may include

ultrasound (US) [10-13], cone beam computed tomography (CT) [6,9], and x-ray imaging of implanted fiducial markers [2,7,8,14-17].

The advantages of using US are that it is a non-invasive and non-ionizing imaging method with good soft tissue contrast. Because of the low soft tissue contrast of cone beam CT, the breast surface or chest wall is often used as a surrogate for the TB. Yet, considerable geometric uncertainties in the position of the TB relative to bony anatomy and breast surfaces have been observed [6]. Cone beam CT also exposes the patient to extra low dose radiation, the risks of which are unclear [5]. Alternatively, surgical clips have been considered the reference standard for TB localization [12], yet subsequent CT scans have shown that clips can move with respect to the TB [16]. Moreover, the position and number of implanted clips are inconsistent [14], and small titanium clips are insufficiently visualized on in-room kV and MV images, while tantalum clips can produce volume artifacts up to 0.81 cm^3 [18]. Uncertainties in US delineated TBs stem from volumes that are consistently small compared to CT [10,11], which emphasizes volumes that may overestimate the TB volume compared with surgical clips [14]. TB delineation on CT images is affected by clinical and radiographic features of the breast [19], such that interobserver variation in breast CT contours have been reported to be larger than inaccuracies predicted from setup uncertainties [20]. On the other hand US has been associated with improved interobserver contour conformity compared to CT [10], suggesting that it can better differentiate the cavity from surrounding tissue, notably for thin patients [12], and when CT cavity visualization is poor [10,11].

Another source of error in the treatment planning process for electron beams is the dose calculation. Conventionally, electron boosts are not planned with a treatment planning system but with clinical techniques [21], a method that carries significant risk of missing the target [22]. In the simplest form, no computer calculation is performed, and the prescription is given to a specified depth near the depth of dose maximum, interpolated from measured percent depth doses (PDD) in a water tank. This method inherently lacks the ability for dose volume histogram (DVH) analysis. It is well accepted that Monte Carlo (MC) simulations offer the most advanced and accurate techniques for 3D treatment planning. The characteristics of external electron beams with oblique beam incidence, tissue heterogeneities, skin surface irregularities, missing tissue, and superficial targets in the build up region make MC the ideal dose prediction method [23].

In this work, we retrospectively determine the dose to the electron boost target for five patients by using MC techniques to reconstruct the clinically defined fields on CT scans. We considered (1) a change in body habitus between the time of planning and boost delivery and (2) interfraction motion during boost delivery as determined from 3D US.

9.3 Methods and materials

9.3.1 Image acquisition

Five patients with early stage breast cancer who had undergone a lumpectomy, followed by whole breast photon irradiation (WBI), and an external beam electron boost to the TB, are reported on. Each patient underwent two CT simulations (CT1 and CT2) with concurrent 3D US imaging, to obtain fused CT/US data sets. The first CT simulation data set was obtained before WBI, and an average of 117 days (range 56-189 days) after surgery. The second CT simulation data set was performed an average of 47 days (range 34-62 days) after CT1, and immediately before boost delivery. US imaging was also performed in the treatment room prior to each boost fraction. Care was taken to not compress the breast tissue in order to avoid altering the depth and configuration of the TB. This was achieved with high viscosity US gel. The US system (Clarity, Resonant Medical Inc., Montreal, Canada) is comprised of stations in the CT room and in the treatment room. This allows US images acquired during the course of treatment to be compared with US images acquired at the time of treatment planning. Intramodality imaging (US to US) has been shown to be more accurate than intermodality imaging (US to CT) for prostate image guidance [24]. Each station uses a freehand transducer with an attached infrared marker array whose position is tracked via a ceiling mounted infrared camera. The US systems are calibrated to the respective room's isocentre so that CT and US images share a common coordinate system and are implicitly registered. The procedure for calibration and measuring organ position are outlined in Hilts et al [25]. When registered, the US slices are interpolated to the position and resolution of the CT slices.

9.3.2 Dose calculations

During WBI the patients received 42.5-50 Gy with tangential photon fields. Afterward, an electron boost of 10-15 Gy was given in 2.5-3 Gy fractions. For treatment planning purposes, at the time of simulation 1, the boost TB shape was defined clinically, and a 15 mm margin around the TB was drawn on the patient's skin to define the boost field shape for a cerrobend insert. Patients were immobilized with both arms abducted using a standard breast board. No

treatment plan was calculated for these patients other than the hand monitor unit (MU) output factor for the cerrobend insert. All patients had superficial targets so that 9 MeV penetrated to the distal side of the TB (depths ranging from 2.5-2.8 cm corresponding to 85-90% of the maximum dose in a 9 MeV PDD curve, based on water tank measurements).

For this study, the BEAMnrcmp [26] MC code was used to model a Varian Clinac 21EX linear accelerator, electron applicator, and cerrobend insert. This model has previously been verified at our institution [27]. Patient dose distributions were calculated using DOSXYZnrcmp [28]. The voxel dimensions were 1.5 mm × 1.5 mm × 3 mm, and the statistical uncertainty on doses › 50% of the maximum dose was about 0.5% of the maximum dose.

Contours on the CT images were drawn retrospectively for dosimetric analysis only. The TB was manually contoured, using Varian Eclipse software, by a single physician according to the visualized seroma fluid at the TB. A clinical target volume (CTV) and planning target volume (PTV) equivalents were retrospectively contoured on the CT images for dosimetric analysis only. The CTV and PTV were defined by uniformly expanding the excision cavity volume by 10 mm and 15 mm, respectively, and yet limiting both to 5 mm from the skin surface and eliminating the chest wall. A volume of tissue, called edge tissue, was defined by subtracting the volume of the TB from the CTV. Edge tissue represents the region potentially harbouring microscopic disease not extracted during surgery, and may even be considered the true target as the dose to the seroma fluid is not of actual interest. A MC dose calculation was performed on the CT1 and CT2 images, by reconstructing the clinically defined electron beams, in order to assess the impact of differences on the delivered dose due to patient setup errors, and a time lapse on changes in body habitus. In order to do this the local breast surface of CT2 was manually registered to the breast surface of CT1 [6]. No rotation was performed. Skin matching mimics how the patient would have been aligned with the light field during boost delivery. The dose to the targets (edge tissue and CTV), ipsilateral lung, heart, and healthy breast tissue (defined by the CTV during WBI) is compared between the two CT data sets.

All dose distributions in paired plans (CT1 and CT2 for each patient) are normalized to their respective prescribed dose in Gray, determined at the time of treatment planning. For example, if the distal side of the TB was at a depth of 2.8 cm (equal to approximately 85% of the 9 MeV PDD curve), then a prescribed dose of 10 Gy at 2.8 cm becomes 100% in the dose distribution for both CT1 and CT2 for that patient.

Dose coverage was considered adequate if the CTV D95 (minimum dose covering 95% of the volume) ≥ 95% of the prescribed dose [29]. This stringent value was chosen because it has

been demonstrated that in most cases, local recurrences occur close to the primary tumour site [30]. A geographical miss was considered true if the CTV D95 < 50% of the prescribed dose.

Similar to CT, the US TB was manually contoured on all images, using Clarity software, by a single physician according to the visualized seroma fluid at the TB. The magnitude of TB motion, and subsequent dosimetric change on target coverage, was quantified by comparing the interfraction US TB position to the reference US TB position during simulation 1. Because a second CT is not commonly performed, this represents the displacement as would be calculated in the clinic. The dose to the CT2-based CTV, taking into account TB motion, is calculated on the CT2 data set for each of the boost fractions. This method considers the motion of the TB, and any changes in body habitus between the time of planning and the beginning of the boost treatment. No actual patient realignment was performed during treatment.

9.4 Results

9.4.1 CT1 and 2 dose calculations

Table 9.1 summarizes the treatment planning parameters and dose metrics for the targets for each patient calculated on the CT1 and CT2 images. For all patients the prescription isodose line (100%) is not sufficiently wide to cover the CTV, also translating into poor TB coverage. Qualitatively, better coverage exists for targets near the skin surface and with a deep chest wall, which also results in smaller doses to the organs at risk. Quantitatively, the CT1 edge tissue D95 was always less, by up to 85%, than the prescribed dose. The CTV D95 values indicate inadequate coverage for all patients and geographic misses in 2/5 patients (patients 3 and 4). Table 9.2 summarizes the dose metrics for the organs at risk, for each patient, calculated on the CT1 and CT2 images. V95 (the volume that received at least 95% of the prescribed dose) for healthy breast tissue was essentially zero with the exception of one patient. V20 for the lung and V10 for the heart were variable, but were larger when the distance from the skin to the chest wall was smaller (3.2 cm for patient 2 and 2.2 cm for patient 5).

The difference in isodose coverage between CT1 and CT2 is shown in Fig. 9.2. The maximum dose in paired plans was similar, but varied by 1.4 Gy for patient 4. The edge tissue mean dose remained relatively constant while D95 improved for two patients, degraded for two patients, and remained the same for one patient. The CTV D95 changed by 3.3-5.8 Gy for three patients. In 3/5 patients the distal side of the TB shifted toward the surface (5 mm for patients 2 and 3, and 2 mm for patient 5).

TABLE 9.1 Dose metrics for the edge tissue and clinical target volume (CTV) as calculated on computed tomography (CT1 and CT2) images.

	Patient 1	Patient 2	Patient 3	Patient 4	Patient 5
Prescribed dose	10 Gy / 4 fxs	15 Gy / 6 fxs	10 Gy / 4 fxs	15 Gy / 6 fxs	15 Gy / 5 fxs
Approximate tumour bed depth	2.8 cm	2.5 cm	2.5 cm	2.5 cm	2.8 cm
CT1					
max dose in distribution (Gy)	12.0	16.7	10.7	16.5	17.1
edge tissue D95 (Gy)	2.7	13.6	0.8	8.0	6.7
edge tissue V90 (%)	47	96	26	49	33
edge tissue mean dose (±SD) (Gy)	7.9 (±1.7)	14.6 (±0.7)	7.0 (±2.8)	12.4 (±2.9)	12.4 (±2.4)
CTV D95 (Gy)	5.5	13.3	1.2	5.9	7.7
CTV V90 (%)	68	92	32	56	42
CTV mean dose (±SD) (Gy)	9.1 (±1.7)	13.7 (±1.4)	7.3 (±2.7)	12.7 (±2.8)	12.8 (±2.2)
CT2					
max dose in distribution (Gy)	11.7	16.9	10.7	15.1	16.1
edge tissue D95 (Gy)	3.4	13.6	7.0	2.2	2.3
edge tissue V90 (%)	59	97	42	27	23
edge tissue mean dose (±SD) (Gy)	8.5 (±2.3)	14.6 (±0.7)	8.7 (±0.9)	10.0 (±4.1)	10.4 (±3.9)
CTV D95 (Gy)	4.1	13.6	7.0	2.5	2.7
CTV V90 (%)	67	97	47	29	29
CTV mean dose (±SD) (Gy)	8.9 (±2.2)	14.6 (±0.6)	8.8 (±0.9)	10.0 (±3.9)	10.9 (±3.4)

Abbreviations: D95, dose covering 95% of the contour volume; V90, volume containing at least 90% of the prescribed dose; and SD, standard deviation.

TABLE 9.2 Dose metrics for healthy breast tissue, lung, and heart as calculated on the computed tomography (CT1 and CT2) images.

		Patient 1	Patient 2	Patient 3	Patient 4	Patient 5
CT1	Breast V95 (cm^3)	9.4	0.31	0.79	0.93	1.7
	Breast V30 (cm^3)	81	48	54	53	66
	Lung V20 (cm^3)	1.3	90	1.5	22	62
	Heart V10 (cm^3)	0.0	34	0.0	2.7	24
CT2	Breast V95 (cm^3)	8.7	4.0	1.1	3.7	0.68
	Breast V30 (cm^3)	83	65	60	49	26
	Lung V20 (cm^3)	0.0	99	1.5	5.4	55
	Heart V10 (cm^3)	0.0	57	0.0	0.0	4.3

Abbreviations: Vx, volume containing at least x% of the prescribed dose.

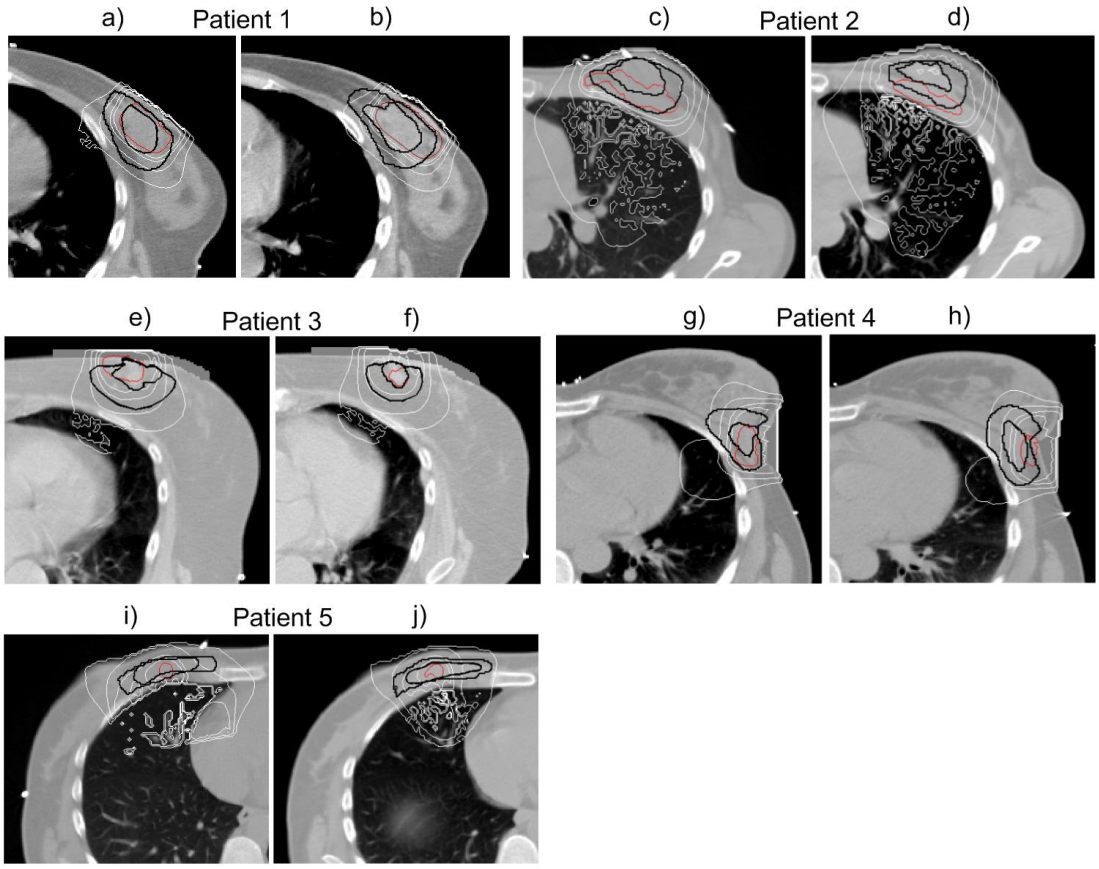

FIG. 9.2 Dose distributions on CT1 (a, c, e, g, i) and CT2 (b, d, f, h, j) images. The tumour bed and clinical target volume are contoured in black. The prescribed isodose line is in red, and the 90%, 80%, 50%, and 10% isodose lines are in white.

9.4.2 Interfraction motion

Figure 9.3 displays three patients' DVHs of the CT2-based CTV for the reference scenario (no shift), and for each fraction of the boost delivery, as calculated on the CT2 data set. The DVH line describing the combined dose from shifts was calculated by summing the dose to all voxels of the CTV2 over all fractions, and then dividing by the number of fractions in order to plot it on the same graph as the individual fraction DVHs. The difference in interfraction position from the reference position at simulation 1 is also indicated in the right (ΔR), posterior (ΔPost), and superior (ΔSup) directions, as well as the 3D radial displacement (Δradial).

The effect of daily TB motion on dose metrics is presented in Table 9.3. Interfraction motion resulted in inadequate coverage for all patients and geographic misses in 3/5 patients.

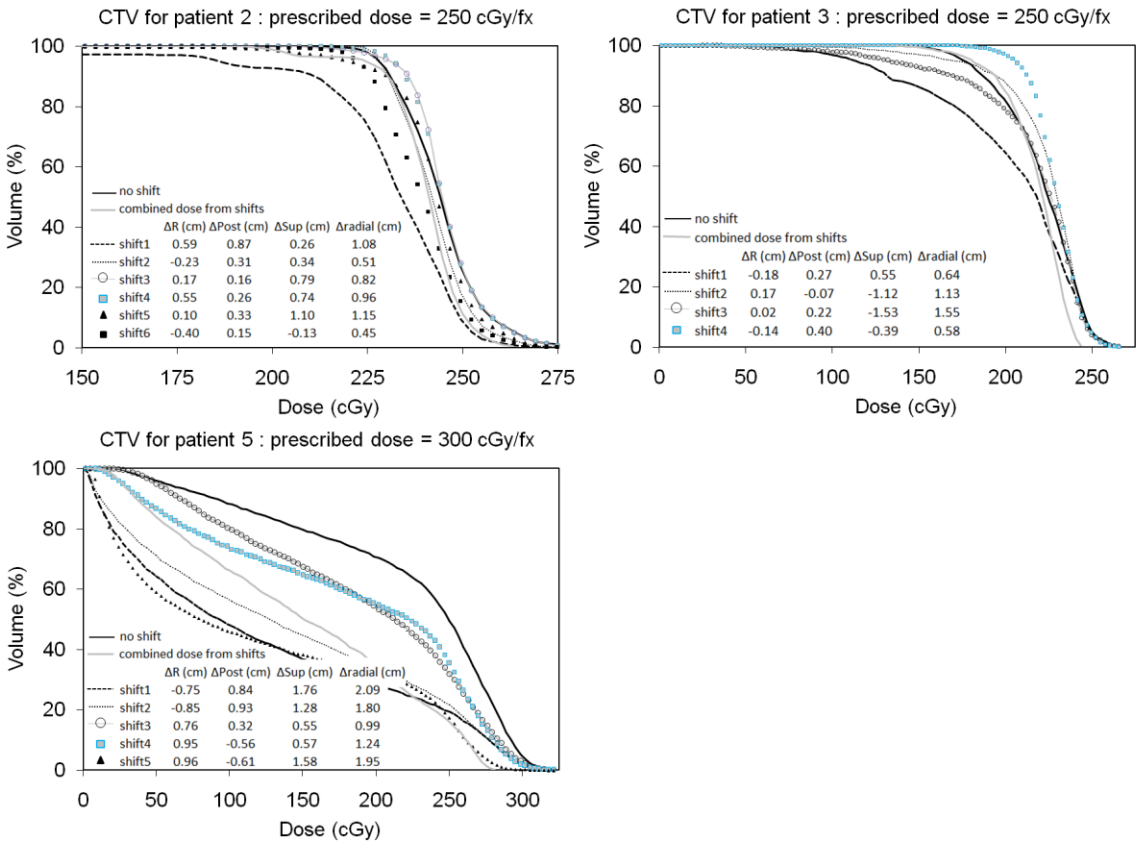

FIG. 9.3 Dose volume histograms for the CT2-based clinical target volume (CTV) for the reference scenario (no shift), for each fraction of the boost delivery considering TB motion, and for the combined dose summed over all fractions for three patients. Compared to the reference scenario, ΔR = rightward motion, Δpost = posterior motion, Δsup = superior motion, and Δradial = magnitude of 3D displacement.

9.5 Discussion

The MU hand calculations for the treatment plans were consistent with MC calculations within 3% (1 ± 1%). The literature reports similar agreement for commercial TPS electron beam dose calculations with smooth anatomy consisting mostly of soft tissue [23,31]. Despite the accurate MU calculations, the prescribed isodose line did not cover the target contours. Planning based solely on clinical information has repeatedly been reported to miss the electron boost target [3,15,21,22]. Lateral coverage could have been improved if the cerrobend insert field size had included a margin for penumbra because a beam's field size on the surface is larger than its

field size at depth for high isodose lines. In the same way, it is estimated that coverage for similarly planned treatments would further degrade for TBs located at greater depths, because higher energy electron beams exhibit more lateral isodose constriction for the higher isodose lines.

TABLE 9.3 Interfraction motion dose metrics for the combined dose summed over all fractions for the CT2-based clinical target volume (CTV).

	Patient 1	Patient 2	Patient 3	Patient 4	Patient 5
Prescribed dose	10Gy/4fxs	15Gy/6fxs	10Gy/4fxs	15Gy/6fxs	15Gy/5fxs
max dose in distribution (Gy)	11.7	15.9	9.8	14.7	14.1
CTV D95 (Gy)	4.1	13.4	7.2	5.4	1.2
CTV V90 (%)	67	94	37	19	3
CTV mean dose (±SD) (Gy)	8.9 (±2.2)	14.3 (±0.6)	8.6 (±0.7)	10.8 (±2.8)	7.4 (±4.1)

Abbreviations: D95, dose covering 95% of the contour volume; V90, volume containing at least 90% of the prescribed dose; and SD, standard deviation.

For electron beam therapy, the skin surface overlying the treatment area should ideally be flat and free from irregularities such as the nipple and surgical scar. This could result in an uneven air gap, and corrections would have to be made to the dose distribution to account for the sloping surface. For one of our patients the presence of the nipple moved the 100% isodose line by 1.2 cm. Bolus was used on patient 4 so that the surface was flat over the treatment area (Fig. 9.2g and h), and may have made an estimation of the depth to the distal side of the TB difficult as only part of the TB was underneath the bolus. The volume of edge tissue is under-dosed more than the CTV because much of the high dose volume has been subtracted out.

As the breast electron boost target is related to the TB, any change in volume and position with time from planning will affect the delivered dose. When the CT2 images were superficially aligned with the local skin surface of CT1 images, as would have been done at the treatment machine, the coverage varied from that of CT1 due to a different external contour and a change in the relationship between the skin and internal target. Improved or degraded coverage was patient specific. The CT2 data set provides a more accurate representation of patient anatomy at the time of boost delivery, especially important for a target that is known to change volume, and for surrounding tissue susceptible to radiation damage [32]. In this instance, the

difficulty with CT imaging is that the clarity of the TB decreases with time from surgery, which could be further prolonged with a course of adjuvant chemotherapy prior to radiation therapy [4].

In accordance with other sonographic studies we found that some TB posterior boundaries moved toward the surface over time. Subsequently, some authors have corrected the treatment plan, lowered the electron beam energy, and changed the field shape based on an image set acquired immediately prior to boost delivery [13]. Other authors changed the isocentre position [22]. However, in our set of patients, lower beam energy would not have covered ≥ 10 mm CTV margin, even with a decrease in TB volume from CT1 and a maximum TB shift of 5 mm toward the surface. It is clear that the dose to the targets is neither homogeneous nor encompassing as a comparison between the edge tissue D95 and mean dose reveals that there are severe hot and cold spots, such as a dose range of 7.9 Gy for patient 5. Considering that subtle changes in a patient's external contour and internal tissue densities have an observable influence on the dose distribution, it is not surprising that without accurate 3D treatment planning, the prescribed dose is not delivered for the electron boost.

An analysis of the EORTC 22881-10882 boost vs. no boost trial data by Poortmans et al [33] revealed that there was no difference in local recurrence rates between photon boosts and electron boosts. Compared to the present study, CT-based planning may improve coverage. But analytical electron beam algorithms have many shortfalls, and MC techniques are not commonly used. In this instance, the major advantage of using photon beams is that calculation algorithms have been rigorously tested and are in widespread use, yet the gains in using electron beams to treat superficial tumours (less than 5 cm deep) would be lost.

3D US is capable of accurately monitoring the TB on a day-to-day basis. US visualized the TB well on 90% of all images. For comparison, Fig. 9.4 is an example of registered CT/US images and their respective TB contours for patient 2 during simulation 1. TB volumes based on US measurements were, on average, 61% (range 29-86%) smaller than those based on CT measurements, a trend found in other studies [10,11], perhaps because different imaging modalities respond to tissue characteristics differently [5,17]. We found that the average difference in the centre of mass between US and CT contours was about 4 mm, similar to another study using an in-house 3D US system that measured the mean total distance from CT to US to be 5.1 mm [11]. Berrang et al [10] found that contours drawn on Clarity US images and CT images overlapped within 72%, similar to our average volumetric overlap of 76%. This means that the majority of US volumes were contained within CT volumes, but with a small offset.

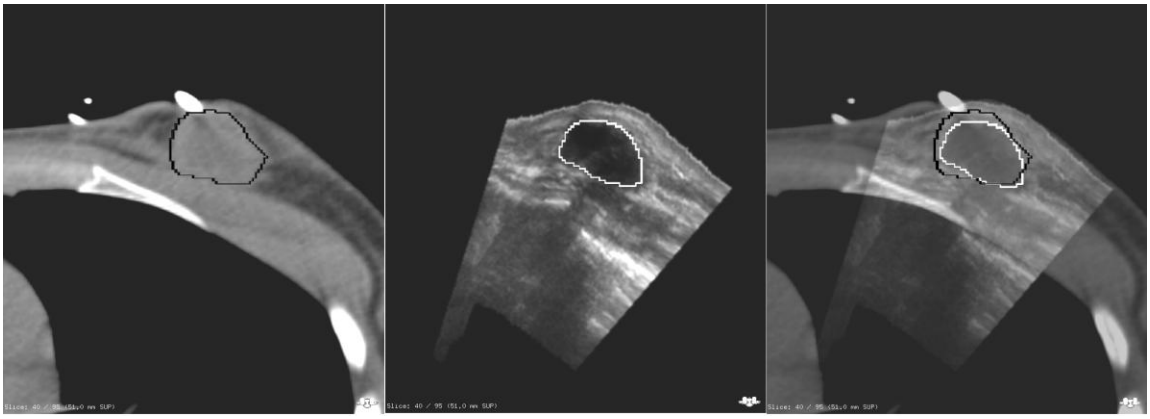

FIG. 9.4 Computed tomography tumour bed contour (black), ultrasound tumour bed contour (white), and a fused image set for patient 2.

The accuracy of the US system will, to some degree, affect the differences between US and CT TB measurements. The position of an object in a phantom has been measured to be accurate within 0.5 mm, and the position of the prostate using manual segmentation has been measured to be reproducible within 1.7 mm [25]. In comparison, the accuracy of a kV imaging system (ExacTrac X-ray, BrainLAB, Germany) that also uses a ceiling mounted camera to monitor couch motion, has been reported to be accurate within 2 mm [34]. Coregistration of breast CT and Clarity US images has been measured to be within 2 mm [10], indicating that the US system is robust and is unlikely responsible for TB position differences on the order of 5 mm.

Considering all fractions, the average interfraction radial displacement was 1.1 cm (range 0.44-2.1 cm). There was a substantial number of shifts in the posterior direction (76%). These 3D US measurements are similar to studies that used fiducial markers sewn into the excision cavity wall [2], and that used cone beam CT to look at the WBI PTV [35] and the accelerated partial breast irradiation PTV [9]. Harris et al [2] found that using fiducial markers a single measurement metric could not distinguish between volume, position, and deformation changes resulting from marker motion. Fatunase et al [9] and Jain et al [35] concluded that cone beam CT is not the most appropriate method for breast localization due to poor target visualization and the substantial dose delivered from the imaging procedure.

Daily target motion resulted in a lower maximum dose to the CTV as the dose distribution was blurred. The mean dose to the CTV in the combined dose distribution deviated from that of the reference scenario (no shift) from 60% less to 23% greater. Because the CTV was not covered by the prescription dose as shown in Fig. 9.2, we find that some TB interfraction

displacements located the CTV in higher dose regions compared to the reference position, causing some of the interfraction DVHs to improve. It is difficult to compare our results to the literature as no one has previously reported the dosimetry of interfraction motion in electron beams to the same target. But to get an idea, some authors have reported interfraction dosimetric discrepancies to larger breast targets with photon techniques on the order of a few percent [9,35,36]. In this study, the combination of the treatment modality (electrons), the treatment planning procedure (conventional, not 3D), and the target of interest (TB) is shown to be more susceptible, by accurate MC techniques, to motion degradation than other breast treatment techniques.

The patient with the largest average radial displacement (patient 5) resulted in the greatest mean dose discrepancy (7.4 Gy / 15 Gy = 0.49). The patient with the smallest average radial displacement (patient 2) resulted in the smallest mean dose discrepancy (14.3 Gy / 15 Gy = 0.95). A closer look reveals that patient 2 is also the patient with the largest field size where the lateral width of the CTV was most similar to the 100% isodose line. This patient also had the highest US to CT volume overlap. The patient with the smallest field size (patient 3) was the second farthest from that prescribed, yet had the second smallest average radial shift. Consequently, dosimetric effects depend on the interplay between the magnitude of motion and patient specific treatment planning parameters.

Using the margin recipe from van Herk et al [37], the margin for setup error and interfraction motion for these 5 patients should be 0.62 cm right/left, 0.74 cm anterior/posterior, and 0.79 cm superior/inferior. In order to include predictable motion due to respiration, a factor related to the peak-to-peak amplitude should be included [38,39]. Yet, as pointed out by Thomas et al [40], the factors affecting target motion in external electron beam therapy are very different from those in conformal photon treatment plans. Electron treatments generally consist of a single field so that setup errors parallel to the incident beam are different from those in a perpendicular direction. Parallel to the beam, setup errors have a minimal change in the PDD, and a larger change in machine output and beam penumbra. Consequently, even if margins are determined with certainty, the absolute dose to the TB and healthy tissue remains variable. Therefore, generalized margins for electron boosts may not provide ideal coverage, whereas 3D image guidance is capable of localizing the TB and provides all the required information to replan if deemed necessary.

9.6 Conclusion

The dosimetric consequences of missing the TB in electron boosts are substantial, and TB interfraction motion provides an additional factor to consider and exacerbates the uncertainty in the delivered dose. Planning should be performed immediately prior to dose delivery using an accurate dose calculation method. As revealed by daily 3D US imaging, the 5 mm PTV margin used in this study was too conservative to account for interfraction motion when no patient repositioning was performed. These factors will have an even larger impact for hypofractionated treatments, where doses greater than twice that used in this study are prescribed within a similar time frame.

9.7 Acknowledgements

The authors would like to thank Eric Reynard for his help with transferring data between workstations, interpretation of the treatment charts, and insightful discussions. Resonant Medical, Inc. is thanked for their time to train personnel in the use of the breast module of the Clarity system. The US equipment and MC engine were partially acquired with a New Opportunity Grant of the Canada Foundation for Innovation (CFI, Grant #10036).

9.8 Afterward

In this chapter we have shown that it is possible to accurately estimate the dose in external electron beams. We demonstrated that conventional treatment planning techniques result in inadequate target coverage and geographical misses. Dosimetric coverage of the CTV was poor in all patients, and perhaps more importantly dosimetric coverage to edge tissue was even worse. This volume may represent the true target for early stage breast cancer patients. This situation could be improved with 3D CT based treatment planning, which also allows for dose calculations in the patient geometry. It is recommended that planning for the electron boost be performed as close to boost delivery as possible.

The images from this study also show CT and US derived TB volumes are different. Table 9.4 compares the geometry of the four TB contours for each patient. On average, US volumes were 61% (range 29-86%) smaller than CT volumes. Any volume changes that occurred between CT1 and CT2 did not correlate with time after surgery. For 4/5 patients the volume ratios US2/US1 < 1 when CT2/CT1 < 1. In general the majority of the US volumes were contained within the CT volumes but were off centered.

TABLE 9.4 Computed tomography and ultrasound based tumour bed comparisons.

	Patient 1	Patient 2	Patient 3	Patient 4	Patient 5
Volume ratios					
US1 / CT1	0.33	0.71	0.09	0.59	0.27
US2 / CT2	0.61	0.61	0.14	0.40	0.19
CT2 / CT1	1.2	0.44	1.1	1.1	0.52
US2 / US1	2.2	0.38	1.7	0.73	0.36
Volumetric overlap (%)					
US1 and CT1	86	90	61	73	79
US2 and CT2	85	61	100	78	44
CT2 and CT1	66	61	39	71	84
US2 and US1	39	32	0.0	61	98
Radial position difference (cm)					
US1 - CT1	0.33	0.33	0.76	0.25	0.12
US2 - CT2	0.42	0.61	0.45	0.58	0.20
CT2 - CT1	0.38	0.50	0.49	0.23	0.25
US2 - US1	0.30	0.13	1.5	0.62	1.1

Volumes based on US measurements were smaller than those based on CT measurements. Only 50% of the TB volumes (CT and US modalities) decreased between CT1 and CT2. The lack of coherence may be due to the large average time between surgery and imaging (117 days), providing sufficient time for tissue remodeling to occur. These factors would also affect the position of the TB as visualized on either modality. The lack of 100% agreement of TB volume and position between different imaging modalities suggests that CT-based TBs should not be the sole guide for target definition.

9.9 References

[1] Bartelink H, Horiot JC, Poortmans PM, et al. Impact of a higher radiation dose on local control and survival in breast-conserving therapy of early breast cancer: 10-year results of the randomized boost versus no boost EORTC 22881-10882 trial. *J Clin Oncol* 2007; 25: 3259-3265

[2] Harris EJ, Donovan EM, Yarnold JR, Coles CE, Evans PM. Characterization of target volume changes during breast radiotherapy using implanted fiducial markers and portal imaging. *Int J Radiat Oncol Biol Phys* 2009; 73: 958-966

[3] Hepel JT, Evans SB, Hiatt JR, et al. Planning the breast boost: comparison of three techniques and evolution of tumor bed during treatment. Int *J Radiat Oncol Biol Phys* 2009; 74: 458-463

[4] Kader HA, Truong PT, Pai R, et al. When is CT-based postoperative seroma most useful to plan partial breast radiotherapy? Evaluation of clinical factors affecting sermoa volume and clarity. *Int J Radiat Oncol Biol Phys* 2008; 72: 1064-1069

[5] Kirby AM, Coles CE, Yarnold JR. Target volume definition for external beam partial breast radiotherapy: Clinical, pathological and technical studies informing current approaches. *Radiother Oncol* 2010; 94: 255-263

[6] Topolnjak R, van Vliet-Vroegindeweij C, Sonke JJ, et al. Breast-conserving therapy: radiotherapy margins for breast tumor bed boost. *Int J Radiat Oncol Biol Phys* 2008; 72: 941-948

[7] Hasan Y, Kim L, Martinez A, Vicini F, Yan D. Image guidance in external beam accelerated partial breast irradiation: comparison of surrogates for the lumpectomy cavity. *Int J Radiat Oncol Biol Phys* 2007; 70: 619-625

[8] Gierga DP, Riboldi M, Turcotte JC. Comparison of target registration errors for multiple image-guided techniques in accelerated partial breast irradiation. *Int J Radiat Oncol Biol Phys* 2008; 70: 1239-1246

[9] Fatunase T, Wang Z, Yoo S, et al. Assessment of the residual error in soft tissue set-up in patients undergoing partial breast irradiation: results of a prospective study using cone-beam computed tomography. *Int J Radiat Oncol Biol Phys* 2008; 70: 1025-1034

[10] Berrang T, Truong P, Pompescu C, et al. 3D ultrasound can contribute to planning CT to define the target for partial breast radiotherapy. *Int J Radiat Oncol Biol Phys* 2009; 73: 375-383

[11] Coles CE, Cash CJC, Treece GM, et al. High definition three-dimensional ultrasound to localise the tumour bed: A breast radiotherapy planning study. *Radiother Oncol* 2007; 84: 233-241

[12] Ringash J, Whelan T, Elliott E, et al. Accuracy of ultrasound in localization of breast boost field. *Radiother Oncol* 2004; 72: 61-66

[13] Warszawski A, Baumann R, Karstens J. Sonographic guidance for electron boost planning after breast-conserving surgery. *J Clin Ultrasound* 2004; 32: 333-337

[14] Goldberg H, Prosnitz RG, Olson JA, Marks LB. Definition of postlumpectomy tumor bed for radiotherapy boost field planning: CT versus surgical clips. *Int J Radiat Oncol Biol Phys* 2005; 63: 209-213

[15] Kovner F, Agay R, Merimsky O, Stadler J, Klausner J, Inbar M. Clips and scar as the guidelines for breast radiation boost after lumpectomy. *Eur J Surg Oncol* 1999; 25: 483-486

[16] Weed DW, Yan D, Martinez AA, et al. The validity of surgical clips as a radiographic surrogate for the lumpectomy cavity in image-guided accelerated partial breast irradiation. *Int J Radiat Oncol Biol Phys* 2004; 60: 484-492

[17] Landis DM, Luo W, Song J, et al. Variability among breast radiation oncologists in delineation of the postsurgical lumpectomy cavity. *Int J Radiat Oncol Biol Phys* 2007; 67: 1299-1308

[18] Thomas CW, Nichol AM, Park JE, et al. An anthropomorphic phantom study of visualisation of surgical clips for partial breast irradiation (PBI) setup verification. *Radiother Oncol* 2009; 90: 56-59

[19] Offersen BV, Overgaard M, Kroman N, Overgaard J. Accelerated partial breast irradiation as part of breast conserving therapy of early breast carcinoma: A systematic review. *Radiother Oncol* 2009; 90: 1-13

[20] van Mourik AM, Elkhuizen PHM, Minkema D, JC Duppen. Multiinstitutional study on target volume delineation variation in breast radiotherapy in the presence of guidelines. *Radiother Oncol* 2010; 94: 286-291

[21] Bates AT, Swift CL, Kwa W, Moravan V, Aquino-Parsons C. A computed tomography-based protocol vs conventional clinical mark-up for breast electron boost. *Clin Oncol* 2007; 19: 349-355

[22] Benda RK, Yasuda G, Sethi A, et al. Breast boost: Are we missing the target? *Cancer* 2003; 97: 905-909

[23] Cygler JE, Lochrin C, Daskalov GM, et al. Clinical use of a commercial Monte Carlo treatment planning system for electron beams. *Phys Med Biol* 2005; 50: 1029-1034

[24] Cury FL, Shenouda G, Souhami L, et al. Ultrasound-based image guided radiotherapy for prostate cancer-comparison of cross-modality and intramodality methods for daily localization during external beam radiotherapy. *Int J Radiat Oncol Biol Phys* 2006; 66: 1562-1567

[25] Hilts M, Bull T, Patterson K, et al. Reproducibility of prostate misalignments computed by automatic segmentation of abdominal ultrasound images used for image guided radiation therapy. *Int Federation Med Biol Eng Proc* 2006; 14: 1712-1715

[26] Rogers DWO, Fadegon BA, Ding GX, Ma CM, Wei J, Mackie TR. BEAM: A Monte Carlo code to simulate radiotherapy treatment units. *Med Phys* 1995; 22: 503-524

[27] Jarry G and Verhaegen F. Electron beam treatment verification using measured and Monte Carlo predicted portal images. *Phys Med Biol* 2005; 50: 4977-4994

[28] Walters B, Kawrakow I, Rogers DWO. DOSXYZnrc users manual 2004 NRCC Report PIRS-794revB (Ottawa, Canada: NRCC)

[29] van der laan HP, Dolsma WV, Maduro JH, Korevaar EW, Langendijk JA. Dosimetric consequences of the shift towards computed tomography guided target definition and planning for breast conserving radiotherapy. *Radiother Oncol* 2008; 3: 6-13

[30] Holland R, Veling SH, Mravunac M, Hendriks JH. Histologic multifocality of Tis, T1-2 breast carcinomas. Implications for clinical trials of breast-conserving surgery. *Cancer* 1985; 56: 979-990

[31] Fragoso M, Pillai S, Solberg TD, Chetty IJ. Experimental verification and clinical implementation of a commercial Monte Carlo electron beam dose calculation algorithm. *Med Phys* 2008; 35: 1028-1038

[32] Borger JH, Kemperman HWPM, Sillevis Smit H, et al. Dose and volume effects on fibrosis after breast conserving therapy. *Int J Radiat Oncol Biol Phys* 1994; 30: 1073-1081

[33] Poortmans P, Bartelink H, Horiot JC, et al. The influence of the boost technique on local control in breast conserving treatment in the EORTC 'boost versus no boost' randomised trial. *Radiother Oncol* 2004; 72: 25-33

[34] Hayashi N, Obata Y, Uchiyama Y, Mori Y, Hashizume C, and Kobayashi T, Assessment of spatial uncertainties in the radiotherapy process with the Novalis system. *Int J Radiat Oncol Biol Phys* 2009; 75: 549-557

[35] Jain P, Marchant T, Breen M, et al. Inter-fraction motion and dosimetric consequences during breast intensity-modulated radiotherapy (IMRT). *Radiother Oncol* 2009; 90: 93-98

[36] Baroni G, Garibaldi C, Scabini M, et al. Dosimetric effects within target and organs at risk of interfractional patient mispositioning in left breast cancer radiotherapy. *Int J Radiat Oncol Biol Phys* 2004; 59: 861-871

[37] van Herk M, P Remeijer, C Rasch, JV Lebesque. The probability of correct target dosage: dose-population histograms for deriving treatment margins in radiotherapy. *Int J Radiat Oncol Biol Phys* 2000; 47: 1121-1135

[38] McKenzie AL. How should breathing motion be combined with other errors when drawing margins around the clinical target volumes? *Br J Radiol* 2000; 73: 973-977

[39] van Herk M, Witte M, van der Geer J, et al. Biological and physical fractionation effects of random geometrical errors. *Int J Radiat Oncol Biol Phys* 2003; 57: 1460-1471

[40] Thomas SJ. Margins between clinical target volume and planning target volume for electron beam therapy. *Br J Radiol* 2006; 79: 244-247

CHAPTER 10
Thesis conclusion

10.1 Summary

In this work the dosimetric impact of interfraction organ motion and tissue remodeling was quantified for prostate, head and neck, and breast cancer sites using a new 3D ultrasound system designed for radiation therapy applications, and using accurate Monte Carlo dose calculation techniques. The popularization of sophisticated dose delivery techniques that tightly conform the dose distribution leads to new requirements for treatment verification. It was determined that image verification, by realigning the target under the treatment beams, does not always guarantee that the planned delivered dose is the true delivered dose for all cancer sites, and that dose verification is required in order to further reduce errors in the treatment delivery procedure.

In Chapter 5 we described the 3D ultrasound system used in this work and demonstrated that ultrasound imaging could be performed on non-traditional sites for radiation therapy purposes. In Chapter 6 we applied ultrasound image guidance to patients with nasopharyngeal cancers with involved cervical lymph nodes. We quantified the changes in position and geometry of the lymph nodes in patients representative of typical scenarios. We subsequently analyzed the dose to the lymph nodes throughout treatment and determined that they could be substantially under dosed. We hypothesize that simple patient realignment may not provide optimum coverage (to the nodes and other tissue) in intensity modulated radiation therapy fields. Instead, ultrasound image guidance is proposed as a noninvasive tool to trigger when adaptive replanning should occur.

In Chapter 7 the importance and implications of using accurate dose calculation algorithms for treatment planning for prostate 3D conformal radiation therapy was discussed. We compared different algorithms and it was determined that for this cancer site heterogeneities did not alter the dose distribution as much as did simplifications in the radiation transport algorithm. These results were utilized in Chapter 8 when prostate organ motion was considered.

In Chapter 8 we dosimetrically quantified the impact of daily prostate motion in 3D conformal radiation therapy using intramodality image verification. Daily ultrasound images of the prostate were compared with a reference ultrasound image acquired in the CT simulation room at the time of planning. This allowed us to bypass any errors due to differences in tissue representation between different imaging modalities. MC simulations of prostate displacements for each fraction for 32 patients allowed us to confidently conclude that for our model of rigidly moving the prostate, bladder, and rectum together, patient realignment does not substantially alter the dose delivered to the target or organs at risk for this cancer site and treatment modality.

In Chapter 9 we changed our focus to target alignment in electron beams, which have lacked the same attention and accuracy as photon beams. We monitored changes to the lumpectomy cavity and its surrounding edge tissue in early stage breast cancer patients, and determined that tissue remodeling and set-up errors cause geometrical misses in the target and also cause healthy radiation sensitive tissue to be irradiated. Moreover, conventional planning techniques in electron beams are insufficient to ensure adequate target coverage, especially when planned weeks before the electron dose is delivered.

10.2 Future work

Initial use of ultrasound prostate image guidance has already resulted in the confident reduction of planning target volume margins [1-3]. However, the dosimetric results found in this thesis should be verified when other treatment modalities (such as intensity modulated radiation therapy) and different margin sizes are used. In addition, deformable registration techniques would greatly augment further dosimetric studies. Ultrasound imaging has often been compared to portal images of prostate implanted fiducial markers, as portal imagers have been a standard add-on to linacs [4-6]. Yet a study comparing the relatively new kV cone beam CT imaging with ultrasound imaging would also provide valuable information as both have better soft tissue contrast than MV imaging, although it may be clinically redundant to have both imagers in the same treatment room.

Ultrasound applications in radiation therapy have been focused on interfraction prostate imaging, but the potential of this modality has yet to be fully realized. For other sites, the system used in this study is now quite capable of imaging the head and neck region, so that further studies with more patients could be performed to enhance our case study. Even though we have applied ultrasound imaging to other sites with success, the implementation of harmonic imaging and contrast agents will aid in identifying tissue on these images [7,8]. In this manner, computer aided segmentation for multiple cancer sites (by using an anatomy atlas, for example) may help in defining the target and margin definition, with only minor intervention to ensure quality assurance and to tune the contours. Subsequently, as treatment delivery becomes more accurate, imaging might expose limitations in the correctness of current clinical target volume definitions.

There has also been preliminary work on tissue typing in ultrasound images [9,10]. This allows automatic tissue identification based on the scatter characteristics of the tissue. Tissue typing may allow for deformable image registration. It may also allow for dose calculations to be performed directly on the ultrasound data if the ultrasound data, with a limited field of view, is registered with the CT data. Deformable registration was not used in this thesis but would be a valuable addition to further dosimetric studies. Tissue typing may also lead to the ability to correct for the various speeds of sound in different tissues, thereby removing spatial distortions and perhaps minimizing tissue representation differences between imaging modalities.

Ultrasound imaging may also increasingly find itself at the forefront of imaging options as the financial and manpower burden of new technology increases. This would require more research on developing acquisition techniques that are systematic, and on producing quality images independent of the user's experience. Full field of view sonographic volumes, as has already been developed for the breast, may be one such solution.

Image guidance may lead to a change in fractionation schedules, currently practiced at a typical 2 Gy per fraction. Fractionation was devised to exploit the differential repair capabilities of normal tissues and tumours, but the reduction in irradiated normal tissue due to IGRT may provide a more forgiving scenario allowing for increased doses with fewer fractions. This would also put greater emphasis on the role of the radiation therapist who evaluates the daily IGRT images and makes decisions without the physician. This role change will become more critical when image guidance is used as a trigger to determine when to replan, and to evaluate the new plan. This step also requires further research into faster Monte Carlo dose calculation algorithms, as assumptions in analytical algorithms will limit the accuracy of the dose calculation step.

10.3 References

[1] Ghilezan M, Yan D, Liang J, et al. Online image-guided intensity-modulated radiotherapy for prostate cancer; How much improvement can we expect? A theoretical assessment of clinical benefits and potential dose escalation by improving precision and accuracy of radiation delivery. *Int J Radiat Oncol Biol Phys* 2004; 60: 1602-1610

[2] Peeters ST, Heemsbergen WD, Koper PC, et al. Dose–response in radiotherapy for localized prostate cancer; results of the Dutch multicenter randomized phase III trial comparing 68 Gy of radiotherapy with 78 Gy. *J Clin Oncol* 2006; 24: 1990-1996

[3] Pollack A, Hanlon AL, Horwitz EM, et al. Dosimetry and preliminary acute toxicity in the first 100 men treated for prostate cancer on a randomized hypofractionation dose escalation trial. *Int J Radiat Oncol Biol Phys* 2006; 64: 518-526

[4] Langen KM, Pouliot J, Anezinos C, et al. Evaluation of ultrasound-based prostate localization for image-guided radiotherapy. *Int J Radiat Oncol Biol Phys* 2003; 57: 635-644

[5] Van den Heuvel F, Powell T, Seppi E, et al. Independent verification of ultrasound based image-guided radiation treatment, using electronic portal imaging and implanted gold markers. *Med Phys* 2003; 30: 2878-2887

[6] Scarbrough TJ, Golden NM, Ting JY, et al. Comparison of ultrasound and implated seed marker prostate localization methods; implications for image guided radiotherapy. *Int J Radiat Oncol Biol Phys* 2006; 65: 378-387

[7] Burns PN and Wilson SR. Focal Liver Masses: Enhancement patterns on contrast-enhanced images - concordance of US with CT and MR images. *Radiology* 2007; 242: 162-174

[8] Halpern EJ, Ramey JR, Strup SE, Frauscher F, McCue P, Gomella LG. Detection of prostate carcinoma with contrast-enhanced sonography using intermittent harmonic imaging. *Cancer* 2005; 104: 2373-2383

[9] Liu T, Mansukhani MM, Benson MC, et al. A feasibility study of novel ultrasonic tissue characterization for prostate-cancer diagnosis: 2D spectrum analysis of in vivo data with histology as gold standard. *Med Phys* 2009; 36: 3504-3511

[10] Zhang P, Osterman KS, Liu T, et al. How does performance of ultrasound tissue typing affect design of prostate IMRT dose-painting protocols? *Int J Radiat Oncol Biol Phys* 2007; 67: 362-368

LIST OF ABBREVIATIONS

2D	two dimensional
3D	three dimensional
3DCRT	three dimensional conformal radiation therapy
ART	adaptive radiation therapy
BEV	beam's eye view
CBCT	cone beam computed tomography
CT	computed tomography
CTV	clinical target volume
D	dipole displacement
d	piezoelectric charge constant
DRR	digitally reconstructed radiograph
DVH	dose volume histogram
EPID	electronic portal imaging device
GTV	gross tumour volume
ICRU	International Commission on Radiation Units
IGRT	image guided radiation therapy
IMRT	intensity modulated radiation therapy
kV	kilovoltage
linac	linear accelerator
M	overall mean error in positioning for a population of patients, the mean of all patient means
MC	Monte Carlo
MLC	multileaf collimator
MR	magentic resonance
MV	megavoltage
OAR	organ at risk
PET	postitron emission tomography
PTV	planning target volume
PZT	lead zirconate titanate
RT	Radiation therapy

SD	standard deviation
SPECT	single photon emission computed tomography
TPS	treatment planning system
US	ultrasound
Z	acoustic impedance
Σ	systematic positioning error (preparation error)
σ	standard deviation OR random positioning error (execution error)
σ_s	applied stress
μ	attenuation coefficient OR average